INSPECTION OF WELD PENETRATION DEPTH IN THIN STRUCTURES USING LASER-GENERATED LAMB WAVES AND EMAT RECEIVER

A Ph.D. Dissertation Presented to
The Academic Faculty
By

Lei Yang

In Partial Fulfillment
of the Requirements for the Degree
Doctor of Philosophy in the
George W. Woodruff School of Mechanical Engineering

Georgia Institute of Technology
August, 2015

INSPECTION OF WELD PENETRATION DEPTH IN THIN STRUCTURES USING LASER-GENERATED LAMB WAVES AND EMAT RECEIVER

Approved by:

Dr. Charles Ume, Advisor
School of Mechanical Engineering
Georgia Institute of Technology

Dr. Shreyes N. Melkote
School of Mechanical Engineering
Georgia Institute of Technology

Dr. Jennifer E Michaels
School of Electrical and Computer Engineering
Georgia Institute of Technology

Dr. Karim Sabra
School of Mechanical Engineering
Georgia Institute of Technology

Dr. Chun (Chuck) Zhang
School of Industrial and Systems Engineering
Georgia Institute of Technology

Date Approved: October 6, 2014

Acknowledgements

I would like to thank my advisor, Dr. Charles Ume, for his guidance, support, and friendship. Dr. Ume has given valuable advice throughout this research project. I have also learned different facets of teaching from Dr. Ume and his Mechatronics classes.

I would like to thank my thesis reading committee: Dr. Jennifer E Michaels, Dr. Karim Sabra, Dr. Shreyes N. Melkote, and Dr. Chun (Chuck) Zhang. I sincerely appreciate their time and valuable suggestions to make my research more comprehensive.

I would like to thank all of my colleagues in Dr. Ume's group for their support: Dr. Matt Rogge, Dr. Tsun-yen Wu, Sungbum Kang, and Jie Gong.

I would like to thank my parents, Mr. Huigao Yang and Mrs. Lanfang Ge, for all of their support and love throughout my life.

Last but not least, I would like to than my wife, Mrs. Xuefei Han, for her continuous love, understanding and support.

Table of Contents

List of Tables

List of Figures

SUMMARY

Welding is one of the most common joining processes in industry. Weld penetration depth (WPD) is a key measure of weld quality since it directly determines the weld joint strength. It is highly desired to develop non-destructive techniques to accurately assess WPDs. The laser/EMAT ultrasonic (LEU) technique has drawn interests from industry for its non-contact operation, which enables the technique for online inspections. Previous research has developed effective signal processing methods to predict WPDs in thick structures using the LEU technique. The prediction is based on the measurement of time of flight (ToF) of laser-generated bulk and surface waves following certain paths. However, as structure thickness decreases, the laser-generated ultrasounds become Lamb waves. Because of the way how Lamb waves propagate, there is no internal path to follow, therefore, the ToF-based method is not applicable in thin structures. It is necessary to find other indicators in the acquired signals to enable the LEU technique to predict WPDs in thin structures.

The objective of this research is to develop an effective signal interpretation method to extend the capability of the LEU technique for WPD inspections to thin structures. Two major challenges need to be overcome to accomplish the research objective. First, the laser-generated Lamb waves are broadband and contains multiple modes, which are very complicated. Different Lamb waves are overlapping in both time and frequency domains. Their traveling speeds are frequency-dependent. The waveforms of the acquired signals is sensitive to the distance from the laser source to the EMAT receiver. All of these facts make the acquired signals very complicated. Secondly, the interaction of laser-generated Lamb waves with the weld joint is very complicated.

Therefore, it's difficult to find new indicators, which are informative of WPDs, from the acquired signals.

A systematic study is conducted in this research to investigate how to use the LEU technique to measure WPDs in thin structures. The systematic study consists of four main aspects. First, LEU signals in thin structures are experimentally characterized to establish a fundamental understanding of the acquired signals. Strong Lamb waves present in the acquired signals are identified, and the following study will only focus on these strong Lamb waves. Secondly, interactions of laser-generated Lamb waves with a WPD-related defect are investigated by measuring wave field signals close to the defect. 3-D FT of the wave field signals helps to separate different Lamb waves and assess their sensitivities to varying WPDs. Thirdly, the possibility of using transmission coefficients of Lamb waves to measure varying notch depths are investigated both numerically and experimentally. An efficient method is developed to calculate transmission coefficients of different Lamb waves in LEU signals, and transmission coefficients of Lamb waves show the potential to measure WPDs in thin structures quantitatively. Finally, real welds of varying WPDs are manufactured using gas metal arc welding (GMAW) to test the sensitivity of transmission coefficients of different Lamb waves. 23 laser-generated Lamb waves are selected and their transmission coefficients are used to develop a neural network to predict WPDs in thin structure. Considerations regarding the implementation of the proposed method are also discussed.

The final deliverable of this research is a fast, efficient, accurate, non-contact, and non-destructive WPD prediction method in thin structures using the LEU technique. This method

shows great potentials. Its implementation is computationally efficient, which enable its application in real time. Even though the method is developed using welds produced by GMAW, it can also inspect welds manufactured by other welding processes.

CHAPTER 1

Introduction

Welding is one of the most important joining processes in industry. Good weld quality is essential to ensuring structural integrity and product safety. Nevertheless, during the welding process, different defects may occur in welds [1]. Traditionally in industry, welded assemblies are sampled and cut-checked to make sure that the welding setup and parameters are producing satisfactory welds. If the cut-checked weld doesn't meet the requirements, the production line will be stopped to allow experienced operators to adjust the welding setup and parameters. The unsatisfactory welds produced previously will be tossed away. The cut-check method is very inefficient and costly. It is highly desired that a non-destructive weld inspection technique can provide feedback control of the welding process in real time.

1.1 Defects in Welds

Weld quality is relative. Standards of good weld quality are established based on the service requirements. In fact, welding standards are different in different industries, even in different companies. Therefore, the definition of weld defect is also relative. Weld defects in some standards may be acceptable in other standards. However, some defects are common in all standards, which include porosities, undercut, cracks etc. Other defects are related to weld dimensions, which include lack of penetration, lack of reinforcement, insufficient bead width, etc. These defects are relative. Different standards may have different requirements on these weld dimensions. Failure to meet these requirements is treated as a weld dimension-related defect.

Fig. 1-1 shows the cross-section of a butt joint weld, which illustrates the common weld defects and important weld dimensions.

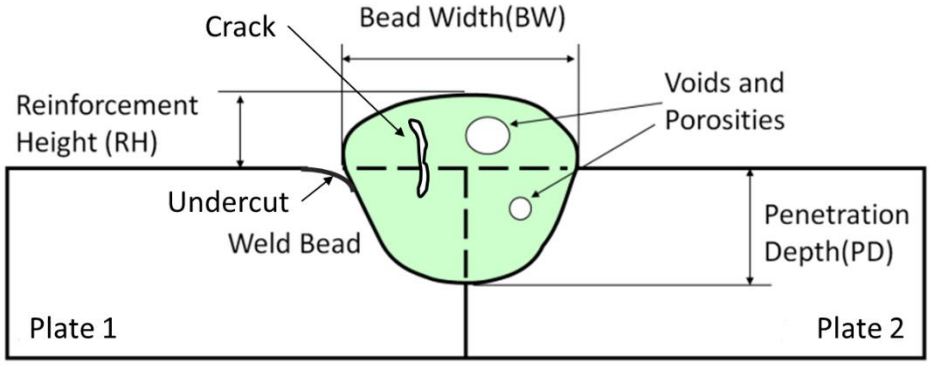

Fig. 1-1: Cross-section of butt joint weld

Among the weld dimensions, weld penetration depth (WPD) is most critical because it directly determines the bearing strength of the weld and therefore a key measurement of weld quality. WPD is defined as the depth at which the weld bead extends into the base material. Since there are so many dynamic factors affecting the welding process, WPD usually varies a lot. Different manufacturers have different standards that the WPD needs to be greater than a threshold value. Smaller than the threshold value is treated as a lack of penetration defect. Enforcing these standards requires a reliable and accurate method to measure WPDs. This research will focused on develop a non-destructive method to measure WPDs of butt joint welds in thin structures. The ultimate goal is to incorporate the developed method into automatic welding systems to achieve a feedback control of WPDs in real time.

1.2 Non-destructive Testing of Welds

Different non-destructive testing techniques have been developed for inspection of weld qualities [2]. Some of them are very mature and even commercialized. Some of them are still under development. All of them have advantages and limitations. The selection of these techniques is really dependent on the specific applications. Some of the common non-destructive techniques for weld inspections are summarized below.

1.2.1 Visual Inspection

Visual inspection (VI) is the simplest and most cost-effective method to assure weld quality [3]. Visual inspection can take place before, during and after welding. It requires little equipment but a broad knowledge from the inspector. A good-looking weld appearance is sometimes considered indicative of high weld quality. However, weld appearance alone assure nothing about internal quality.

1.2.2 Radiographic Inspection

Radiography inspection (RI) is used to determine the internal quality of welds based on the ability of X-rays and gamma rays to pass through metal and produce photographic records of the transmitted radiant energy on a permanent film [4, 5]. Different materials will absorb different amounts of radiant energy. Therefore, X-rays and gamma rays can be used to show discontinuities and inclusions within the weld. Skilled operators are necessary to interpret the X-ray film to identify small defects [6].

1.2.3 Magnetic Particle Inspection

Magnetic particle inspection (MPI) is a non-destructive testing process widely used for weld quality inspection, especially for crack detection. The inspection process applies a magnetic field into the sample and ferrous iron particles on the sample surface. The presence of any surface or subsurface discontinuity will produce a magnetic flux leakage area, which the particles will be attracted to. Therefore, potential defects can be identified by looking for particle build-up areas. The potential defects can be further evaluated to determine what it is [7, 8]. There are already many standards established for the MPI process.

1.2.4 Liquid Penetrant Inspection

Liquid penetrant inspection (LPI) is a cost-effective inspection method widely used to locate hard-to-see cracks in welds based upon capillary action. Fig. 1-2 shows the major LPI steps [9]. First, the inspected area is cleaned. Then the penetrant is applied to the surface. Next, the excess penetrant is removed. Finally, the developer is applied to render the crack visible. The inspection procedure requires both pre and post inspection cleaning. It also requires smooth sample surface to allow excessive penetrant to be removed. It is only good for surface defect detection. There are already many standards established for the LPI process.

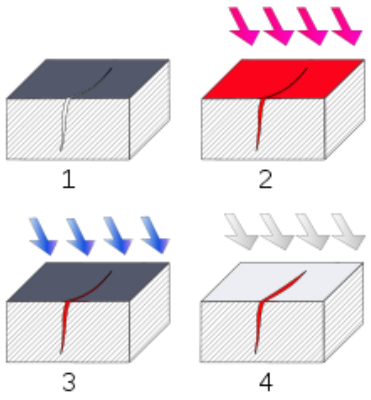

Fig. 1-2: Main LPI steps

1.2.5 Alternating Current Field Measurement Technique

Alternating Current Field Measurement (ACFM) is an electromagnetic NDT technique which can both detect and size surface cracks. It can work through thin coatings such as paint or rust [10]. The ACFM probe induces a uniform alternating current in the area under test and detects magnetic field of the resulting current near the surface. A crack will disturb the current around the ends and faces of the crack. The ACFM instrument measures these disturbances and uses mathematical modelling to estimate crack size. This technique is not recommended for small items due to the disturbances from boundaries. The technique can only measure cracks longer than 5 mm. Equipment is bulky and expensive and requires trained operators to interpret recorded data.

1.2.6 Eddy Current Inspection

Eddy current testing (ECT) is another widely used NDT technique for weld inspection [11]. Commercial portable ECT instruments are available. When the probe, which has a circular coil carrying alternating current, is placed in proximity to a sample, it generates changing magnetic field which interacts with the sample and generates eddy current. Variations of the eddy currents caused by discontinuities in the test specimen are detected. The ECT technique requires the inspected area to be accessible and is limited to detection of surface and subsurface defects. It is only sensitive to defects that lie perpendicular to the probe.

1.2.7 Infrared Thermography Method

Infrared thermography (IRT) method [12] is primarily used as an online NDT method to monitor and control weld quality. It monitors weld quality based on the temperature distribution at the welding pool [13, 14]. It is an indirect method and is not good at evaluating internal weld quality.

1.2.8 Ultrasonic Testing

Ultrasonic testing (UT) is a family of NDT techniques. It is widely used for weld quality inspection [15]. Traditional method applies transducers to emit and receive ultrasounds, which requires liquid couplant to be used between transducers and the specimen. This makes the traditional UT technique not suitable for inspecting moving samples and rough surfaces. Plus, the variation of couplant can greatly affect the received signals.

Table 1-1: Comparison of Different Non-destructive Weld Inspection Techniques

Techniques	Advantages	Disadvantages
VI	• Simple • Cost-effective	• Require training • Not good at internal quality
RI	• Good at internal voids and inclusions • Reliable	• Expensive • Hazardous to operator • Require training • Not suitable for online or in-service inspection
MPI	• Good at cracks • Mature	• Require pre-cleaning • Require demagnetization • Sensitivity dependent on crack orientation • Need further identification of defects
LPI	• Cost-effective • Good at cracks and pores • Mature	• Require pre and post cleaning • Require smooth surface • Not able to detect internal defects

ACFM	• Able to locate and size detect • Able to work through thin coatings	• Not good for small item and complex shapes • Can only detect cracks longer than 5 mm • Equipment bulky and expensive • Require training
ECT	• Instrument portable • Mature	• Only good at surface and subsurface defects • Require close access to inspected area • Sensitivity dependent on crack orientation
IRT	• Suitable for online inspection	• Indirect method • Not good at internal defect
UT	• Mature • Reliable • Able to detect both surface and internal defects	• Require liquid couplant • Require contact operation • Not suitable for moving sample and rough surface • Not suitable for high temperature environment

Table 1-1 summarizes the advantages and disadvantages of different non-destructive weld inspection techniques introduced previously. None of them is suitable for real-time measurement of WPDs. The ultrasonic testing technique is most promising compared with other techniques because of its capability to detect both surface and internal defects. However, the traditional transducers require the usage of liquid couplant, which greatly limit its application in real-time inspections.

1.3 Laser/EMAT Ultrasonic Technique

The Laser/EMAT ultrasonic (LEU) technique has drawn significant attentions [16, 17] for measuring WPDs. The LEU technique uses a pulsed laser to excite ultrasounds in specimens and an electromagnetic acoustic transducer (EMAT) to pick up signals. The laser-generated

ultrasounds interact with welds, and the acquired signals contain information about weld quality. The technique is most attractive for its non-contact operation.

Essentially, the LEU technique belongs to the family of ultrasonic testing techniques. Therefore, it inherits all the advantages of traditional UT techniques. Plus, both the laser generation [18-20] and the EMAT reception of ultrasounds are non-contact, which makes the technique suitable for moving samples, harsh environments, and automatic inspections. Because of the broadband nature of laser-generated ultrasounds, the complexity of acquired signals increases greatly, which makes it difficult to interpret signals. On the other hand, the laser generation of ultrasounds provides more flexibility since acquired signals contain different types of ultrasounds which can potentially be used to predict WPDs.

1.4 Motivation

Previous research has shown that the LEU technique is capable to measure WPDs effectively in thick structures [21-25]. In thick structures, laser-generated ultrasounds are primarily bulk waves and surface waves, which propagate in all directions, as shown in Fig. 1-3. WPDs can be determined by tracing different wave paths and measuring the time of flight (ToF) of ultrasounds following these paths [23]. The selected wave paths are closely interacting with the weld bead. WPDs have a closed form relationship with the measured time of flight.

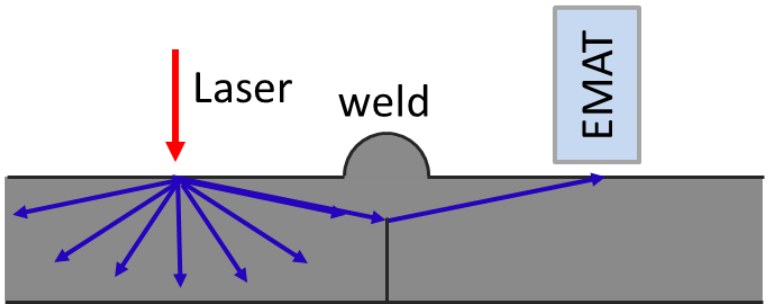

Fig. 1-3: LEU technique in thick structures

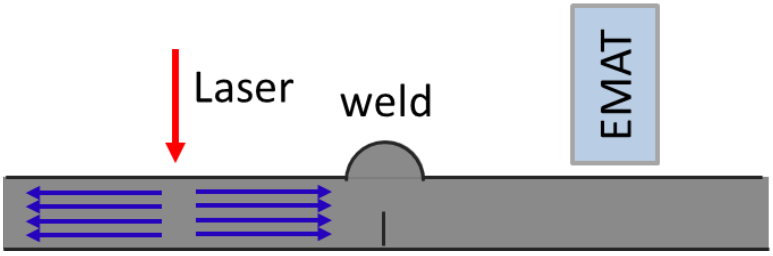

Fig. 1-4: LEU technique in thin structures

However, as the thickness of the structure decreases, Lamb waves [26-28] become dominant in laser-generated ultrasounds [20]. Lamb waves vibrate throughout the structure's thickness direction [29], as shown in Fig. 1-4, therefore the ray tracing and ToF-based method is no longer applicable in thin structures. New indicators need to be found from acquired signals to apply the LEU technique to measure WPDs in thin structures. There exist two major challenges. First, LEU signals in thin structures are very complicated. The ultrasonic signals contain broadband and multimodal Lamb waves, whose propagation speeds are frequency dependent. The waveform of acquired signals varies at different laser-to-EMAT distances. Second, the interaction of laser-generated Lamb waves with weld beads is unknown.

Previous research in our lab developed a method called superimposed laser sources which can create narrow band laser-generated Lamb waves. The reflection coefficients of selected Lamb waves were used to develop a regression model to predict WPDs in thin structures [30, 31]. However, the implementation of the method requires the laser source to move tens of times normal to the weld seam in order to measure the WPD at a single location along the weld. The

signal complexity is reduced by sacrificing experimental time, which makes the method not practical for weld inspections. The Lamb waves, whose reflection coefficients are used to develop the regression model, are preselected without knowing if they are sensitive to varying WPDs. Nevertheless, this pilot study does suggest that the reflection coefficients of laser-generated Lamb waves may contain information of WPDs in thin structures.

1.5 Research Objective

The objective of this research is to develop a fast and effective method to use the LEU technique to measure WPDs in thin structures. A systematic study will be conducted to accomplish the research objective from four major aspects. First, LEU signals in thin structures are characterized experimentally to establish a better understanding of laser-generated Lamb waves, which will be discussed in Chapter 3. Secondly, full wave field signals of laser-generated Lamb waves are measured to study their interactions with a local lack of penetration defect in thin structures, which will be discussed in Chapter 4. Thirdly, transmission coefficients of Lamb waves are investigated to see if they are able to predict WPDs quantitatively, which will be discussed in Chapter 5. Finally, the transmission coefficients of sensitive Lamb waves are used to develop a neural network to predict WPDs in thin structures, which will be discussed in Chapter 6.

CHPATER 2

Background

2.1 Laser Generation of Ultrasounds

When a pulsed laser is incident on a specimen, the temperature at the laser irradiation area increases dramatically. When the pulsed laser is turned off, the elevated temperature will dissipate quickly. This process induces a thermo-elastic stress, which serves as the source of laser-generated ultrasounds [32]. Due to the short duration of laser pulses (~ 10 ns), the excited ultrasounds are broadband in nature. A pulsed laser can be delivered to specimens through either optical lens and mirrors or optical fibers. Unlike traditional UT probes, the laser generation of ultrasound is non-contact and does not require any couplant.

Depending on the power density of the laser source, ultrasounds can be generated in three different regimes: thermo-elastic regime, transition regime, and ablation regime.

2.1.1 Thermo-elastic Regime

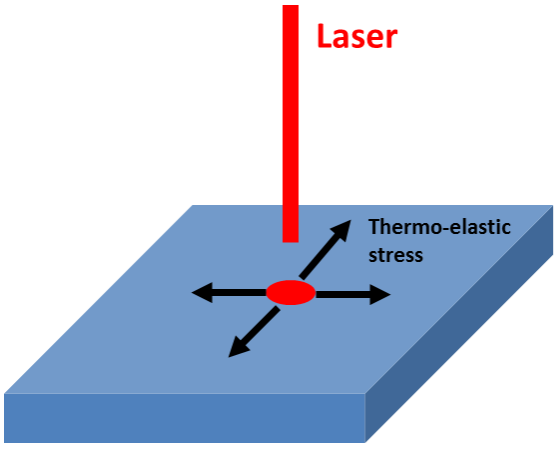

Fig. 2-1: Laser generation of ultrasounds in thermos-elastic regime

When the pulsed laser power is below certain threshold, the elevated temperature doesn't exceed the melting point of base material. In this regime, no damage is caused on the sample surface, and only thermos-elastic stress is induced, which is primarily parallel to the sample surface, as shown in Fig. 2-1.

2.1.2 Transition Regime

The transition regime is between the thermos-elastic regime and the ablative regime. Because of the narrow range of laser power, it is not very useful in practice.

2.1.3 Ablative regime

In the ablative regime, the pulsed laser power is high enough to cause vaporization of a thin layer of the top material. The vaporized material applies an additional normal stress on the specimen, as shown in Fig. 2-2. The ultrasounds generated in this regime have larger amplitudes than in the two other regimes. This work will primarily use the ablation regime to excite ultrasounds. Even though this regime will leave minor marks on samples, they are acceptable in most weld inspection applications.

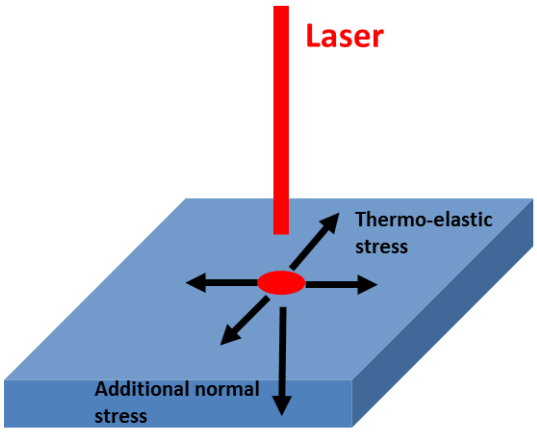

Fig. 2-2: Laser generation of ultrasounds in ablation regime

2.1.4 Directivity patterns of Laser-generated Bulk Waves

In thick structures, pulsed laser excites bulk and surface waves. The amplitudes of laser-generated longitudinal and shear waves are different in different directions. The directivity patterns of laser-generated bulk waves in different regimes have been studied both theoretically and experimentally [20, 33], as shown in Fig. 2-3 and Fig. 2-4.

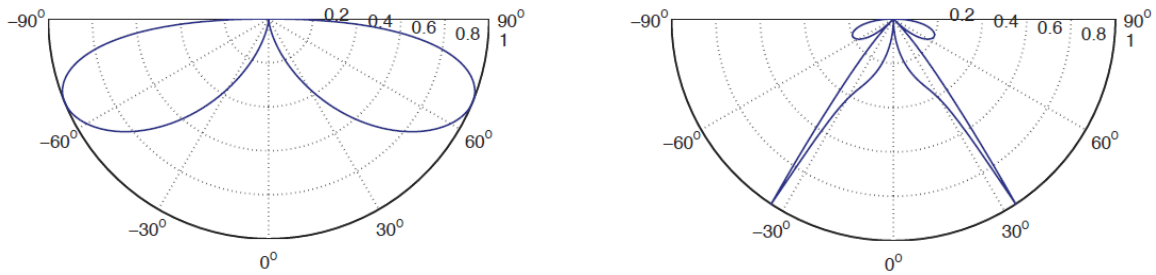

(a) (b)

Fig. 2-3: Directivity patterns of laser-generated (a) longitudinal and (b) shear waves in thermos-elastic regime

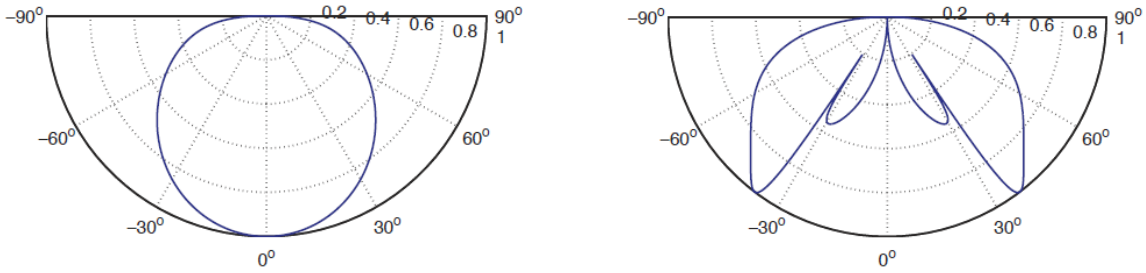

(a) (b)

Fig. 2-4: Directivity patterns of laser-generated (a) longitudinal and (b) shear waves in ablation regime

2.1.5 Pulsed Laser Used in This Work

This work uses a Continuum Lasers InliteTM II-20 pulsed Q-switched Nd: YAG laser to excite ultrasounds. The wavelength of the output laser is 1064 nm. The repletion rate of the laser is 20 pulses/sec. The laser pulse energy can be tuned from 0 to 250 mJ/pulse. The pulse width is about

7 ns. The laser has an external trigger which allows the control of the laser firing through an external TTL signal. Fig. 2-5 shows the photo of the laser used in this work.

Fig. 2-5: Photo of the laser

2.2 EMAT Reception of Ultrasounds

EMAT can be used to both generate and detect ultrasounds [34]. This work focuses only on EMAT's capability to detect ultrasounds. A schematic diagram of EMAT detecting ultrasounds is shown in Fig. 2-6. There is a permanent magnet inside EMAT, which creates a static magnetic field in the specimen. When ultrasounds propagate in the specimen, the particle vibration (v) interacts with the static magnetic field (B), and a current density (J) is established in the specimen. This induced current density is then detected by a pickup coil in EMAT through induction.

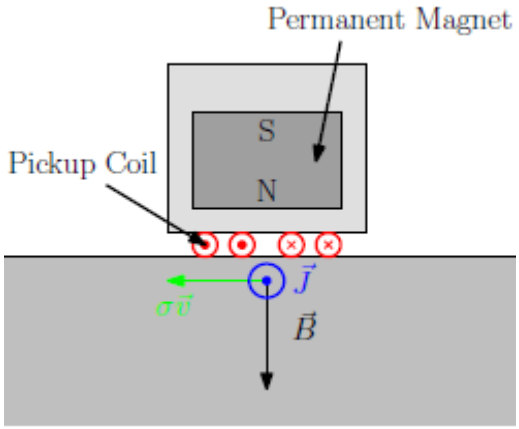

Fig. 2-6: Schematic of EMAT reception of ultrasounds

EMAT reception of ultrasounds is a non-contact process. EMAT has a larger detection area than traditional UT probes or laser interferometers due to the size of its pickup coil. The EMAT used in this work is custom-designed to be more sensitive to the in-plane particle motions in the specimen. Fig. 2-7 shows the photo of the EMAT used in this work. It has two wheels, which allow it to move easily along sample surfaces. It contains four pickup coils so that it can acquire four signals through its four channels simultaneously. The EMAT comes with a preamp which has a bandwidth from 0.5 MHz to 2.0 MHz. Fig. 2-8 shows the layout of the four pickup coils in the EMAT used in this work.

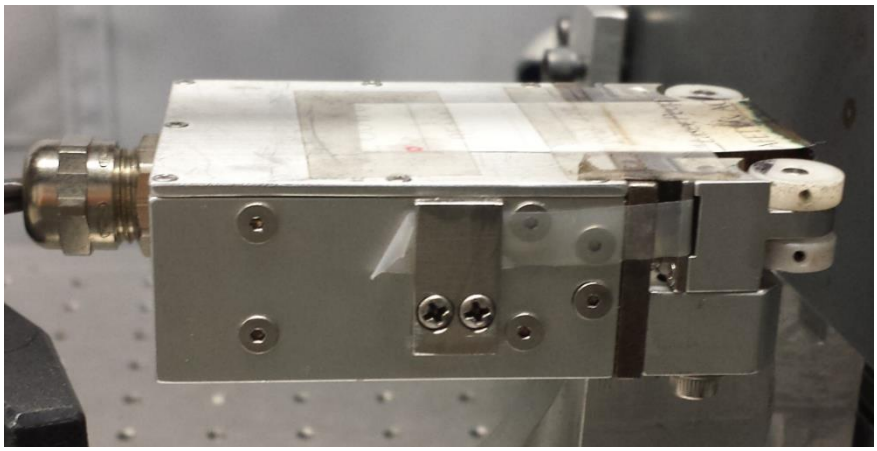

Fig. 2-7: Photo of EMAT used in this work

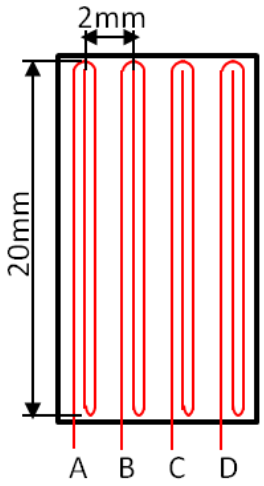

Fig. 2-8: Layout of pickup coils in EMAT

2.3 Laser/EMAT Ultrasonic Technique

The laser/EMAT ultrasonic technique uses a pulsed laser to generate and an EMAT to receive ultrasounds. Both the generation and the reception of ultrasounds are non-contact, which makes the technique very attractive. This technique belongs to the family of ultrasonic testing methods, which use ultrasounds to interrogate weld quality. Therefore, it inherits all the advantages of ultrasonic testing methods, such as reliability and capability to inspect both internal and surface defects.

2.4 WPD Inspection Using LEU Technique in Thick Structures

The LEU technique has been extensively studied for WPD inspections in thick structures. The laser source generates bulk waves and surface waves in thick structures, whose paths from the laser source to the EMAT receiver are traceable. WPDs can be measured by tracing different wave paths which closely interact with the weld bead. The ToF of waves following these paths can be used to determine WPDs through simple geometric calculations.

2.4.1 RGLS Method

The Rayleigh Generation Longitudinal to Shear (RGLS) method [24] is one of the ToF methods developed previously in our lab, which measures WPDs by tracing a specific wave path as shown in Fig. 2-9. The RGLS wave path consists of a shear wave reaching the bottom surface from the laser source, a Rayleigh wave propagating along the bottom surface and the crack between the two plates, a longitudinal wave converted from the weld bead root, and a shear wave converted from the bottom surface and finally reaching the EMAT receiver. The ToF of the waves following the RGLS path has an analytical relationship with the WPD.

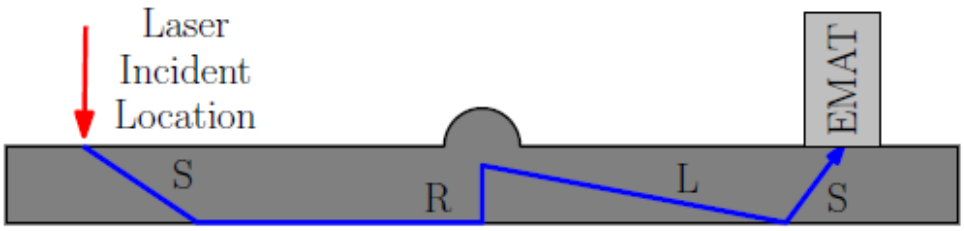

Fig. 2-9: RGLS wave path

2.5 WPD Inspection Using LEU Technique in Thin Structures

Application of the LEU technique for WPD inspection in thin structures has been limited by the complexity of laser-generated Lamb waves and the lack of effective signal interpretation methods. The laser-generated Lamb waves are broadband and contain multiple modes. The particle vibration induced by Lamb waves is throughout the thickness direction of structures. There is no internal traceable wave path in thin structures, therefore the ToF-based method cannot be used.

A method called superimposed laser sources was developed by previous students in our lab [31]. The method simplifies the laser-generated Lamb waves and uses reflection coefficients of preselected Lamb waves to predict WPDs. Fig. 2-10 shows how the superimposed laser sources method works. The laser beam is delivered though a cylindrical lens to create a line source on the sample. Measurement of the WPD at each location along the weld requires the line source to fire at a sequence of evenly spaced locations in the direction normal to the weld seam. The EMAT receives signals at the same location while the line source is moving. The received signals are stored in PC for post-processing. Signals generated at multiple line source locations with same intervals are shifted and added to obtain a narrow band Lamb wave signal. Changing the interval size can synthesize narrow band Lamb waves of different wavelengths. The reflection coefficients of synthesized Lamb waves are calculated and used to develop a regression model to predict WPDs. There are a few drawbacks about this method. First, the wavelengths that can be synthesized are only the multiples of the increment of the laser line sources, which is not flexible. Secondly, the wavelengths are preselected without knowing if the synthesized Lamb waves are sensitive to the varying WPDs or not. Thirdly, the implementation of this method is not efficient because the laser line source needs to move at multiple locations in order to measure the WPD at a single location along the weld seam.

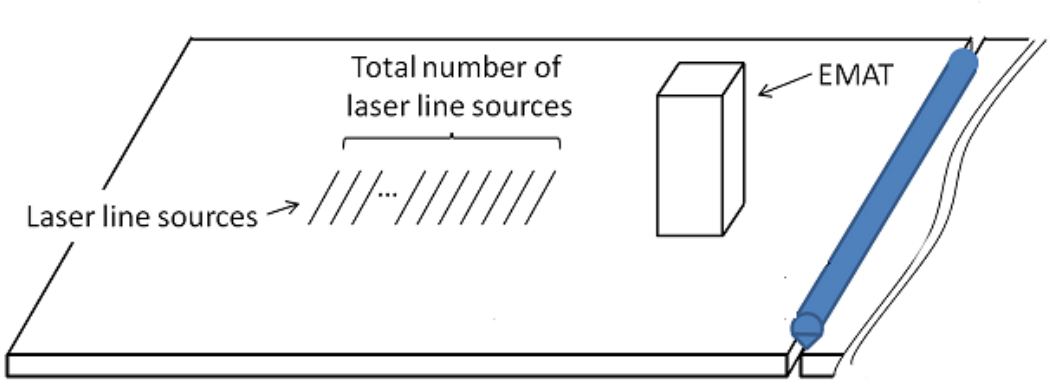

Fig. 2-10: Diagram of superimposed laser sources method

2.6 Lamb Waves

Lamb waves are elastic waves that propagate in plate structures. Lamb waves can travel longer distances with less attenuation than bulk waves, and they are dispersive because Lamb waves of different frequencies travel with different speeds.

2.6.1 Rayleigh-Lamb Equations

Lamb waves are governed by Rayleigh-Lamb Equations, as shown in Eq. 2-1 and 2-2,

$$\frac{tan(qh)}{tan(ph)} = -\frac{4k^2pq}{(q^2-k^2)^2} \quad \textbf{(Eq. 2-1)}$$

$$\frac{tan(qh)}{tan(ph)} = -\frac{(q^2-k^2)^2}{4k^2pq} \quad \textbf{(Eq. 2-2)}$$

where h is the half thickness of the plate, k is the radian wave-number, p and q are parameters defined in Eq. 2-3 and 2-4:

$$q^2 = \frac{\omega^2}{c_T^2} - k^2 \quad \textbf{(Eq. 2-3)}$$

$$p^2 = \frac{\omega^2}{c_L^2} - k^2 \qquad \textbf{(Eq. 2-4)}$$

where ω is the radian frequency, c_T is the shear speed, and c_L is the longitudinal speed. Eq. 2-1 represents the equation for symmetric modes, and Eq. 2-2 represents the equation for antisymmetric modes. These two equations define the relationships between the wavenumber and frequency of waves that can propagate in plate structures. Both equations have an infinite number of solutions, which are pairs of wavenumber and frequency. The real-valued solutions of Rayleigh-Lamb Equations constitute dispersive curves in the frequency-wavenumber domain. Fig. 2-11 shows the dispersive curves of several low modes in a 2.5 mm thick steel plate. The solid lines represent symmetric modes, which are solutions of the symmetric equation. The dashed lines represent antisymmetric modes, which are solutions of the antisymmetric equation.

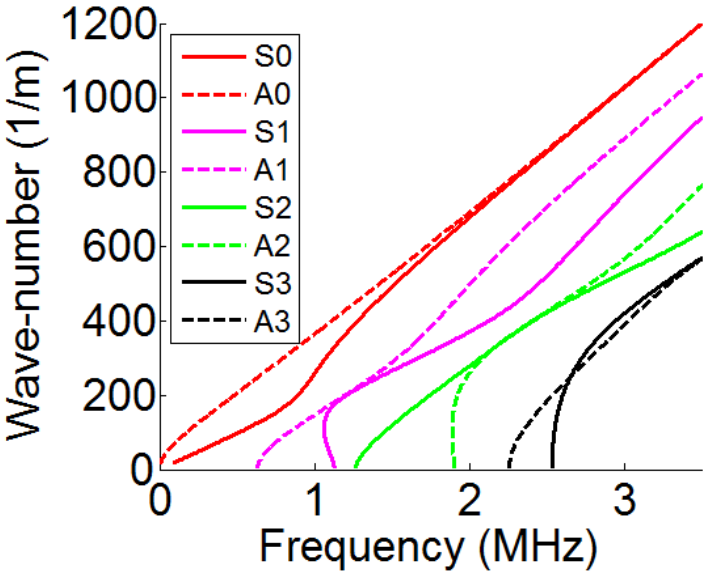

Fig. 2-11: Dispersive curves in frequency-wavenumber domain

The group velocity of Lamb waves can be calculated using Eq. 2-5. The dispersive curves of Lamb waves in a 2.5 mm thick steel plate in the group velocity-frequency domain are shown in

Fig. 2-12. For each Lamb wave mode, different frequencies propagate with different velocities, which is the dispersive property of Lamb waves. This is one of the reasons why the laser-generated Lamb waves are complicated.

$$c_g = \frac{\partial \omega}{\partial k} \quad \textbf{(Eq. 2-5)}$$

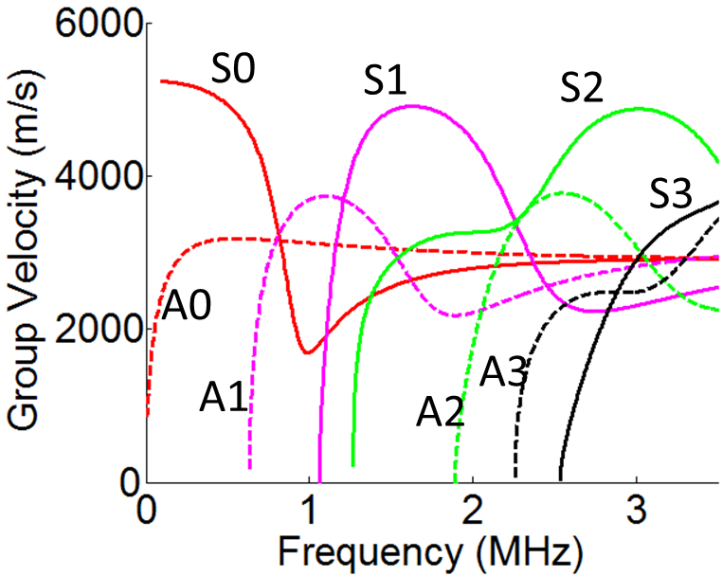

Fig. 2-12: Dispersive curves in group velocity-frequency domain

2.6.2 Lamb Wave Displacement Field

Each point on dispersive curves defines a unique displacement field. The displacements of Lamb waves are defined as below:

For symmetric modes:

$$u_1 = \{ikA_2 \cos(px_2) + qB_1 \cos(qx_2)\}\exp[i(kx_1 - \omega t)] \quad \textbf{(Eq. 2-6)}$$

$$u_2 = \{-pA_2 \sin(px_2) - ikB_1 \sin(qx_2)\}\exp[i(kx_1 - \omega t)] \quad \textbf{(Eq. 2-7)}$$

For antisymmetric modes:

$$u_1 = \{ikA_1\, sin(px_2) - qB_2\, sin(qx_2)\}exp[i(kx_1 - \omega t)] \quad \textbf{(Eq. 2-8)}$$

$$u_2 = \{pA_1\, cos(px_2) - ikB_2\, cos(qx_2)\}exp[i(kx_1 - \omega t)] \quad \textbf{(Eq. 2-9)}$$

where u_1 stands for the in-plane displacement, u_2 stands for the out-of-plane displacement, A_1, A_2, B_1 and B_2 are coefficients which must satisfy Eq. 2-10 and Eq. 2-11. Fig. 2-13 shows the coordinate system used in this work.

$$\frac{A_2}{B_1} = \frac{(k^2 - q^2)\sin(qh)}{2ikpsin(ph)} \quad \textbf{(Eq. 2-10)}$$

$$\frac{A_1}{B_2} = -\frac{(k^2 - q^2)\cos(qh)}{2ikpcos(ph)} \quad \textbf{(Eq. 2-11)}$$

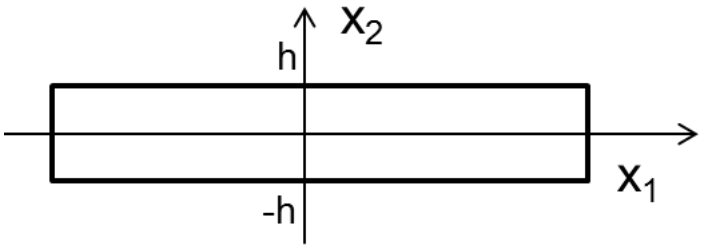

Fig. 2-13: Coordinate system used in this work

The exponential terms in Eq. 2-6 to 2-9 indicate that Lamb waves propagate in directions parallel to the plate surface, which is why there is no internal wave path to trace in thin structures. The amplitude terms in Eq. 2-6 to 2-9 indicate that the displacement amplitudes of Lamb waves are functions of x_2, known as the Lamb wave mode shape. Fig. 2-14 shows two example mode shapes, one for a symmetric mode, the other for an antisymmetric mode. Table 2-1 summarizes

the features of mode shapes of Lamb waves. The in-plane displacements of symmetric modes are symmetric in the thickness direction, while the out-of-plane displacements of symmetric modes are inverse symmetric in the thickness direction. The in-plane displacements of antisymmetric modes are inverse symmetric in the thickness direction, while the out-of-plane displacements of antisymmetric modes are symmetric in the thickness direction. Snapshots of displacement fields of two example Lamb waves are shown in Fig. 2-15.

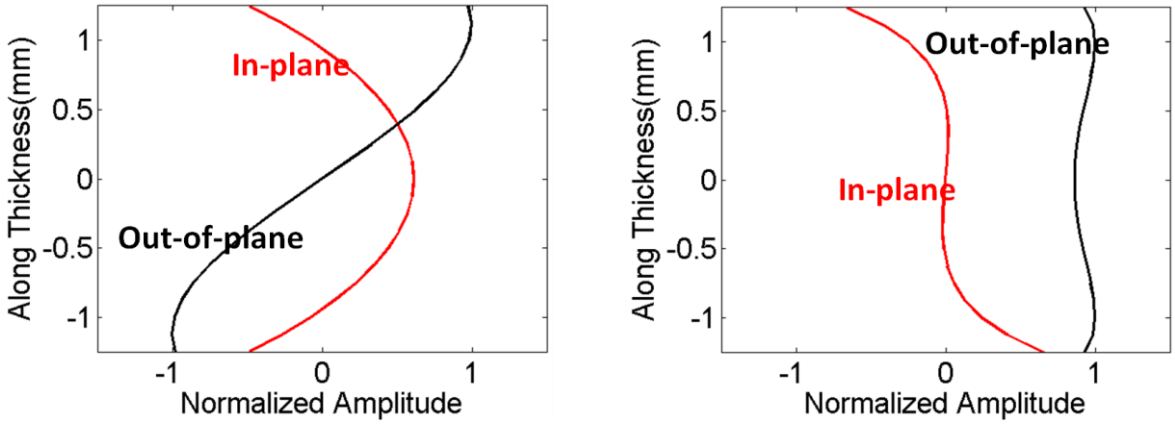

(a) S0 mode at 1.08 MHz

(b) A0 mode at 1.08 MHz

Fig. 2-14: Example mode shapes of Lamb waves in 2.5 mm thick steel plate

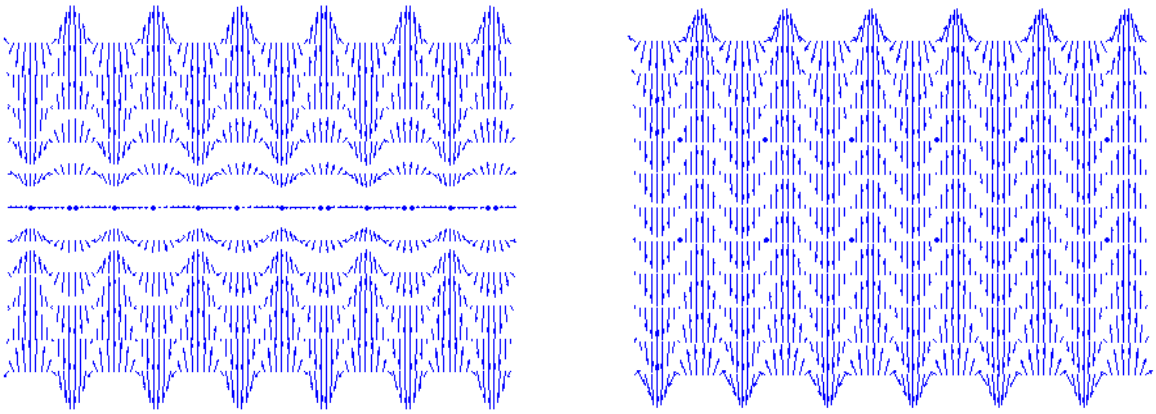

(a) S0 mode at 1.08 MHz (b) A0 mode at 1.08 MHz

Fig. 2-15: Snapshots of example displacement fields of Lamb waves in 2.5 mm thick steel plate

Table 2-1: Properties of mode shapes of symmetric and antisymmetric modes

	In-plane displacement	Out-of-plane displacement
Symmetric modes	symmetric	Inverse symmetric
Antisymmetric modes	Inverse symmetric	symmetric

2.6.3 Effect of Structure Thickness on Laser-generated Ultrasounds

As mentioned previously, laser-generated ultrasounds differ in thin and thick structures. The effect of structure thickness on laser-generated ultrasounds can be viewed by plotting dispersive curves of Lamb wave modes of interest in the group velocity-frequency domain for different thicknesses, as shown in Fig. 2-16. At thinner thicknesses, the group velocities of several low Lamb wave modes vary greatly within the frequency range of interest [0.5MHz, 2.0MHz]. As the thickness increases, the dispersive portions of Lamb waves are squeezed into the low frequencies and eventually out of the frequency range of interest when the thickness is large enough. Therefore, at thin thicknesses, the dispersion of laser-generated ultrasounds is prominent within

the frequency range of interest. As the thickness increases, the dispersion of laser-generated ultrasounds within the frequency range of interest reduces and can be ignored when the thickness is large enough. When the thickness increases to infinite, the group velocities of all Lamb wave modes converge to a constant value, which is the Rayleigh wave velocity.

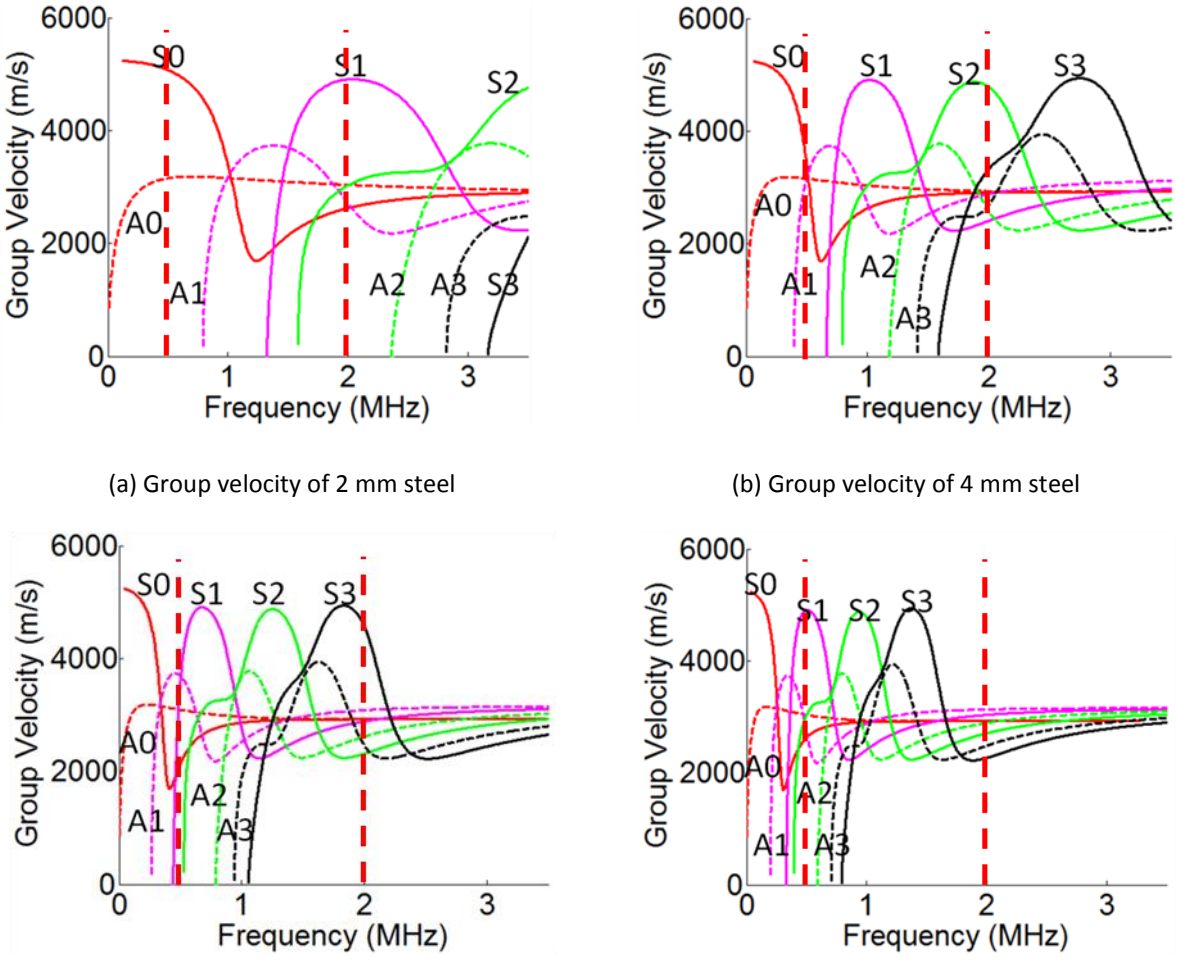

(a) Group velocity of 2 mm steel

(b) Group velocity of 4 mm steel

(c) Group velocity of 6 mm steel

(d) Group velocity of 8 mm steel

Fig. 2-16: Effect of thickness on group velocities

2.6.4 Evanescent Waves

Rayleigh-Lamb Equations also have solutions with complex-valued wavenumbers. When the wavenumber is complex, it can be written in the following form.

$$k = a + bi \quad \textbf{(Eq. 2-12)}$$

Then the displacement field becomes:

$$u_1 = Ae^{i(kx_1 - \omega t)} = Ae^{-bx_1}e^{i(ax_1 - \omega t)} \quad \textbf{(Eq. 2-13)}$$

$$u_2 = Be^{i(kx_1 - \omega t)} = Be^{-bx_1}e^{i(ax_1 - \omega t)} \quad \textbf{(Eq. 2-14)}$$

where Ae^{-bx_1} and Be^{-bx_1} represent the amplitude terms for the in-plane and out-of-plane displacements, respectively. The amplitudes of these waves decrease exponentially with their propagation distance. They are called evanescent waves. Evanescent waves are very local and difficult to be detected.

2.7 Continuous Wavelet Transform

Continuous wavelet transform (CWT) uses inner products to compare the similarity between a signal and the shifted and dilated versions of selected wavelets [35, 36]:

$$C(a,b) = \int_{-\infty}^{\infty} f(t) \frac{1}{\sqrt{a}} \psi^* \left(\frac{t-b}{a}\right) dt \quad \textbf{(Eq. 2-15)}$$

where $f(t)$ is the signal under investigation, $\psi(t)$ is the mother wavelet, and $\frac{1}{\sqrt{a}}\psi^*\left(\frac{t-b}{a}\right)$ is the complex conjugate of the wavelet shifted to position b and dilated by scale a. The scale has a general but not precise inverse relationship with frequency. The calculated CWT coefficient $C(a,b)$ provides a pseudo time-frequency representation of the original signal. The choice of mother wavelet depends on its capability to capture signal features of interest. MATLAB Wavelet Toolbox provides convenient functions and wide options of wavelets to perform CWT analysis.

In this work, CWT provides an effective way to study individual LEU signals. Different Lamb waves present in LEU signals can be separated in their time-frequency domain representation. This work uses complex-valued Morlet wavelet as the mother wavelet, which is defined in Eq. 2-16.

$$\psi(t) = \frac{1}{\sqrt{\pi F_b}} e^{2i\pi F_c t} e^{-\frac{t^2}{F_b}} \quad \textbf{(Eq. 2-16)}$$

where the parameter F_c represents the wavelet center frequency, and the parameter F_b represents the wavelet bandwidth in the time domain. These two parameters are determined depending on the features of signals which are to be analyzed. Fig. 2-17 shows plots of the complex-valued Morlet wavelets with different parameters.

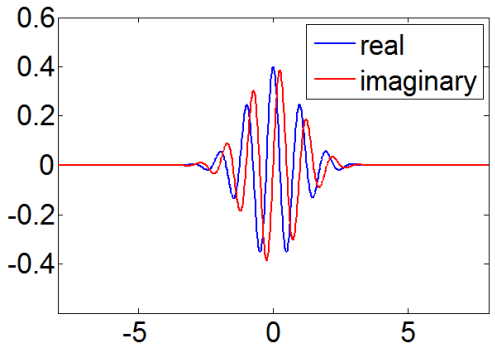

(a) Fc = 1 and Fb = 2

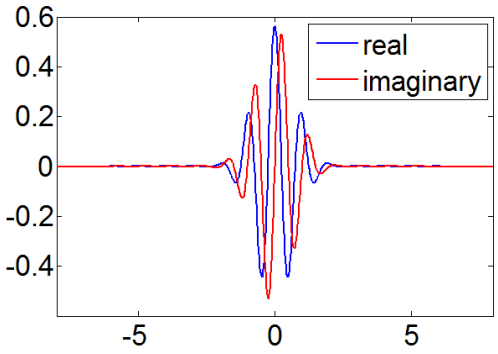

(b) Fc = 1 and Fb = 1

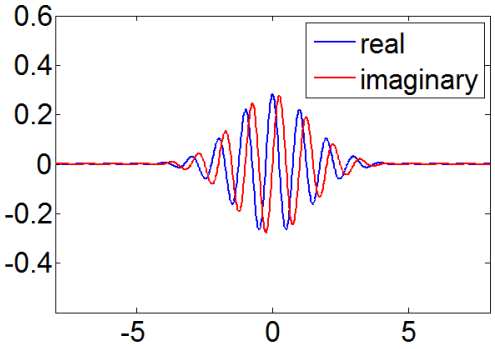

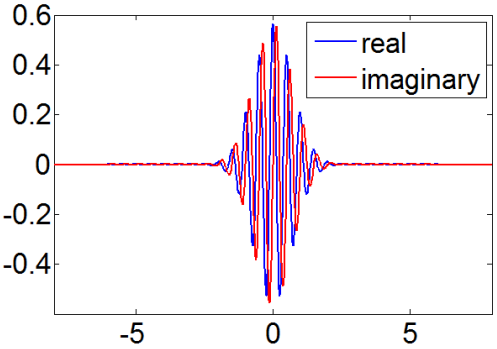

(c) Fc=1 and Fb=4

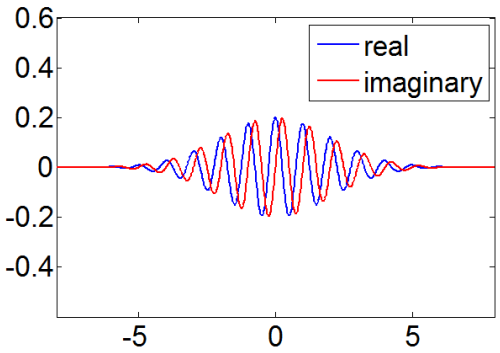

(d) Fc = 2 and Fb = 1

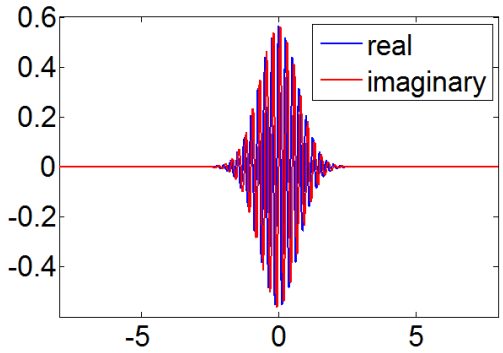

(e) Fc=1 and Fb=8

(f) Fc = 4 and Fb = 1

Fig. 2-17: Plots of complex-valued Morlet wavelet with different parameters

2.8 Multidimensional Fourier Transform

Fourier Transform (FT) converts signals from the time or spatial domain to the frequency domain. Multidimensional FT is the extension of the one dimensional definition:

$$F(\omega_1, \omega_2, \omega_3, \dots \omega_n) = \int_{-\infty}^{\infty} \dots \int_{-\infty}^{\infty} e^{-2\pi i(x_1\omega_1 + x_2\omega_2 \dots + x_n\omega_n)} f(x_1, \dots, x_n) dx_1 dx_2 \dots dx_n \quad \textbf{(Eq. 2-17)}$$

where f stands for a multidimensional signal, F stands for the multidimensional FT coefficient, and n stands for the dimension. In this work, 2-D and 3-D FT will be used. 2-D FT is effective to analyze B-scan signals, and 3-D FT is effective to analyze C-scan signals.

2.8.1 2-D FT

A one dimensional wave can be represented by

$$S(x,t) = Ae^{i(kx-\omega t)} \quad \textbf{(Eq. 2-18)}$$

where A represents the wave amplitude, k is the wavenumber, and ω is the radian frequency. The wave direction is determined by the signs of k and ω. For example, if k and ω are both positive, the function represents waves propagating in the positive x direction. 2-D FT converts

signals of a one dimensional wave to coefficients in the wavenumber-frequency domain [37, 38]. In digital signal processing, the calculated 2-D FT coefficient $F(k, \omega)$ is periodic in both wavenumber and frequency directions. Fig. 2-18 shows the cycle centered at the origin. Within this cycle, the 2-D FT coefficient is conjugate symmetric about the origin. Waves propagating in different directions are automatic separated in the wavenumber-frequency domain. The 2-D FT coefficients located in quadrants I and III correspond to waves propagating in the positive x direction, and the coefficients located in quadrants II and IV correspond to waves propagating in the negative x direction.

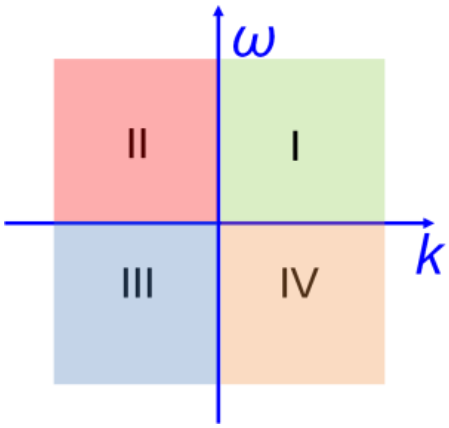

Fig. 2-18: 2-D FT coefficient in wavenumber–frequency domain

2.8.2 3-D FT

A two dimensional wave can be represented by

$$S(x, y, t) = Ae^{i(k_x x + k_y y - \omega t)} \quad \textbf{(Eq. 2-19)}$$

where A represents the wave amplitude, k_x is the wavenumber in the x direction, k_y is the wavenumber in the y direction, and ω is the radian frequency. The wave direction is determined by signs of k_x, k_y, and ω. For example, if k_x, k_y, and ω are all positive, the function represents waves propagating in the positive x and positive y directions.

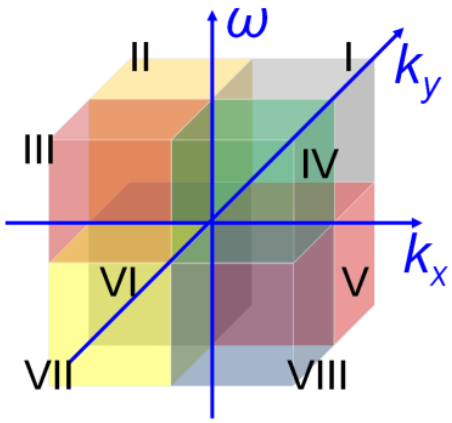

Fig. 2-19: 3-D FT coefficients in k_x - k_y - ω domain

3-D FT converts signals of a two dimensional wave to coefficients in the k_x - k_y - ω domain [39-41]. In digital signal processing, the calculated 3-D FT coefficient $F(k_x, k_y, \omega)$ is periodic in all three dimensions. Fig. 2-19 shows the cycle centered at the origin. Within this cycle, the 3-D FT coefficient is conjugate symmetric about the origin. Two dimensional waves propagating in different directions are automatic separated in the k_x - k_y - ω domain. The 3-D FT coefficients located in different octants correspond to waves propagating in different directions. The mapping relationship is summarized in Table 2-2.

Table 2-2: Relationship between wave direction and 3-D FT coefficient

Wave direction	3-D FT coefficient	Wave direction	3-D FT coefficient
Positive x, Positive y	Octant I and VII	Positive x	Surface shared by octant I and IV Surface shared by octant VI and VII
Positive x, Negative y	Octant IV and VI	Negative x	Surface shared by octant II and III Surface shared by octant V and VIII
Negative x, Positive y	Octant II and VIII	Positive y	Surface shared by octant I and II Surface shared by octant VII and VIII
Negative x, Negative y	Octant III and V	Negative y	Surface shared by octant III and IV Surface shared by octant V and VI

CHAPTER 3

Characterization of Laser-Generated Lamb Waves

The first challenge which limits applications of the LEU technique to measure WPDs in thin structures is that laser-generated ultrasounds are very complicated due to the broadband nature of laser excitation. In thin structures, the LEU signals become more complicated. The laser-generated Lamb waves may contain multiple modes. Lamb waves are dispersive, that is, the wave forms of received LEU signals vary at different laser-to-EMAT distances. The EMAT receiver used in the LEU system may also affect the received signals since it is more sensitive to the in-plane particle motions.

The systematic study starts with characterizing the Lamb wave signals acquired using the LEU technique. In this chapter, a B-Scan procedure is conducted on a thin plate, and the acquired signals reveal a wealth of information about the Lamb waves present in the LEU signals. This preliminary study helps to establish a better understanding of the acquired LEU signals in thin structures.

3.1 Experimental Setup

The B-scan procedure is conducted on a defect-free 2.5 mm thick A36 steel plate. The material properties of the A36 steel plate are listed in Table 3-1. The inspection procedure is shown in Fig. 3-1. The pulsed laser repeatedly fires at the same location, and the EMAT picks up signals at 251 evenly spaced locations at increments of 0.4 mm. The laser pulse is delivered through a convex lens and focused to a point source with a radius of 0.4 mm on the plate surface. The laser power

is tuned to 115 mJ/pulse, which excites ultrasounds in the ablative regime. The sampling frequency is set to 12.5 MHz based on Nyquist–Shannon sampling theorem. At each EMAT location, the laser fires 16 times, and the acquired signals are averaged later to improve the signal to noise ratio (SNR).

Table 3-1: Material properties of A36 steel plate

Young's modulus	Poisson ratio	density	Shear speed	Longitudinal speed
200 GPa	0.32	7800 kg/m^3	3116.5 m/s	6057.4 m/s

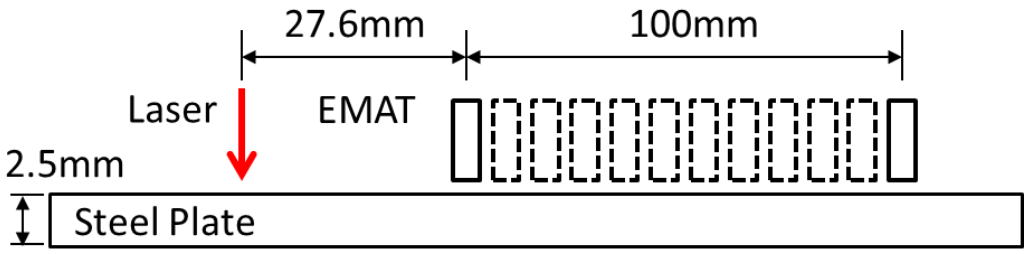

Fig. 3-1: B-Scan procedure of defect free steel plate

3.2 Characterization in Wavenumber-Frequency Domain

Fig. 3-2 shows the compilation of the 251 averaged signals based on their acquisition locations. 2-D FT converts the B-scan signals to the k - ω domain [38, 42], and Fig. 3-3 (a) shows the calculated 2-D FT coefficients. The x axis represents frequency, and the y axis represents wavenumber. The color represents the magnitude of the calculated 2-D FT coefficients. Fig. 3-3 (b) shows the theoretical dispersive curves of a 2.5 mm thick A36 steel plate in the k - ω domain. Dispersive curves of different Lamb waves are observed in the plot of the calculated 2-D FT coefficient, which confirms that the laser-generated ultrasounds in the 2.5 mm thick steel plate are Lamb waves. Comparison with the theoretical dispersive curves helps to identify the Lamb

waves present in the received signals, as labeled in Fig. 3-3 (a). Broadband and multi-modal Lamb waves are generated by laser in the steel plate. Along each curve in Fig. 3-3 (a), the color varies, which indicates that for each observed Lamb wave mode in LEU signals, the amplitude is not uniform across frequencies. This can be explained by the facts that laser-generated Lamb waves are not uniform and that the EMAT is more sensitive to Lamb waves with large in-plane motions at the plate surface.

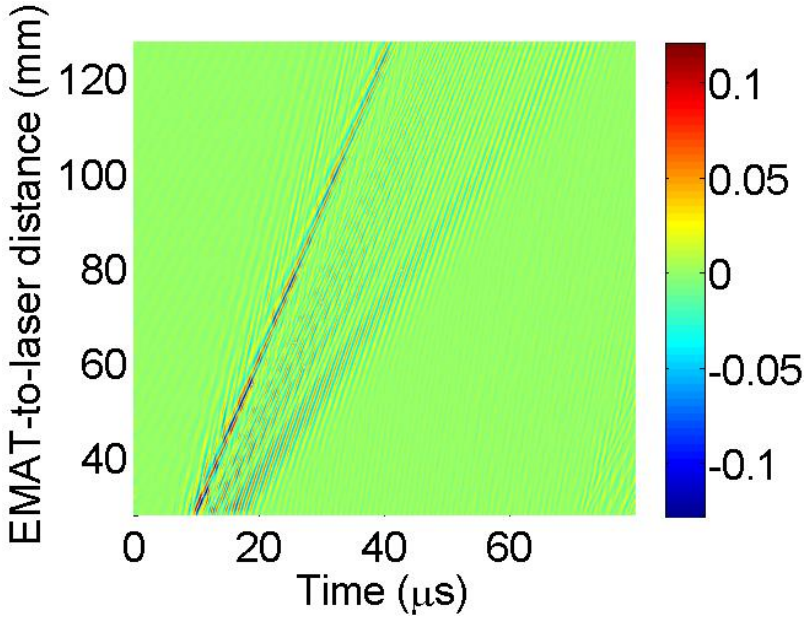

Fig. 3-2: Time-space representation of B-scan signals

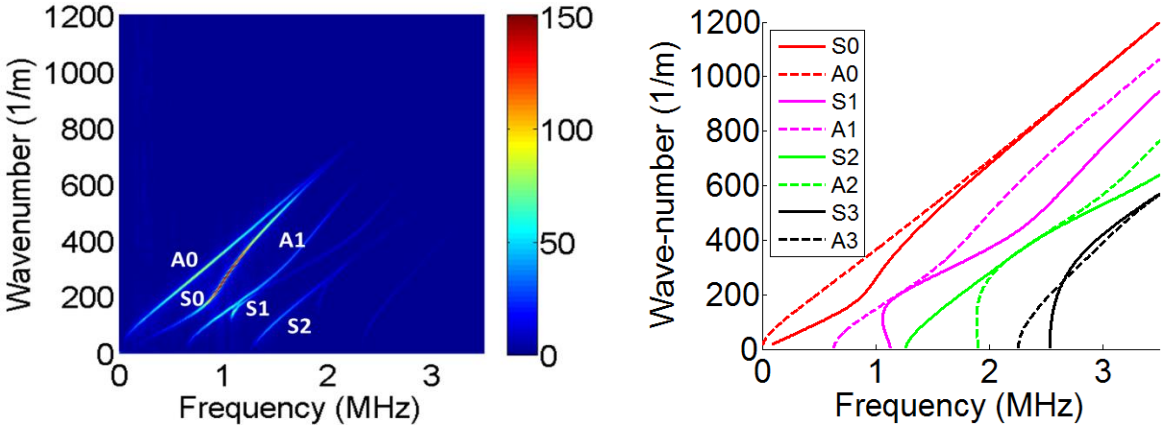

(a) 2-D FT of B-scan signals

(b) Theoretical dispersive curves of 2.5 mm thick steel plate

Fig. 3-3: Dispersive curves in wavenumber-frequency domain

Even though the EMAT used in this work has a nominal bandwidth from 0.5 MHz to 2.0 MHz, Lamb waves beyond this frequency range are also observed in the LEU signals. However, their amplitudes are very small. Future study will only focus on the strong Lamb waves observed within the EMAT bandwidth. They are A0, S0, A1, S1 and S2 modes.

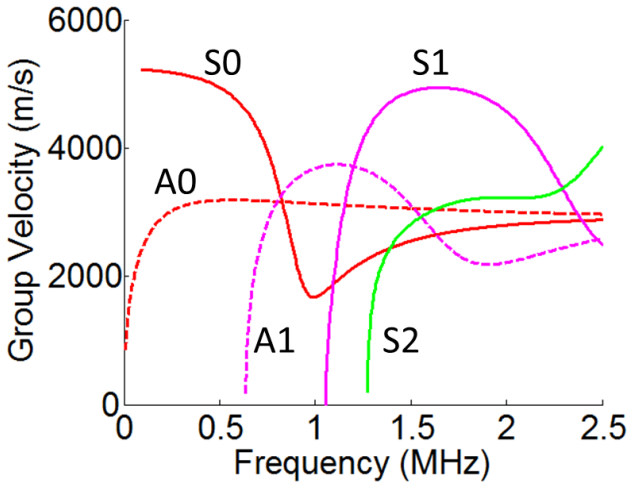

Fig. 3-4: Group velocities of A0, S0, A1, S1 and S2 modes in 2.5 mm thick steel plate

3.2.1 A0 Mode

The wavenumber of A0 mode within the EMAT bandwidth is from about 204 m^{-1} to 688.6 m^{-1}. The corresponding wavelength is from about 4.9 mm to 1.5 mm. The corresponding group velocity changes from about 3185 m/s to 3005 m/s. Therefore, the observed A0 mode in the LEU signals are not very dispersive, that is, the velocity doesn't change much across different frequencies within the EMAT bandwidth, which can be seen from Fig. 3-4.

3.2.2 S0 Mode

For S0 mode, the wavenumber within the EMAT bandwidth is from about 97.5 m^{-1} to 674 m^{-1}. The corresponding wavelength is from about 10.3 mm to 1.5 mm. The corresponding group velocity starts from about 4945 m/s, decreases to 1676 m/s, and then increases to 2798 m/s, as shown in Fig. 3-4. Therefore, the observed S0 mode in the LEU signals are very dispersive. Fig. 3-3 (a) shows that the amplitude of S0 mode is especially strong between 0.9 MHz and 1.3 MHz. Across this frequency range, the group velocity varies a lot. Therefore, and the S0 mode in the received LEU signals will expand in the time domain as it propagates further distances.

3.2.3 A1 Mode

In 2.5 mm thick steel plate, A1 mode has a cut-off frequency of 0.636 MHz. The wavenumber within the EMAT bandwidth is from 0 m^{-1} to 491 m^{-1}. The corresponding wavelength is from positive infinite to 2 mm. The corresponding group velocity increases from 0 m/s to 3745 m/s, then decreases to 2184 m/s, and finally increases to 2213 m/s, as shown in Fig. 3-4. Fig. 3-3 (a) shows that the strongest A1 mode appears at frequencies from 0.9 MHz to 1.3 MHz. Even though the A1 mode is very dispersive across the entire EMAT bandwidth, its group velocity doesn't vary a lot within the frequency range where its strongest amplitude is observed. Therefore, the A1 mode Lamb wave observed in the received LEU signals is not very dispersive.

3.2.4 S1 Mode

In 2.5 mm thick steel plate, S1 mode has a cut-off frequency of 1.117MHz, as shown in Fig. 3-3 (b). Its wavenumber from the cut-off frequency to 2.0 MHz values from 0 m^{-1} to 370 m^{-1}. The corresponding wavelength is from positive infinite to 2.7 mm. The corresponding group velocity starts from a negative value, then increase to 4943 m/s, and finally decreases to 4575 m/s. The

frequency at which the group velocity changes from negative to positive is about 1.054 MHz. In fact, the frequency range where the group velocity exhibits negative values belongs to a backward propagating mode, S2b, which is connected to S2 mode through a small imaginary loop in the ω(k) space [43]. Only the S1 mode Lamb waves with positive group velocities are observed in the received LEU signals, as shown in Fig. 3-3 (a), which have wavenumbers from 116 m^{-1} to 370 m^{-1} and corresponding wavelengths from 8.6 mm to 2.7 mm. S1 mode is also very dispersive. However, S1 mode is much weaker compared with the previous three modes.

3.2.5 S2 Mode

The S2 mode has a cut-off frequency of 1.273 MHz, from which to 2.0 MHz its wavenumber values from 0 m^{-1} to 278 m^{-1}. The corresponding wavelength is from positive infinite to 3.6 mm. The corresponding group velocity increases from 0 m/s to 3228 m/s, which is dispersive. S2 mode is even weaker than S1 mode.

Table 3-2 summarizes the properties of the Lamb waves observed in the LEU signals.

Table 3-2: Properties of Lamb waves observed in LEU signals

Lamb wave mode	Frequency range	Wavenumber	Wavelength	Group velocity
A0	0.5 – 2.0 MHz	204 - 688.6 m^{-1}	4.9 - 1.5 mm	3185 - 3005 m/s
S0	0.5 – 2.0 MHz	97.5 - 674 m^{-1}	10.3 - 1.5 mm	4945 - 1676 - 2798 m/s
A1	0.636 – 2.0 MHz	0 - 491 m^{-1}	+∞ - 2 mm	0 - 3745 - 2184 - 2213 m/s
S1	1.504 – 2.0 MHz	116 - 370 m^{-1}	8.6 - 2.7 mm	0 - 4943 - 4575 m/s
S2	1.273 – 2.0 MHz	0 - 278 m^{-1}	+∞ - 3.6 mm	0 - 3228 m/s

3.3 Characterization in Time-Frequency Domain

2-D FT is a very effective to characterize Lamb waves in the received LEU signals because different laser-generated Lamb waves are separated in the wavenumber-frequency domain. However, it requires LEU signals acquired at multiple evenly spaced locations. Practically, it would be more helpful to identify Lamb waves from individual LEU signals. Traditional frequency spectrum analysis is not suitable for LEU signals because different Lamb waves are overlapping in the frequency domain. CWT provides an effective way to analyze individual LEU signals [44, 45]. CWT converts temporal signals to the time-frequency domain, in which different Lamb waves are separated because of their different speeds. The complex-valued Morlet wavelet is used as the mother wavelet due to the similarity of its waveform to the LEU signals. Proper parameters need to be selected to capture different Lamb waves in the LEU signals.

Fig. 3-5 shows an LEU signal acquired when the EMAT receiver is 64 mm away from the laser source. Fig. 3-6 shows two versions of complex-valued Morlet wavelets used in this work. The waveform of the first wavelet is similar to the waveform observed at the beginning of the LEU signal, which oscillates a lot in a short period. The waveform of the second wavelet is similar to the waveform observed later in the LEU signal, which is smoother and long-lasting.

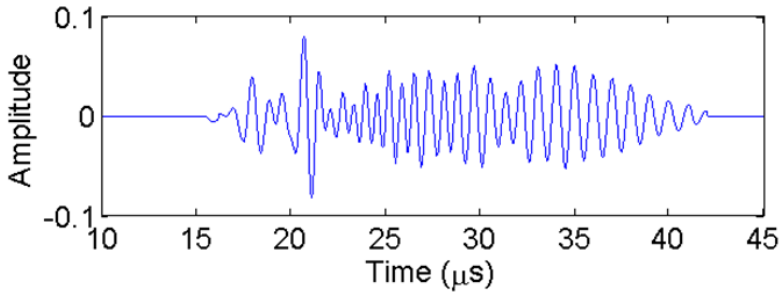

Fig. 3-5: LEU signal acquired when EMAT is 64 mm away from laser source

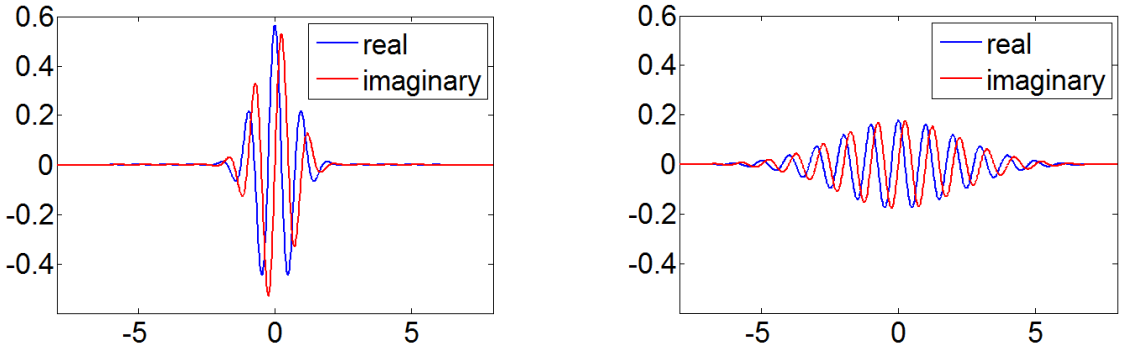

(a) Complex-valued Morlet (Fb=1, Fc=1) (b) Complex-valued Morlet (Fb=6, Fc=1)

Fig. 3-6: Complex-valued Morlet parameters selected for CWT

Fig. 3-7 shows the CWT coefficients of the LEU signal in the time-frequency domain using the two different versions of complex-valued Morlet wavelets. The theoretical arrival times of Lamb waves identified in the previous section are calculated using Eq. 3-1 and superimposed to both CWT plots.

$$T = \frac{D}{C_g} \qquad \textbf{(Eq. 3-1)}$$

where D is the distance from the laser source to the EMAT receiver, and C_g is the group velocity of Lamb waves. The superimposed dispersive curves help to identify different Lamb waves in the LEU signals from the time-frequency domain. Fig. 3-7 (a) shows that the first complex-valued Morlet wavelet is good at identifying the A0 mode and that it can also identify the S0 mode, which arrives after the A0 mode. Fig. 3-7 (b) shows that the second complex-valued Morlet wavelet captures the A0 mode poorly but is better at identifying the S0 mode when compared with the first complex-valued Morlet wavelet. In the time-frequency domain, the most outstanding Lamb waves that can be identified are A0 and S0 modes. The other Lamb waves modes that are identified in the wavenumber-frequency domain are not as outstanding as the

S0 and A0 modes. This is because the wavenumber-frequency domain representation requires LEU signals acquired at multiple locations. It contains both time and space information and therefore has a higher resolution. Nevertheless, the time-frequency domain representation is derived from a single LEU signal and therefore has a limited resolution. In fact, different Lamb waves cannot be completely separated in the time-frequency domain. For example, in some regions dispersive curves of different Lamb waves are close to or even intersect with each other. The other Lamb waves are not as outstanding because they may be obscured by the strong A0 and S0 modes.

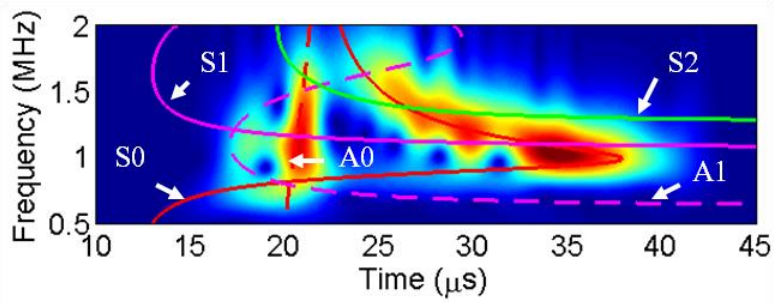

(a) CWT using complex-valued Morlet with Fb=1 and Fc=1

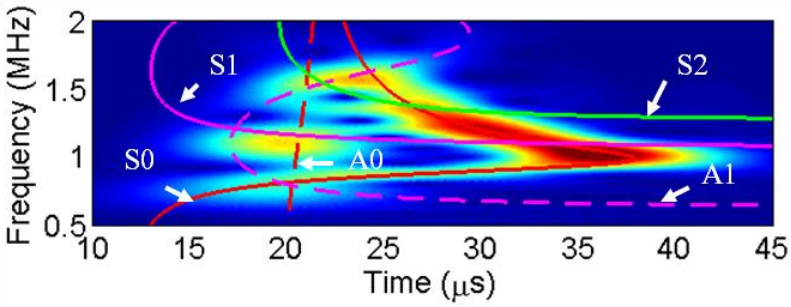

(b) CWT using complex-valued Morlet with Fb=6 and Fc=1

Fig. 3-7：CWT plots with dispersive curves superimposed

CWT helps to obtain a better understanding of the waveform of the LEU signal in the time domain. The short strong oscillation primarily corresponds to A0 mode Lamb wave, which has a

fast speed and is less dispersive. The long-lasting gentle oscillation primarily corresponds to S0 mode, which travels slower than A0 mode and is very dispersive. The waveform corresponding to A0 mode is relatively consistent as the laser-to-EMAT distance increases, while the waveform corresponding to S0 mode expands as the laser-to-EMAT distance increases, which can be seem from Fig. 3-2.

3.4 Attenuation of Laser-generated Lamb Waves

LEU signals attenuate as the laser-to-EMAT distance increases. Theoretically, Lamb waves don't attenuate in perfect linear elastic materials. In reality, they attenuate but with a much slower rate than bulk waves. Therefore, they can usually interrogate larger areas than bulk waves. It is good to know how fast the Lamb wave signals acquired using our LEU system attenuate. The B-scan signals can help to estimate the attenuation rate of laser-generated Lamb waves. The sum of square is calculated for LEU signals acquired at each laser-to-EMAT distance to estimate the signal energy. Fig. 3-8 plots the signal energy versus the laser-to-EMAT distance, which is noisy due to the presence of background noises in the LEU system. A linear fitting is performed to estimate the attenuation rate of the LEU signal, as shown below.

$$E = -0.0011 \times D + 0.2685 \quad \textbf{(Eq. 3-2)}$$

where D is the laser-to-EMAT distance in mm, and E is the signal energy. It can be estimated that the signal energy reduces at a rate of 0.4% per mm and that the LEU signal will die out after the laser-generated Lamb waves propagate for a maximum of 237 mm.

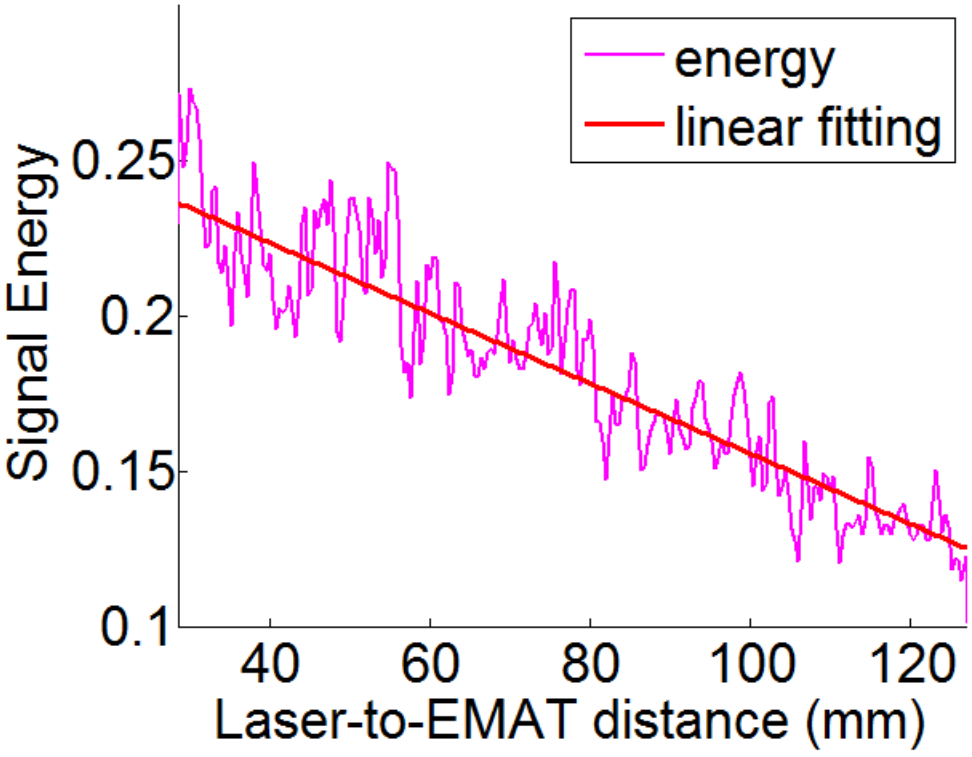

Fig. 3-8：Plot of signal energy vs. laser-to-EMAT distance

3.5 Summary

The LEU system in our lab is used to inspect a defect free 2.5 mm thick steel plate with a B-scan procedure. A wealth of information about the Lamb waves present in the LEU signals is revealed through analysis in the wavenumber-frequency domain and time-frequency domain. Due to its high resolution, the wavenumber-frequency domain representation of the B-scan signals helps to characterize properties of different laser-generated Lamb waves. Even though CWT of individual LEU signals cannot separate different Lamb waves as well as in the wavenumber-frequency domain, it stills helps to establish a better understanding of the waveform of LEU signals.

The LEU signals acquired in thin structures contain broadband and multimodal Lamb waves, which are shaped by the laser excitation and the EMAT receiver. From this preliminary study, Lamb waves which are strong in the received signals are identified, and their properties are well understood. The following studies will only focus on the interactions of the identified strong Lamb waves with welds.

CHAPTER 4

Interactions of Laser-Generated Lamb Waves with Weld Penetration Depth-Related Defect

In Chapter 3, the laser-generated Lamb waves have been characterized, and the strong Lamb waves in the received LEU signals are identified. The laser-generated Lamb waves are shown to be very complicated, which include broadband frequencies and multiple modes. Another challenge which limits applications of the LEU technique to measure WPDs in thin structures is that interactions of laser-generated Lamb waves with weld beads are also complicated. In Chapter 4, the full wave field of laser-generated Lamb waves will be measured to study their interactions with welds since wave field signals contain the complete information of Lamb waves' propagations [46-51].

The wave field signals of laser-generated Lamb waves close to a WPD-related defect will be captured using a C-Scan procedure. The measured wave field signals help to understand how the presence of the defect will affect the propagations of laser-generated Lamb waves.

4.1 Sample Preparation

Two 2.5 mm thick A36 steel plates are welded together using Gas Metal Arc Welding (GMAW). A local lack of penetration defect is created by reducing the wire feed rate (WFR). Fig. 4-1 shows the close look of the weld defect from both sides of the welded sample. The defect is 6 mm long, which is very difficult to see from the front side. The objective is to determine if the LEU system is able to detect the presence of the defect by inspecting from the front side of the sample.

(a) Front view of weld

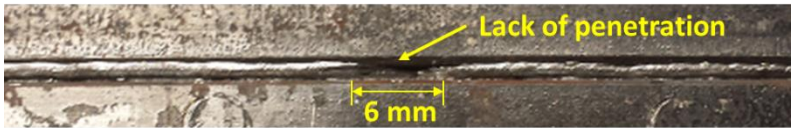

(b) Back view of weld

Fig. 4-1: Close look of defect

4.2 Inspection Setup

The inspection setup used for C-scan is shown in Fig. 4-2. The LEU inspection system in our lab consists of an Nd:YAG pulsed laser, a custom designed EMAT, a 1-directional moving sample stage, a high speed acquisition card, and a control unit. Another lead screw is added to allow the sample stage to move in two directions. The laser power is set to 115 mJ/pulse. The sampling frequency is set to 12.5 MHz. The sample is clipped firmly onto the stage, with weld seam facing up. The laser beam is delivered using a convex lens and an optic mirror and focused to a point source of 0.5 mm in radius on the sample surface. The EMAT is attached to the sample through its built-in magnet and moves with the sample. The movement of the sample stage allows the laser to be incident on multiple locations on the sample surface.

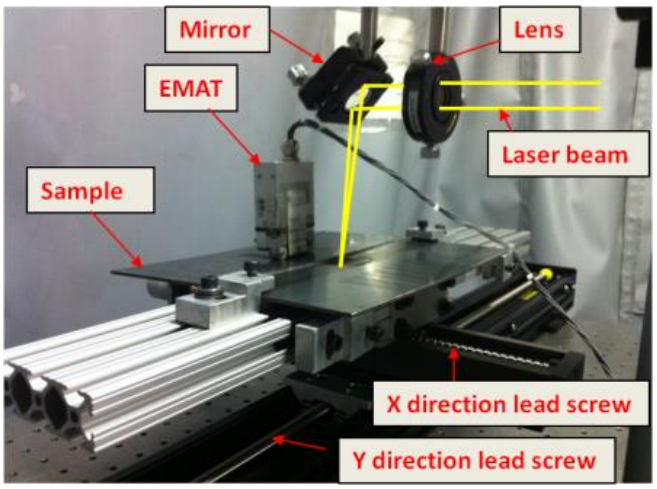

Fig. 4-2: LEU inspection system

4.3 C-scan Procedure

Fig. 4-3 (a) shows the C-scan procedure used in this work. The EMAT receiver stays stationary relative to the sample. The laser source moves relative to the sample and fires at two 30 × 80 arrays of locations on the sample surface on both sides of the weld defect. The pitch of the laser incident points is 0.3 mm in both directions. Fig. 4-3 (b) shows an alternative C-scan procedure, in which locations of the EMAT receiver and the laser source are reversed. The two C-scan procedures are equivalent with regard to the acquired signals due to reversibility of wave propagations. The first procedure is used in this work because the EMAT has a large probe area and a high spatial resolution is easier to achieve by moving the laser incident point. Plus, the first C-scan procedure can be performed with a minimum modification of the current LEU system in our lab. However, the second C-scan procedure is more intuitive to interpret the acquired signals. Since these two procedures are equivalent, the second C-scan procedure will be used to discuss the acquired signals later.

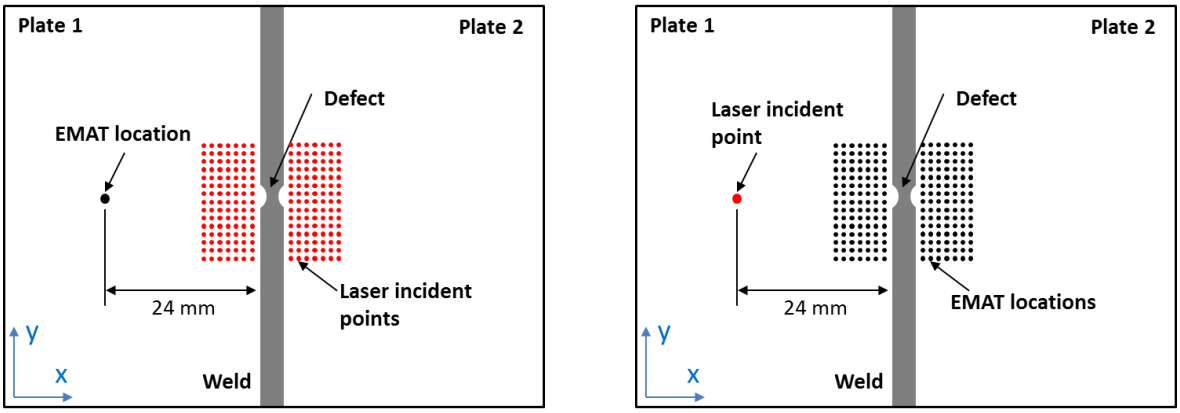

(a) C-scan procedure used

(b) Equivalent C-scan procedure

Fig. 4-3: C-scan procedures

4.3.1 Background Noise in LEU System

A challenge to perform the C-scan procedure is that a very strong background noise is observed in the LEU inspection system. Fig. 4-4 shows a raw LEU signal, which is heavily contaminated by the background noise and therefore has a very low SNR.

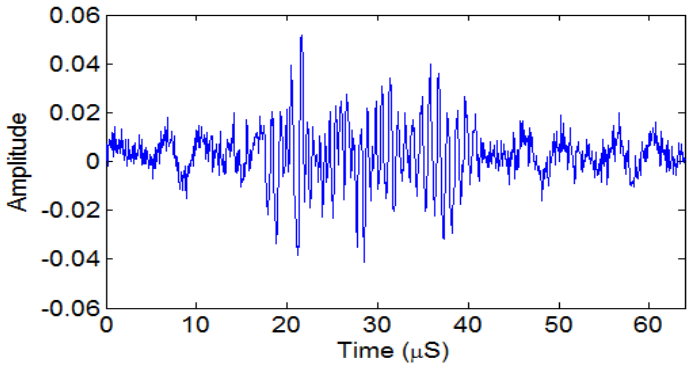

Fig. 4-4: Plot of a raw LEU signal

Fig. 4-5 shows the plot of a pure background noise, which is captured by blocking the laser pulse from reaching the sample surface during inspection. The signal has a low-frequency ripple with superimposed high-frequency random oscillations. The background noise is believed to originate from the preamp circuit of the EMAT receiver.

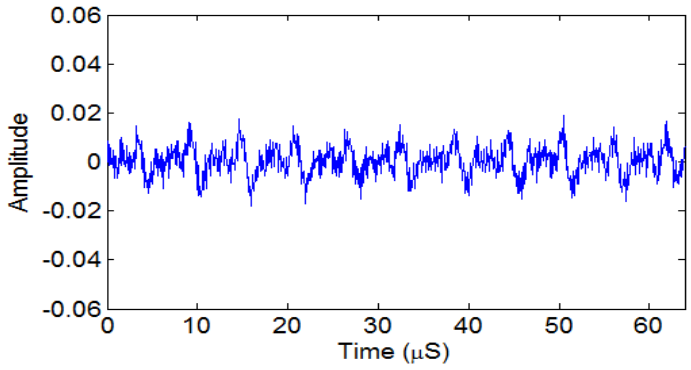

Fig. 4-5: Plot of a pure background noise

Usually the laser fires multiple times at the same location, and the acquired signals are averaged to improve the SNR. Fig. 4-6 shows the signal obtained by averaging 16 raw LEU signals acquired at the same location as the signal in Fig. 4-4. The background noise is greatly diminished, and the SNR is improved, however, at a cost of compromising the inspection speed. The averaging-based method to improve SNR is not suitable for the C-scan procedure, since there are totally 4800 locations to inspect.

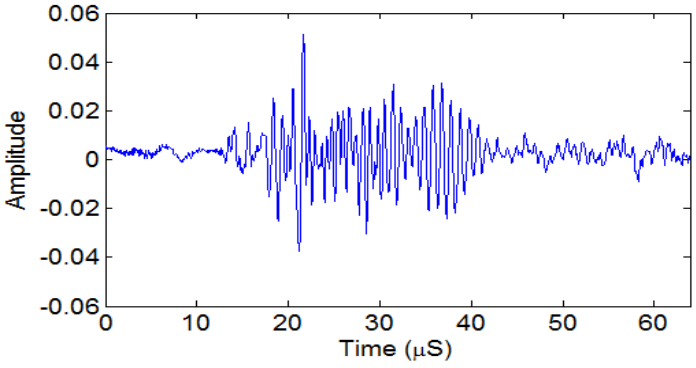

Fig. 4-6: Plot of average signal from 16 raw LEU signals

4.3.2 CWT-based Denoising

Instead, a CWT-based method will be used to improve the SNR, which allows the laser to fire only once at each location. Fig. 4-7 shows the CWT of the raw LEU signal in Fig. 4-4 using Morlet

as the mother wavelet. In the time-frequency domain, the low-frequency ripple in the background noise is located below 0.5 MHz, and the high-frequency random oscillations in the background noise are scattered all around. Lamb waves in the signal correspond to CWT coefficients of high magnitudes within the EMAT bandwidth.

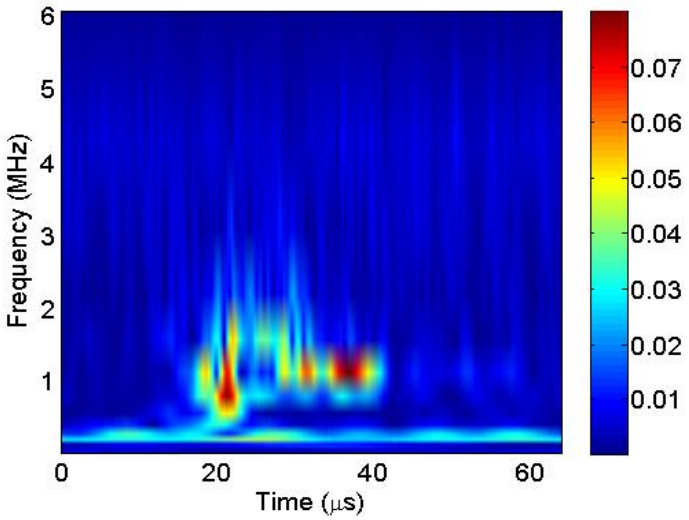

Fig. 4-7: CWT plot of raw signal

The background noise can be removed from the time-frequency domain in two steps. First, CWT coefficients beyond the EMAT bandwidth are replaced by zeros. Secondly, within the EMAT bandwidth any CWT coefficient smaller than a pre-determined threshold is replaced by zero. The modified CWT coefficients are then inverse transformed to reconstruct the signal in the time domain.

A proper threshold needs to be determined. If the threshold is too small, some of the background noise within the EMAT bandwidth remains in the reconstructed signal. If the threshold value is too large, some of the small CWT coefficients corresponding to Lamb waves will be compromised. Fig. 4-8 shows how the selected threshold will affect the energy of the

reconstructed signal. The signal energy decreases first because the background noise becomes less and then because the Lamb waves are compromised.

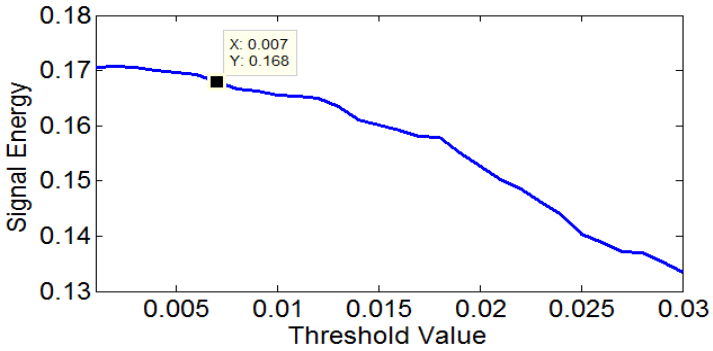

Fig. 4-8: Signal energy vs. threshold

Fig. 4-9 shows how increasing the number of averaging will affect the energy of the averaged signal. The signal energy decreases and approaches a constant value as more signals are averaged. Assuming the background noise can be completely removed when the averaging number reaches infinite, the constant value corresponds to the energy of the noise-free signal. The threshold is selected to yield a signal energy equal to the constant value. The threshold is selected to be 0.007, as shown in Fig. 4-8.

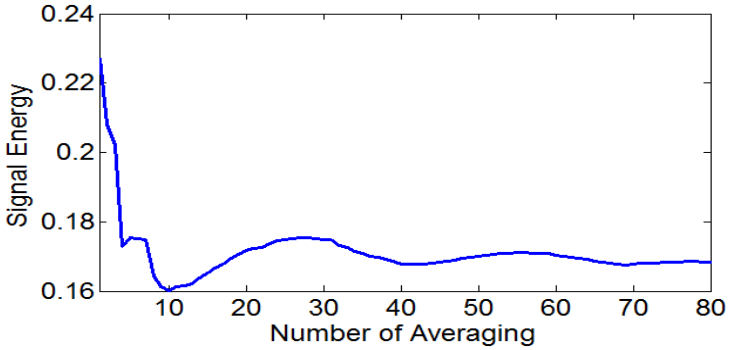

Fig. 4-9: Signal Energy vs. Number of Averaging

Fig. 4-10 shows the modified CWT coefficients using the selected threshold, and Fig. 4-11 shows the reconstructed signal. Comparison with Fig. 4-6 shows that the CWT-based method can achieve a SNR comparable to the averaging-based method but without sacrificing the inspection speed.

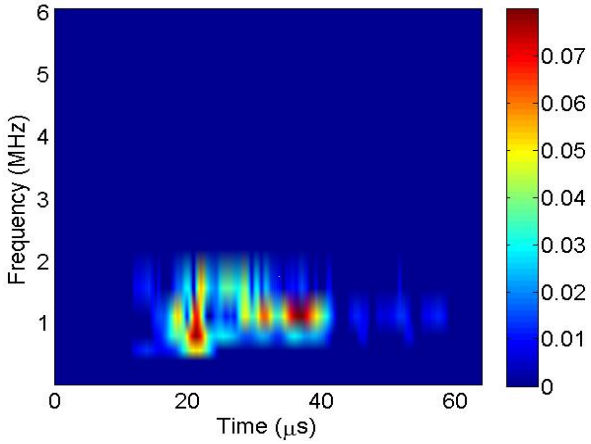

Fig. 4-10: Modified CWT coefficients

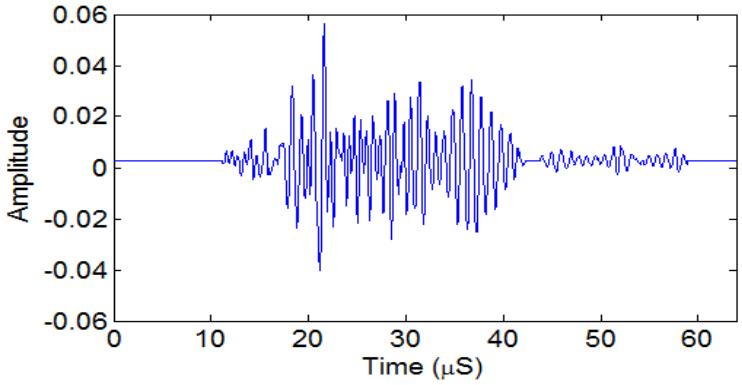

Fig. 4-11: Plot of CWT-denoised signal

4.4 Wave Field Signal Analysis

The C-scan procedure collects signals from 4800 locations, which are denoised using the CWT-based method. The 4800 signals are assembled into two 3-D data matrices based on their

acquisition locations. The two 3-D data matrices have the same size. The first data matrix consists of signals acquired from the left side of weld, and the second data matrix consists of signals acquired from the right side of weld. Fig. 4-12 shows the diagram of one 3-D data matrix. The first two dimensions of the 3-D data matrix correspond to the coordinates of the acquisition locations, and the third dimension corresponds to time. The C-scan procedure in Fig. 4-3 (b) is used here to interpret the 3-D data matrix. Data on each “slice” normal to the time dimension represent the wave signal over the inspected area at the corresponding moment. Plotting the "slices" in time order allows the wave field in the inspected area to be visualized [50].

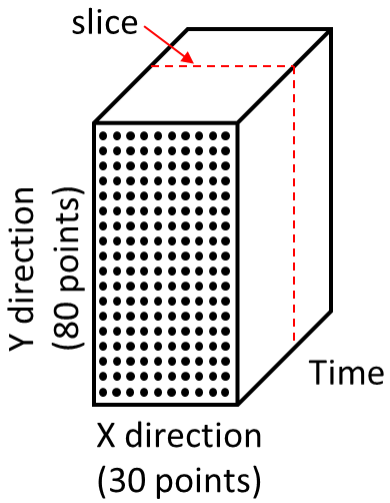

Fig. 4-12: 3-D data matrix

Fig. 4-13 shows snapshots of the wave fields in the two inspected areas at 6 evenly separated moments. The laser-generated Lamb waves propagate towards right in the left wave field. When their wave fronts encounter the weld, some of them get reflected and the rest transmit through the weld to the right wave field. The left wave field contains the incident and reflected waves, and the right wave field contains the transmitted waves.

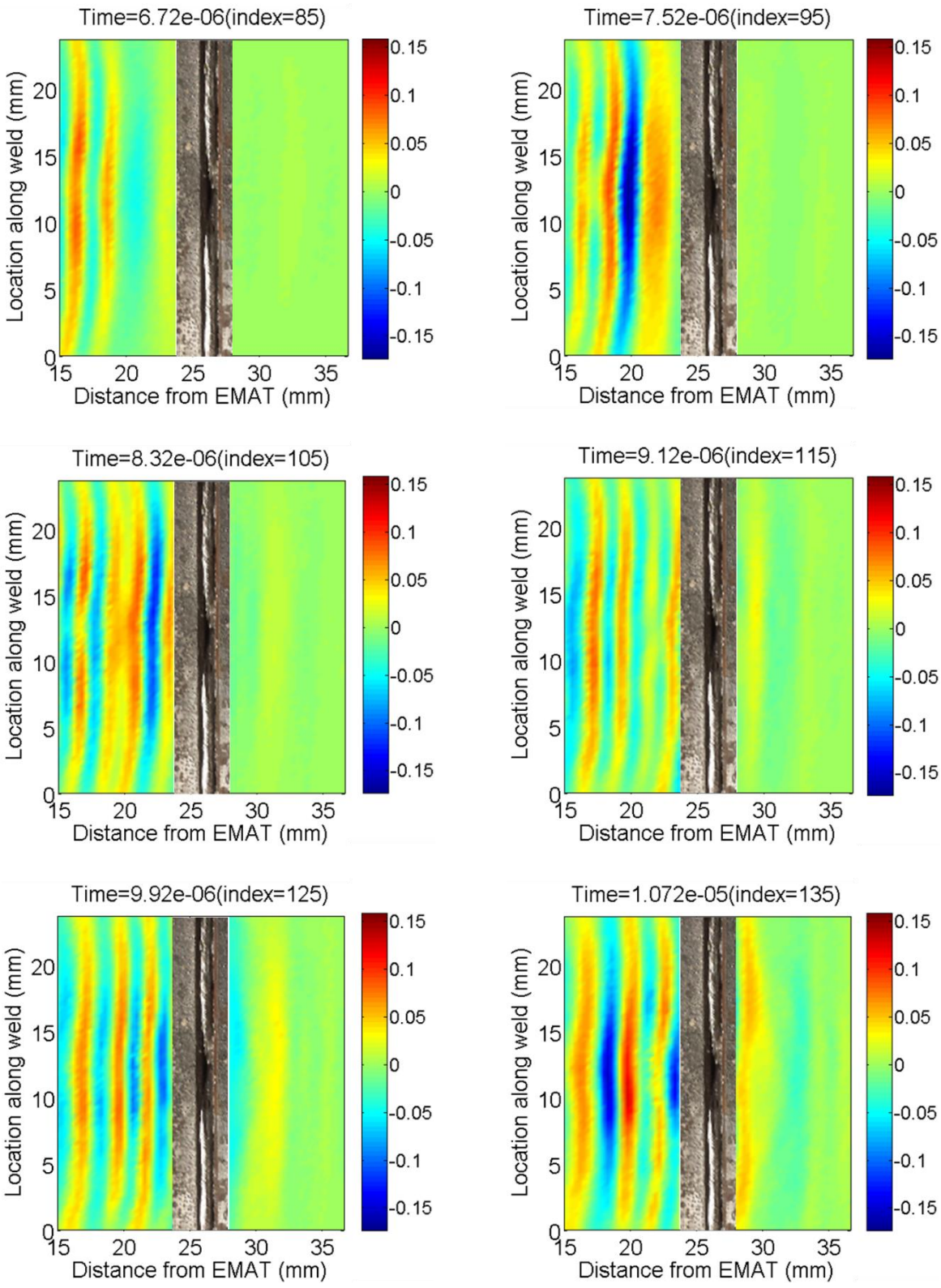

Fig. 4-13: Snapshots of original wave fields

In the left wave field, because of the different speeds of laser-generated Lamb waves, the fast Lamb waves get reflected sooner, and their reflections interfere with the slow Lamb waves. The reflected waves are of more interest because they contain the information of the weld defect. However, they are obscured by the strong incident waves. It would be helpful to remove the incident waves and highlight the reflections in the left wave field.

In the right wave field, the signals are cleaner because it primarily contains the right-going transmitted waves. However, at the very end of the wave field signals, reflections from the sample edge are observed. It would be helpful to remove the edge reflections in the right wave field.

4.4.1 Remove Incident Waves and Edge Reflections Using 3-D FT

The collected wave field signals essentially are two dimensional waves propagating in a plane. 3-D FT can be used to remove the incident waves in the left wave field and the edge reflections in the right wave field [52]. In the left wave field, because the incident and the reflected waves propagate in opposite directions, they are automatically separated in the k_x - k_y - ω domain when 3-D FT is applied to the 3-D data matrix of the left wave field. According to Table 2-2, the left-going reflections correspond to 3-D FT coefficients in Octants II, III, V and VIII, and the right-going incident waves correspond to 3-D FT coefficients in Octants I, IV, VI and VII. The 3-D FT coefficients corresponding to the incident waves are replaced by zeros. Fig. 4-14 (a) shows the remaining 3-D FT coefficients in the k_x - k_y - ω domain. The remaining 3-D FT coefficients are inverse transformed to reconstruct the wave field signals in the time and spatial domain. In the right wave field, the transmissions and the edge reflections propagate in opposite directions.

Therefore, the same method is used to remove the edge reflections. Fig. 4-14 (b) shows the remaining 3-D FT coefficients in the k_x - k_y - ω domain for the right wave field.

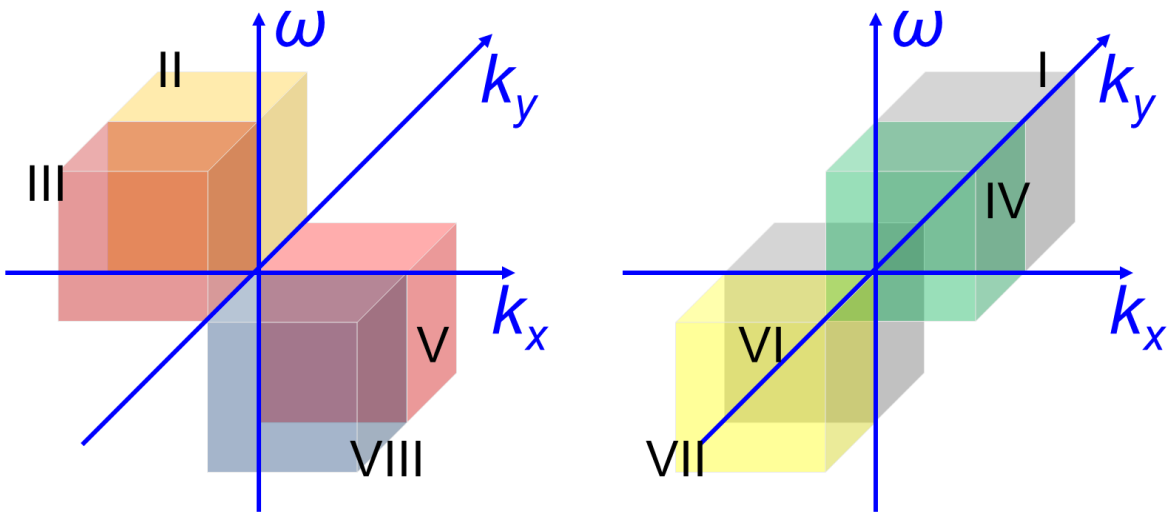

(a) Left wave field (b) Right wave field

Fig. 4-14: 3-D FFT coefficients selected for extracting reflections and transmissions

Snapshots of the two wave fields after the incident waves and edge reflections are removed are shown in Fig. 4-15. Only the left-going reflections are observed in the left wave field, and only the right-going transmissions are observed in the right wave field. The presence of the weld defect is clearly indicated by the reflected wave fronts and the disconnections in the transmitted wave fronts. The lack of penetration defect in the weld causes stronger reflections and weaker transmissions. Because the laser-generated Lamb waves contain multiple modes, their reflections and transmissions are overlapping with each other. It would be helpful to separate reflections and transmissions of different Lamb wave modes so that their interactions with the weld defect can be viewed separately and Lamb wave modes sensitive to the defect can be identified.

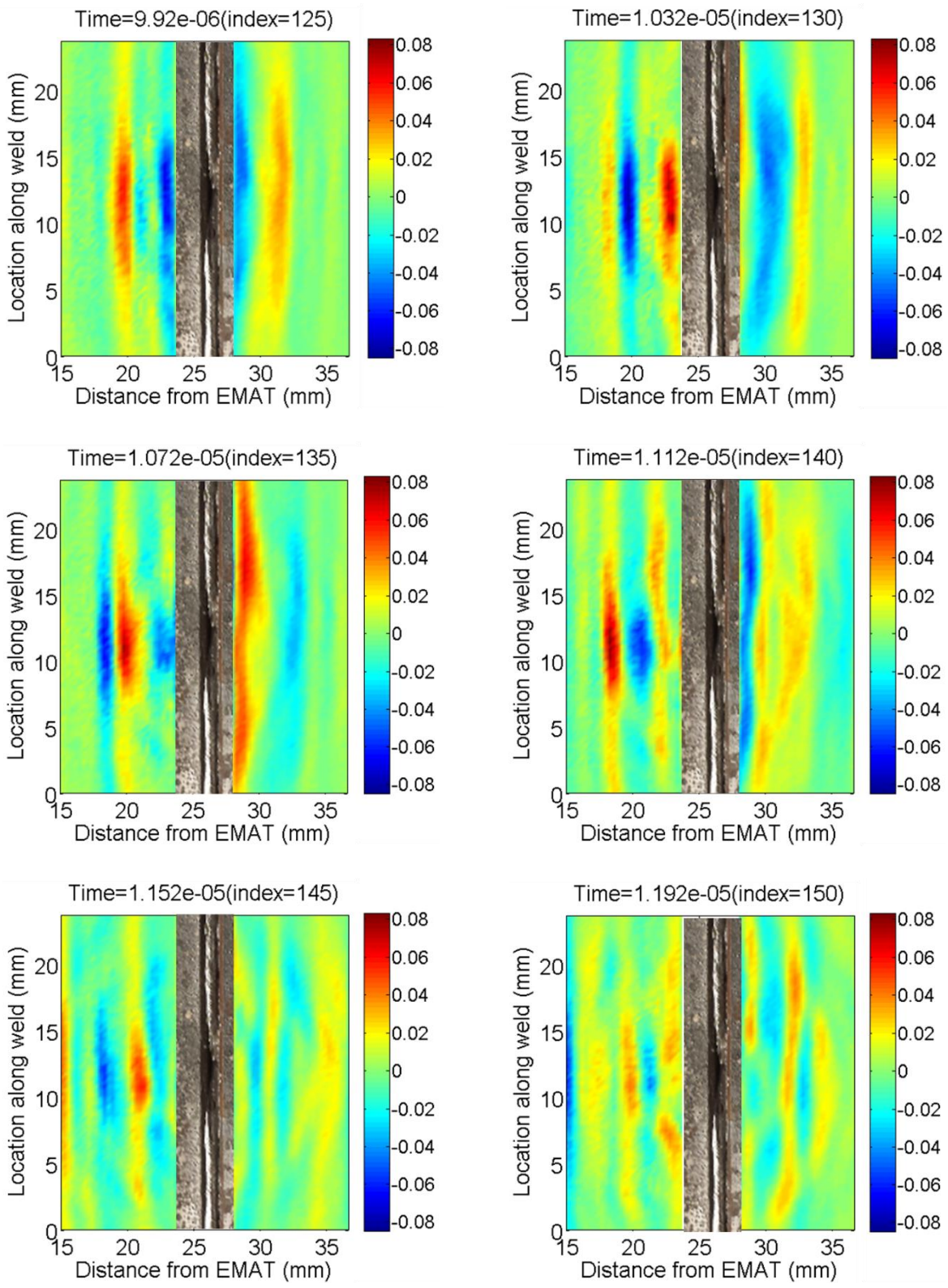

Fig. 4-15: Snapshots of wave fields after incident waves and edge reflections are removed

4.4.2 Separate Different Lamb Wave Modes

Dispersive curves of Lamb waves in the wavenumber-frequency domain extend to dispersive surfaces in the k_x - k_y - ω domain. Fig. 4-16 shows the dispersive surfaces of several modes in the k_x - k_y - ω domain. The dispersive surfaces are cone-shaped surfaces which are obtained by rotating the dispersive curves in the k - ω domain around the ω axis. After 3-D FT converts the reflection and transmission field signals to the k_x - k_y - ω domain, different Lamb wave modes fall on these surfaces and are separated automatically. Different Lamb wave modes contained in the reflection and transmission fields can be separated by extracting 3-D FT coefficients corresponding to different Lamb waves modes in the k_x - k_y - ω domain.

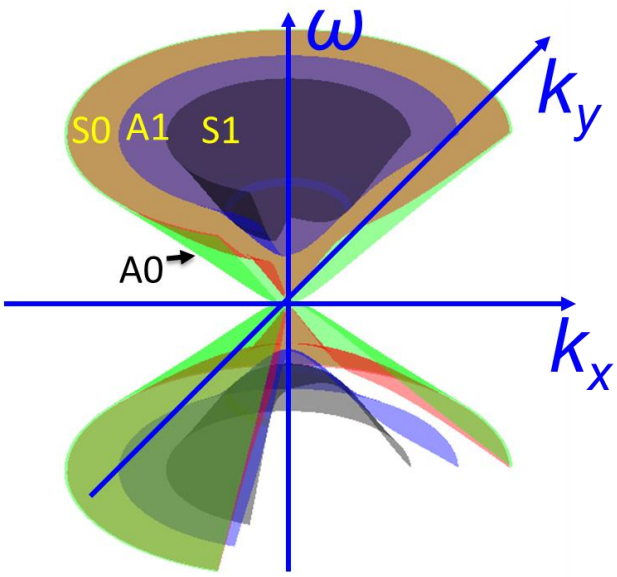

Fig. 4-16: Dispersive surfaces in k_x - k_y- ω domain

The reflection field signals will be used to demonstrate how to separate different Lamb wave modes. Their 3-D FT coefficients, as shown in Fig. 4-14 (a), can be divided into slices perpendicular to the ω axis. Each slice intersects with the dispersive surfaces at circular curves of different

radius. Fig. 4-17 shows a slice of 3-D FT coefficients in Octant V corresponding to -0.98877 MHz, whose intersections with dispersive surfaces are plotted, too. Because the absolute value of the frequency is below the cut-off frequency of S1 mode, only three circular curves are plotted, which correspond to A0, S0, and A1 modes. The circular curves help to identify the 3-D FT coefficients corresponding to different Lamb wave modes. High 3-D FT coefficients in the slice are located close to the k_x axis. This is because the decomposition of the wave propagation direction in the measured wave field has a large x component, which can be seen from Fig. 4-15.

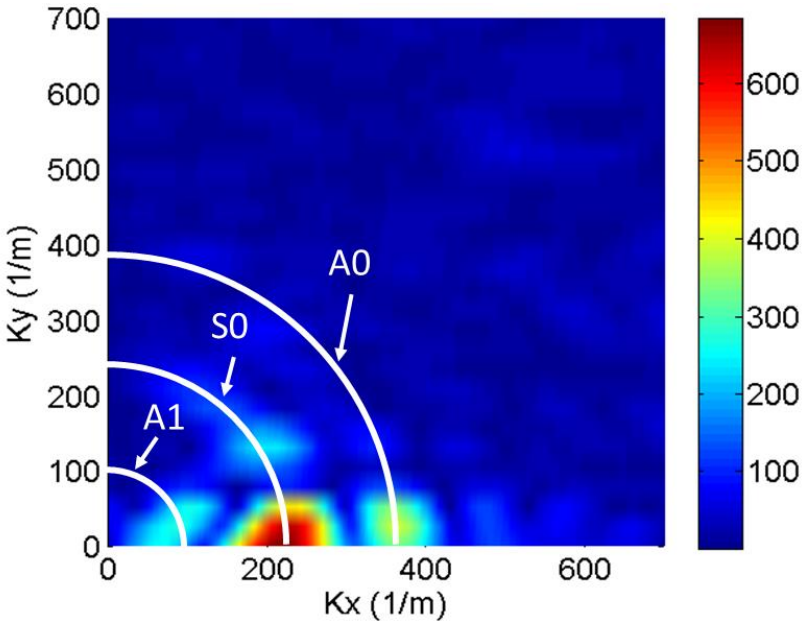

Fig. 4-17: 3-D FT coefficients on a slice corresponding to -0.98877 MHz

The 3-D FT coefficients corresponding to different Lamb wave modes are extracted from each slice with the help of the intersection curves. The extracted 3-D FT coefficients are inverse transformed to reconstruct the reflections of different Lamb wave modes. The same method can be used to separate different Lamb wave modes in the transmission field. Snapshots of reflections and transmissions of A0, S0, and A1 modes, which are the strongest Lamb wave modes

identified in LEU signals, are shown in Fig. 4-18, Fig. 4-19 and Fig. 4-20, respectively. Because each Lamb wave mode contains broadband frequencies, their interactions with the weld defect are still very complicated.

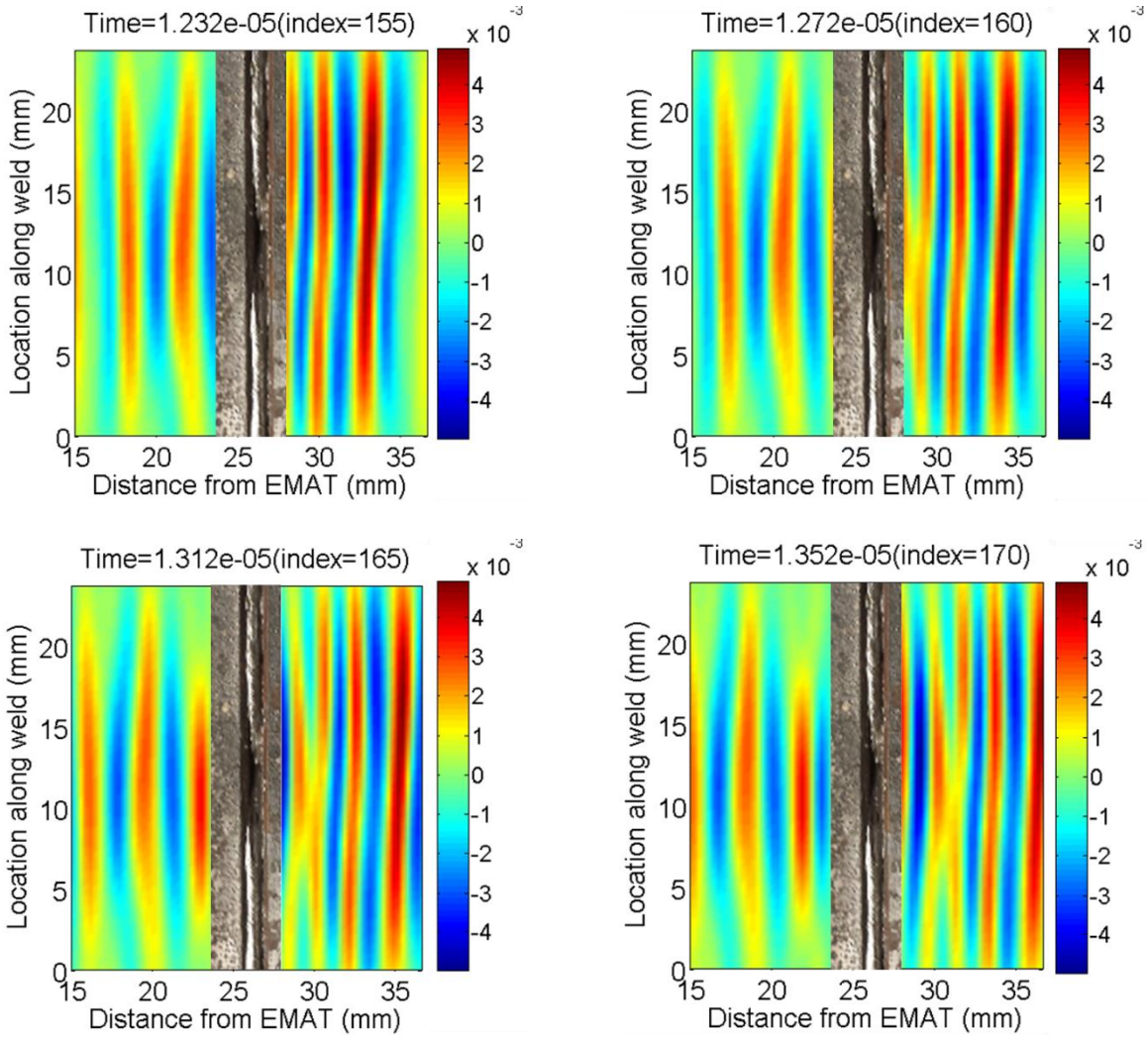

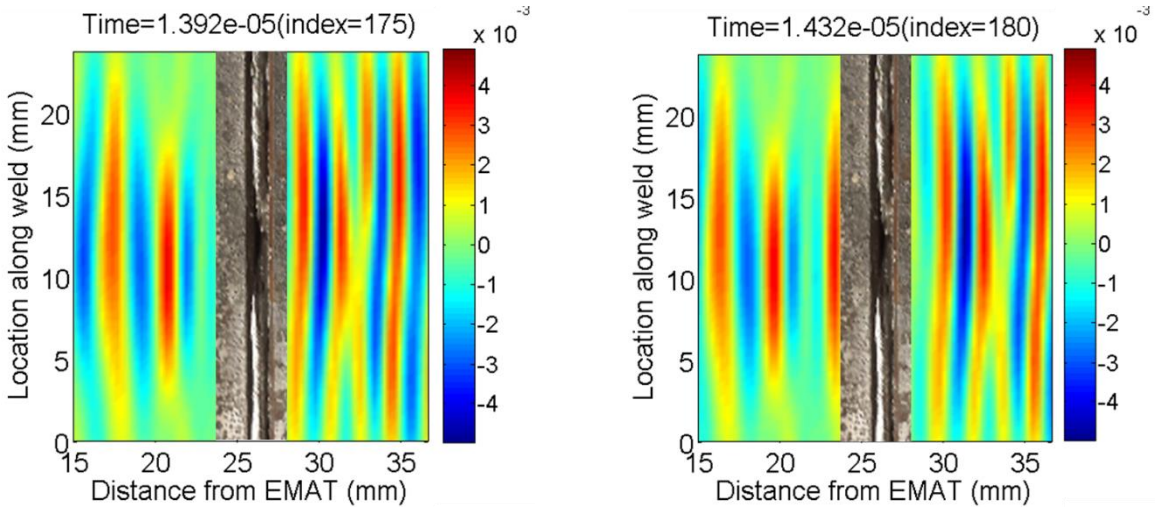

Fig. 4-18: Reflection and Transmission of A0 mode

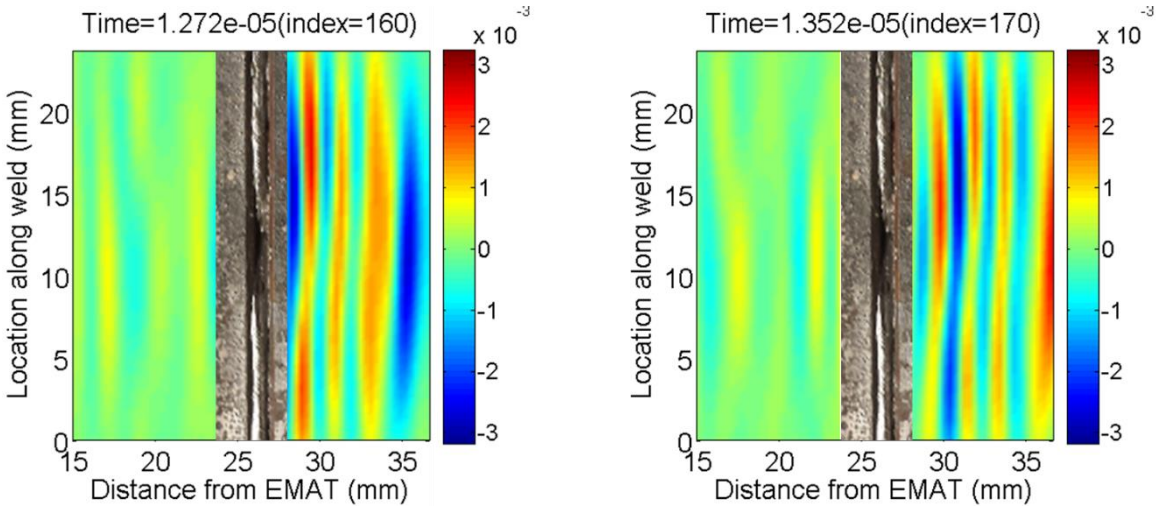

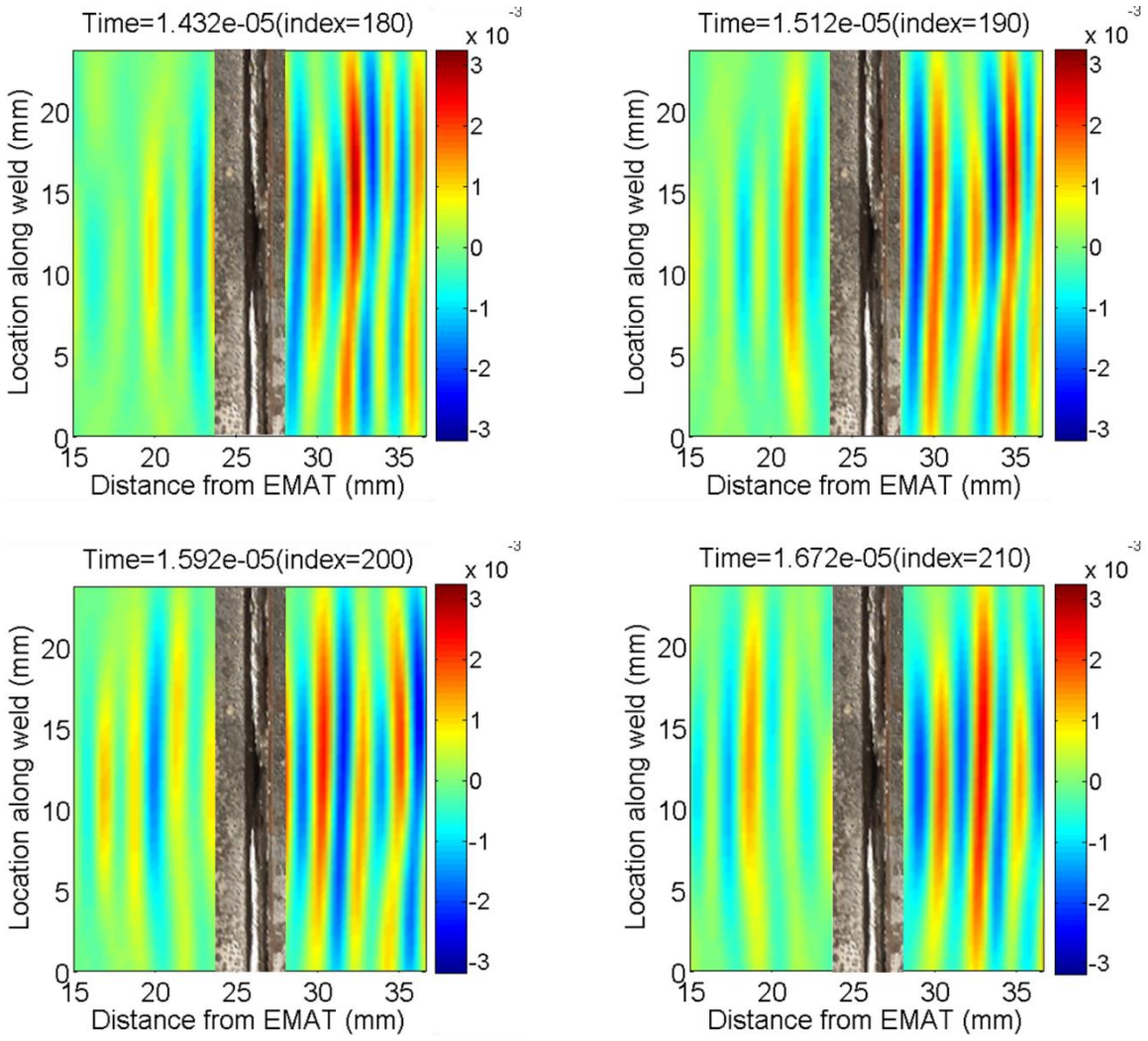

Fig. 4-19: Reflection and Transmission of S0 mode

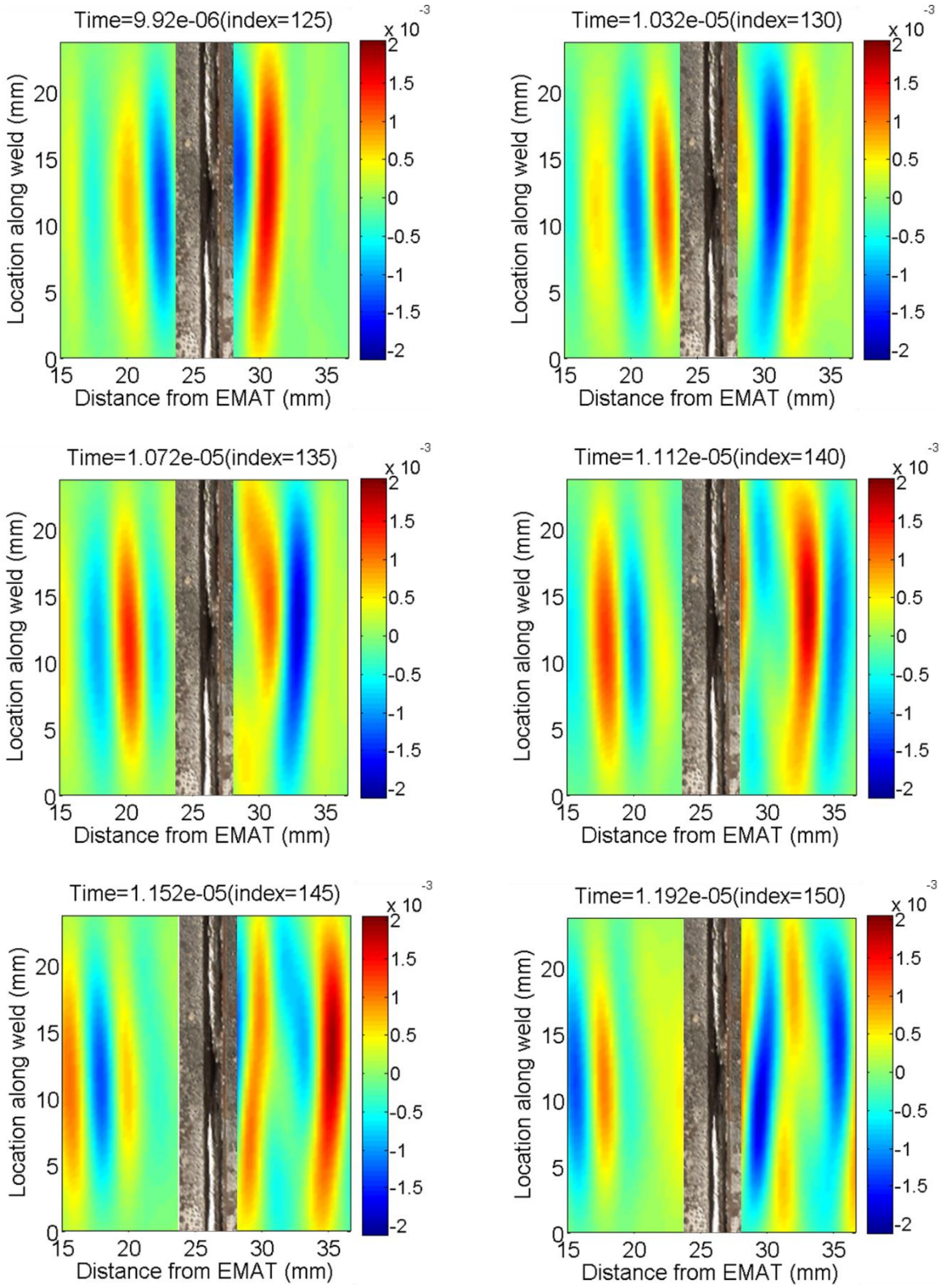

Fig. 4-20: Reflection and Transmission of A1 mode

4.4.3 Separate Different Frequencies of Each Lamb Wave Mode

Different frequencies of each Lamb wave mode can be further separated by extracting their corresponding 3-D FT coefficients and inverse 3-D FT. Observing their reflection and transmission fields helps to understand how the defect will affect the Lamb wave's propagation. Not all frequencies of each Lamb wave mode are sensitive to the presence of the weld defect. Wave fields of two sensitive Lamb waves, A0 mode at 1.5 MHz and S0 mode at 1.1 MHz, are plotted in Fig. 4-21 and Fig. 4-22, respectively. They have different interactions with the weld defect. For the A0 mode Lamb wave of 1.5 MHz, the weld defect causes strong reflections and creates disconnections in the transmitted wave fronts. For the S0 mode Lamb wave of 1.1 MHz, the weld defect creates strong wave fronts in the transmitted field, which may be caused by mode conversions occurring at the defect. These two Lamb waves show the capability to detect the presence of the lack of penetration defect either with their reflection or transmission field.

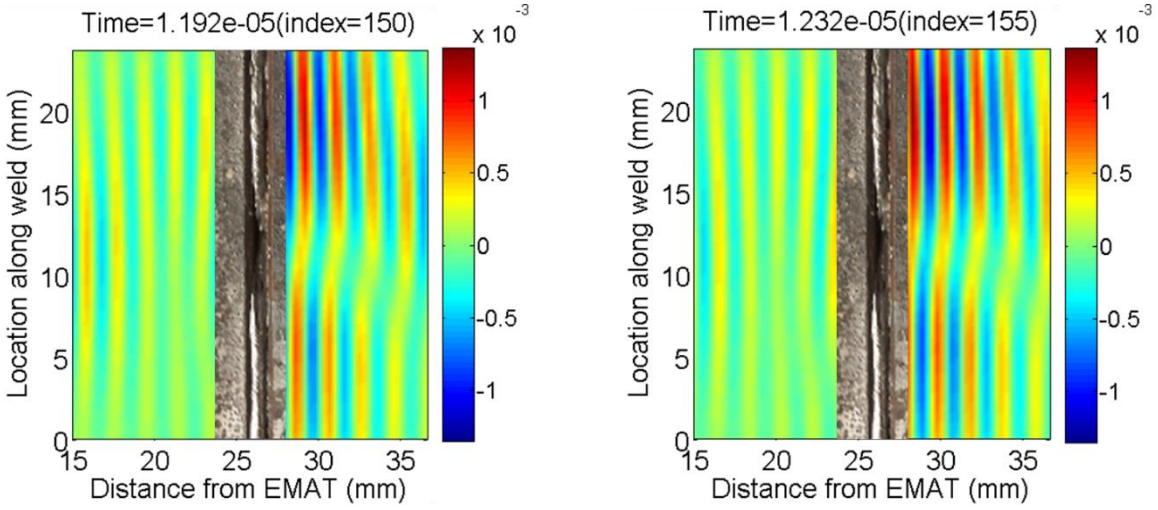

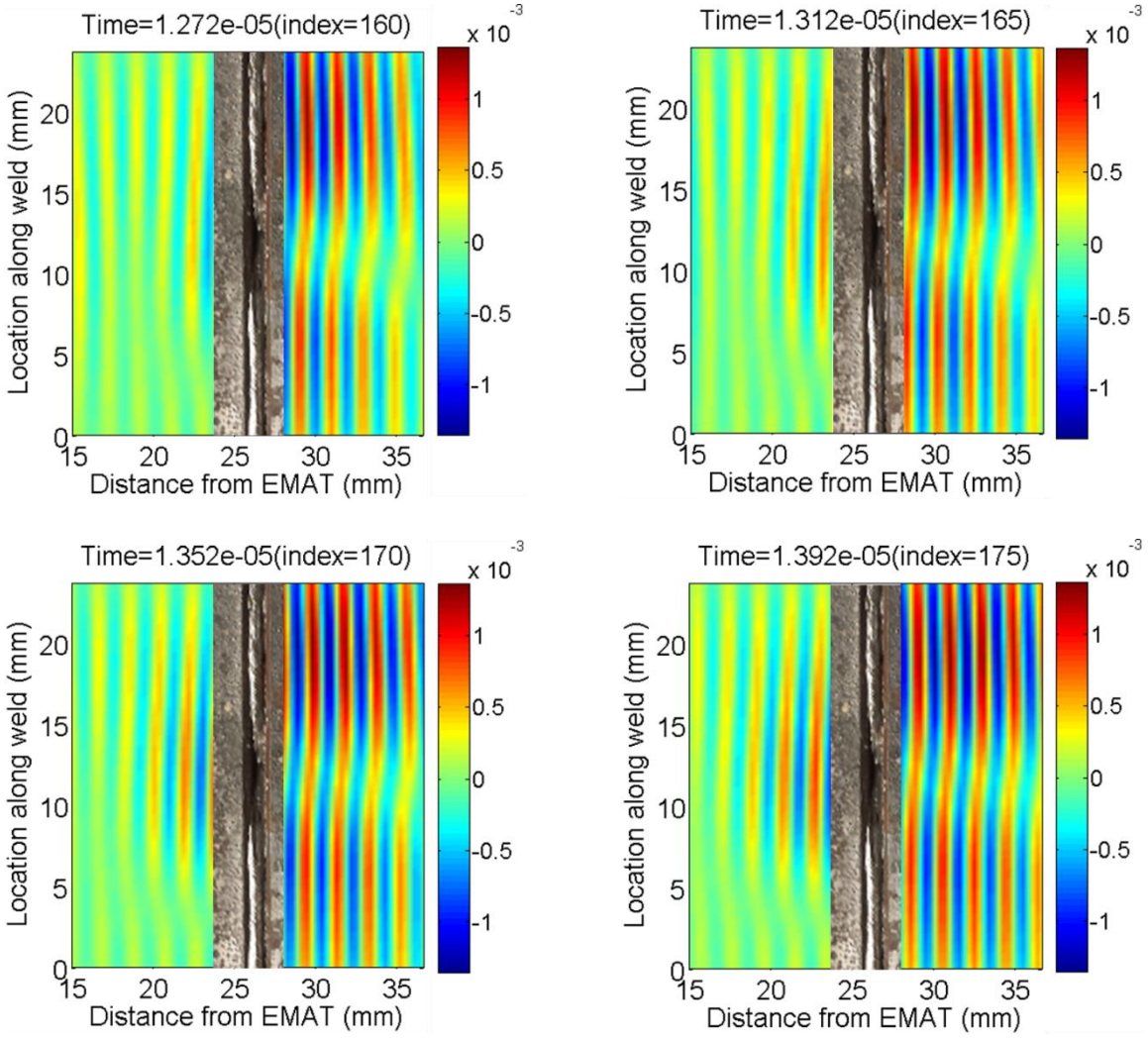

Fig. 4-21: Reflection and Transmission of A0 mode at 1.5 MHz

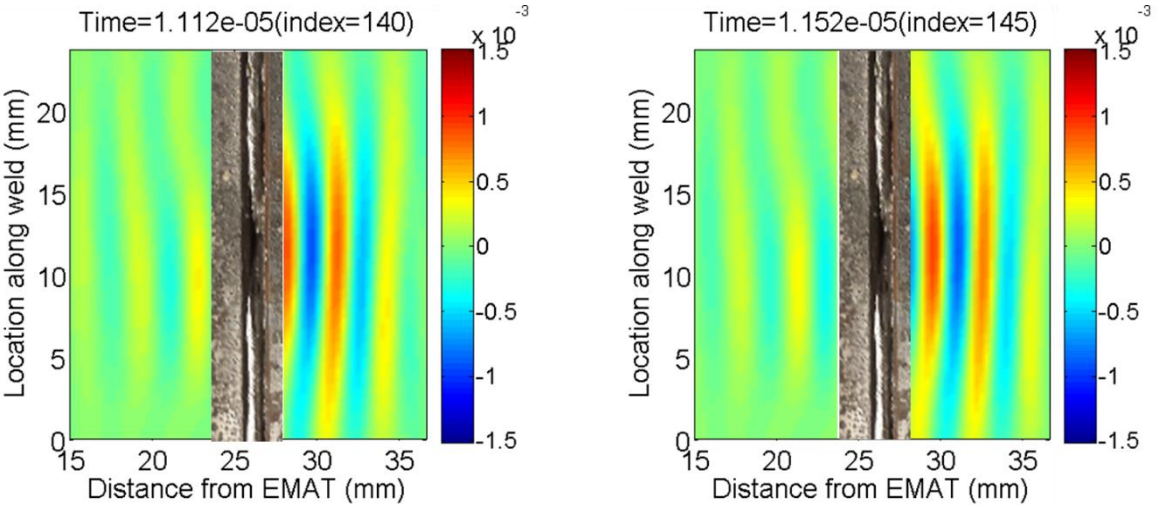

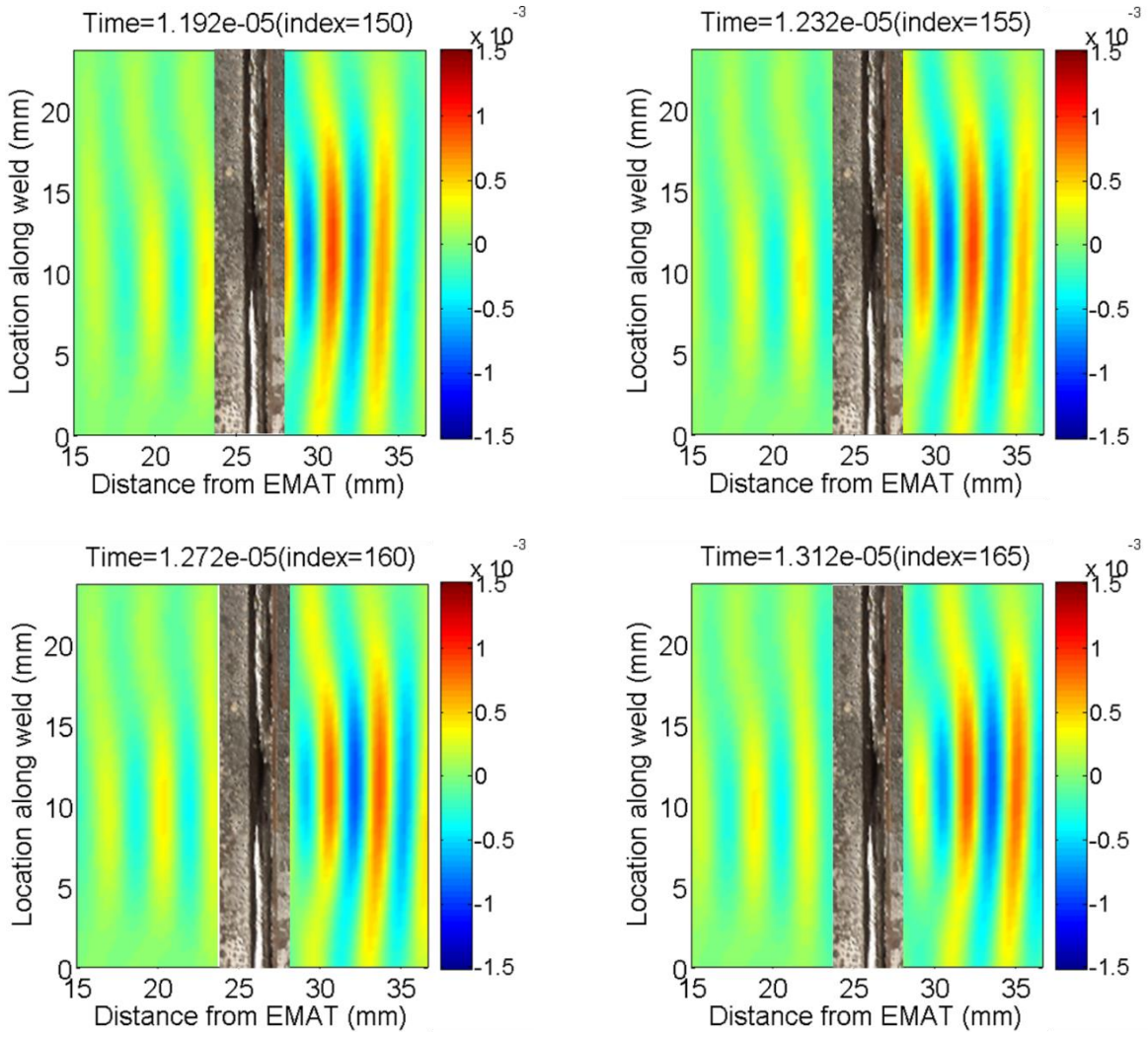

Fig. 4-22: Reflection and Transmission of S0 mode at 1.1 MHz

4.5 Summary

The wave field signals of laser-generated Lamb waves close to a WPD-related defect are captured using a C-scan procedure. A CWT-based method is used to improve the SNR of LEU raw signals, which greatly reduces the experimental time. 3-D FT-based filtering is used to remove the useless incident waves and edge reflections in the wave field signals. The interactions of laser-generated Lamb waves with the weld defect are complicated because they contain multiple modes and broadband frequencies. Dispersive surfaces in the k_x - k_y- ω domain help to separate

wave field signals corresponding to different Lamb waves. Not all Lamb waves in LEU signals are sensitive to the presence of the defect. Different Lamb waves may have different interactions with the defect. Sensitive Lamb waves in the LEU signals can be used to detect the presence of the lack of penetration defect based on their reflections or transmissions.

CHAPTER 5

Measurement of Varying Notch Depths Using Transmission Coefficient of Laser-Generated Lamb Waves

In Chapter 4, interactions of Lamb waves present in LEU signals with a local lack of penetration defect are investigated, and the LEU technique shows the potential to detect varying WPDs in thin structures qualitatively based on reflections or transmissions of sensitive Lamb waves. This chapter will move one step further to investigate if the LEU technique is able to measure WPDs in thin structures quantitatively using transmission coefficients of laser-generated Lamb waves. Transmission coefficients of Lamb waves are selected because it's easier to calculate transmission coefficients than reflection coefficients.

This chapter will first use varying notch depths to evaluate the capability of transmission coefficients of laser-generated Lamb waves for two reasons. First, notches of varying depths are easier to manufacture due to its structural simplicity. Secondly, notches of varying depths can roughly simulate welds of varying penetration depths, as shown in Fig. 5-1. Assuming that the weld face and root are flat and that the weld bead and the base material have the same material properties, a butt joint weld can be approximated by an isolated surface notch. In this approximation, the plate thickness minus the notch depth is equivalent to the simulated WPD. Investigation of the capability of the LEU signals to measure varying notch depths can help to determine whether they can be used to measure varying WPDs.

Notch is a very important structural feature in NDT, which has been extensively studied with respect to its interactions with Lamb waves [53-55]. However, previous studies mainly focused on its interactions with narrowband fundamental Lamb wave modes generated using traditional ultrasonic transducers [56, 57].

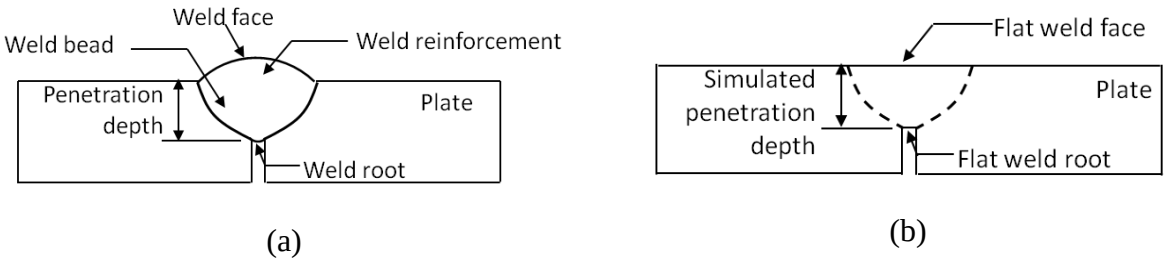

Fig. 5-1: Simulated weld penetration depth: (a) butt joint weld, (b) isolated notch

In this chapter, finite element analysis (FEA) and experimental measurement are used to study how Lamb waves transmit across varying notch depths. Only the strong Lamb waves identified in LEU signals will be investigated.

5.1 Finite Element Study

Finite element analysis is first used to investigate how varying notch depths in a thin plate will affect transmission coefficients of laser-generated Lamb waves. Simulating the laser excitation of Lamb waves is complicated and time-consuming, and therefore not suitable for the parametric study of varying notch depths. Instead, a simple and efficient FEA model is developed to quickly simulate how individual Lamb waves propagate in thin plates and how they transmit across varying notch depths. For the different Lamb waves identified in the LEU signals, their interactions with the varying notch depths will be simulated separately.

5.1.1 Finite element model

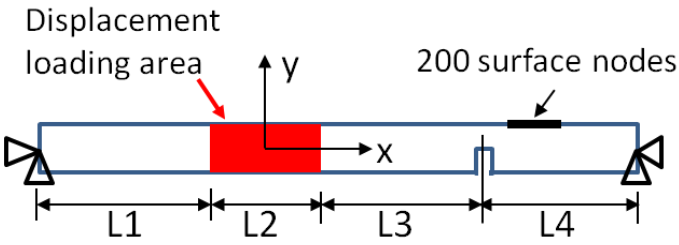

Fig. 5-2: Finite Element Model

Figure 5-2 shows the 2-D FEA model used in this work, which is a plane strain analysis using the PLANE182 element in ANSYS. The model simulates a 2.5 mm thick steel plate with a notch on its bottom surface. The two ends of the plate are completely constrained. In each run, an individual Lamb wave is excited in the plate by applying a proper loading condition to the red zone. The loading condition is divided into two steps. In load step 1, the theoretical displacement field of the Lamb wave which is to be excited is applied to the red zone as a displacement loading. In load step 2, the displacement loading is removed to allow the excited Lamb wave to propagate freely in the plate. Changing the notch depth makes it possible to study the effect of the varying notch depths on the transmission of the excited Lamb wave. Changing the displacement loading makes it possible to study a different Lamb wave's interaction with the varying notch depths.

In practice, the applied theoretical displacement fields of Lamb waves are shaped to avoid abrupt changes of the loading condition at the boundaries of loading area and at the transition between the two load steps. Two Hanning windows, as defined in Eq. 5-1 and Eq. 5-2, are used to shape the displacement loading in the time domain and the space domain, respectively.

$$W_{time} = 0.5 \times (1 - cos\frac{2\pi t}{D}) \quad \textbf{(Eq. 5-1)}$$

$$W_{space} = 0.5 \times (1 + cos\frac{2\pi x}{L2}) \quad \textbf{(Eq. 5-2)}$$

where D is the duration of load step 1, and $L2$ is the length of the displacement loading area, as shown in Fig. 5-2. Fig. 5-3 shows the plots of the two window functions used when the S0 mode Lamb wave at 0.9771 MHz is to be simulated.

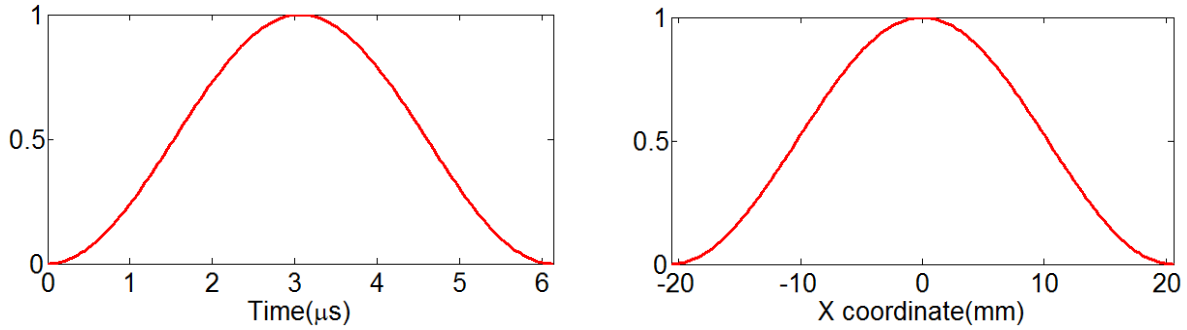

(a) Time domain window function (b) Space domain window function

Fig. 5-3: Plots of window functions used when simulating S0 mode at 0.9771 MHz

In the FEA model, the notch width is fixed to be 1 mm. Other parameters such as the labeled lengths, element size, and step size, are set to be functions of the excited Lamb wave's period (T) or wavelength (λ), as listed in Table 5-1. This parametric design has two advantages. First, the FEA model can be easily modified to simulate different Lamb waves. Secondly, the number of total elements in the model is controllable when Lamb waves of small wavelength are simulated. The duration of load step 2 and the plate length are properly selected to avoid reflections from the ends of the plate. The material properties in Table 3-1 are used so that the simulation results can be experimentally verified later.

Table 5-1: Dependent parameters of FEA model

Parameters	Value	Parameters	Value	Parameters	Value
L1	25 λ	L4	20 λ	Load Step 1	6 T
L2	10 λ	Element size (x)	1/20 λ	Load Step 2	120 T
L3	25 λ	Element size (y)	1/20 λ	Sub-step	1/20 T

5.1.2 Validation of Finite Element Model

The finite element model will be validated first to make sure that it excites only the expected Lamb wave in the plate. When the notch depth equals zero, the model becomes a notch-free plate. The excited waves in the model can be characterized using "B-scan" signals acquired from a series of equally-spaced surface nodes.

The excitation of the S0 mode Lamb wave at 0.9771 MHz is used to validate the FEA model. Its theoretical displacement field is applied as the displacement loading, and the notch depth is set to zero. After the model is solved, transient in-plane displacements of 200 adjacent nodes on the plate surface, as shown in Fig. 5-2, are extracted to obtain the "B-scan" signals. Fig. 5-4 shows the compilation of the "B-scan" signals based on the x coordinates of the surface nodes. Fig. 5-5 shows one of the 200 signals in the time domain and its frequency spectrum. The excited wave has a peak frequency at 0.9771 MHz. 2-D FT converts the "B-scan" signals to the wavenumber-frequency domain, as shown in Fig. 5-6. The theoretical dispersive curve of the S0 mode is superimposed to the 2-D FT plot, and the excited wave falls on the dispersive curve, which confirms that the FEA model only excites the expected Lamb wave in the plate.

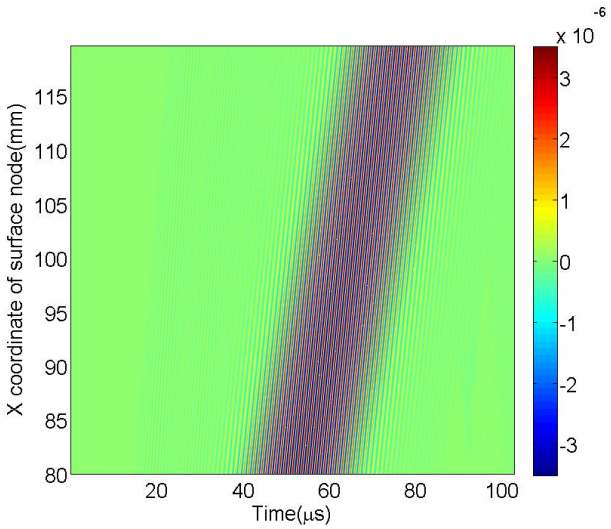

Fig. 5-4: Compilation of 200 surface node signals in time-space domain

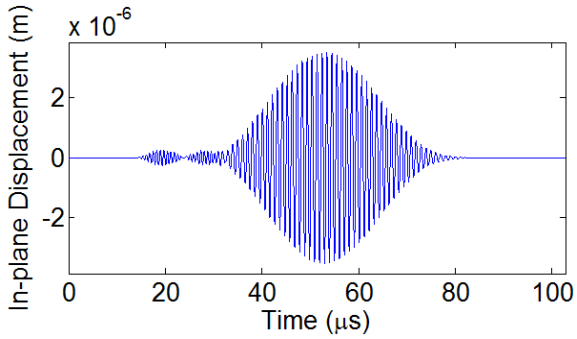

(a) Time domain representation

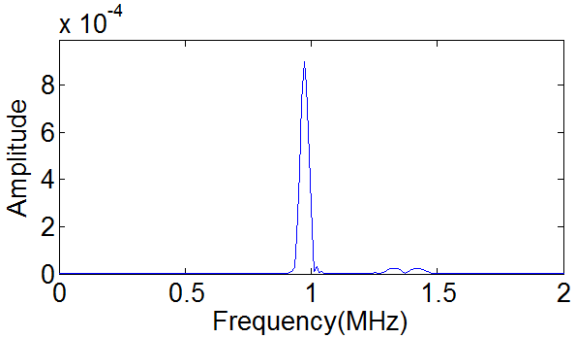

(b) Frequency spectrum

Fig. 5-5: Time domain representation and frequency spectrum of in-plane displacement of one surface node

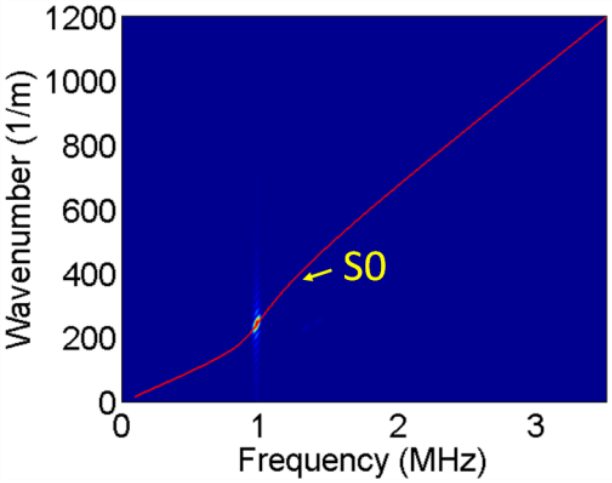

Fig. 5-6: 2-D FT of surface node signals when notch depth equals 0 mm

The in-plane and out-of-plane displacements of nodes along the thickness direction of the plate are also extracted to study the mode shapes of the excited Lamb wave in the FEA model. The maximum displacement amplitudes are normalized and plotted in Fig. 5-7. The theoretical mode shapes of S0 mode Lamb wave at 0.9771 MHz are also plotted in Fig. 5-7. The simulated and theoretical mode shapes match very well, which further confirms that the FEA model excites a clean Lamb wave in the plate. The excited Lamb wave in the FEA model is very simple, which makes it easy to study how it interacts with the varying notch depths later.

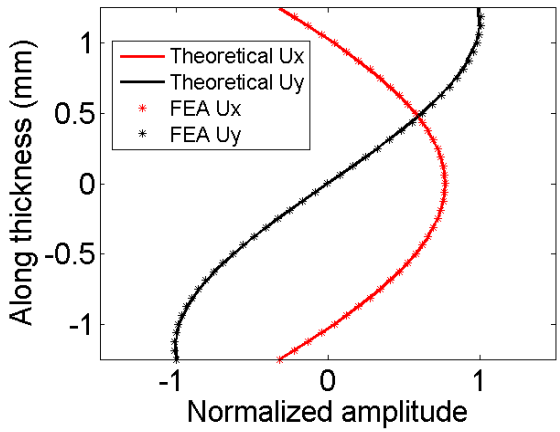

Fig. 5-7: Comparison of theoretical and simulated mode shapes

5.1.3 Effect of Varying Notch Depths on Transmission Coefficients

After the FEA model is validated, the notch depth is changed to investigate the effect of the varying notch depths on the transmission coefficients of the excited Lamb wave in the plate. Fig. 5-8 shows the 2-D FT of the "B-scan" signals of the same 200 surface nodes, which are located on the right of the notch, when the S0 mode Lamb wave at 0.9771 MHz is excited and the notch depth equals 1.5 mm. The theoretical dispersive curves of the A0, S0 and A1 modes are superimposed in Fig. 5-8. In addition to the excited Lamb wave, A0 and A1 modes of the same frequency are observed in the "B-scan" signals because of the mode conversions occurring at the notch.

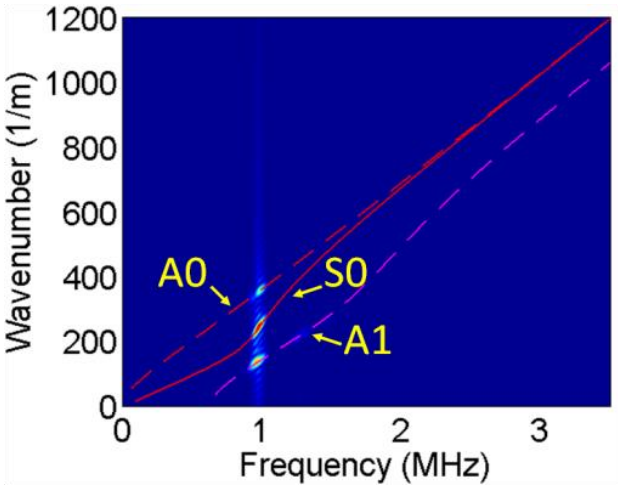

Fig. 5-8: 2-D FT of surface node signals when notch depth equals 1.5 mm

The transmission coefficient of the excited wave is calculated using

$$C_{tr} = A_d / A_0 \qquad \textbf{(Eq. 5-3)}$$

where A_d is the amplitude of the 2-D FT coefficient of the excited Lamb wave when the notch depth equals d, and A_0 is the amplitude of the 2-D FT coefficient of the excited Lamb wave when the notch depth equals zero. The theoretical dispersive curve in the wavenumber-frequency

domain is used to locate the 2-D FT coefficient of the excited Lamb wave. The notch depth changes from 0 mm to 2.25 mm at increments of 0.25 mm to calculate transmission coefficients of the excited Lamb wave at different notch depths. The relationship of the transmission coefficient versus the notch depth can be established for the excited Lamb wave. The loading condition is changed to model different Lamb waves identified in the LEU signals. Transmission coefficients of selected Lamb waves versus the notch depth are plotted in Fig. 5-9.

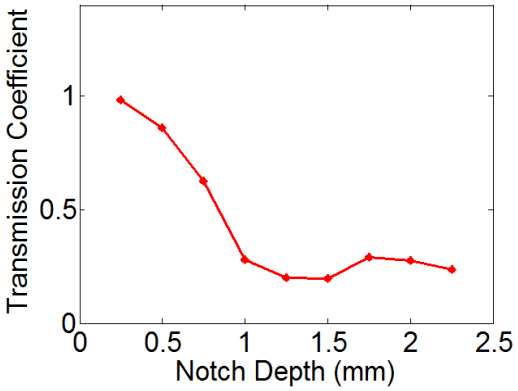

(a) A0 at 0.9771 MHz

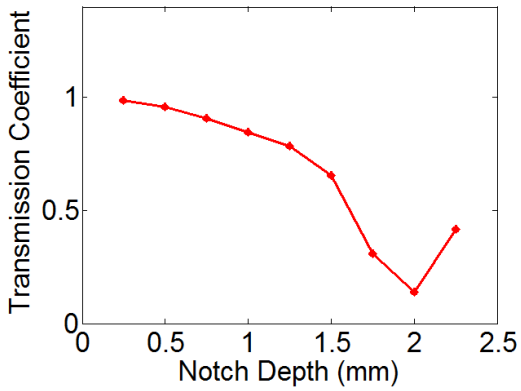

(b) S0 at 0.9771 MHz

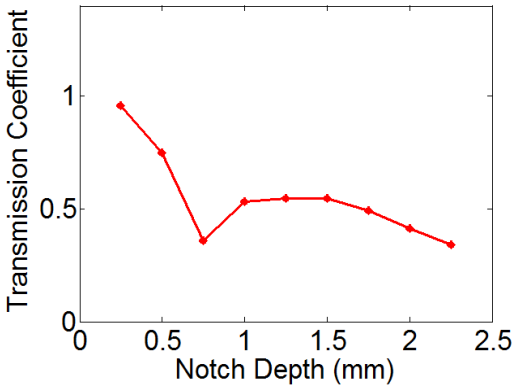

(c) A1 at 0.9771 MHz

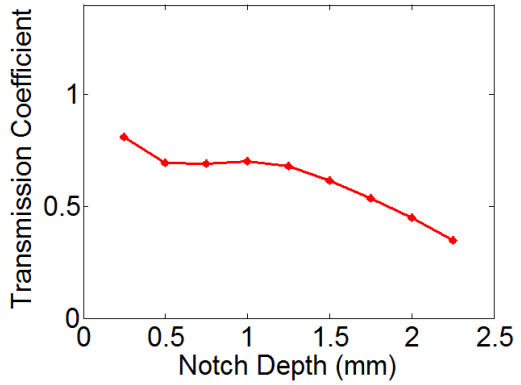

(d) S0 at 1.142 MHz

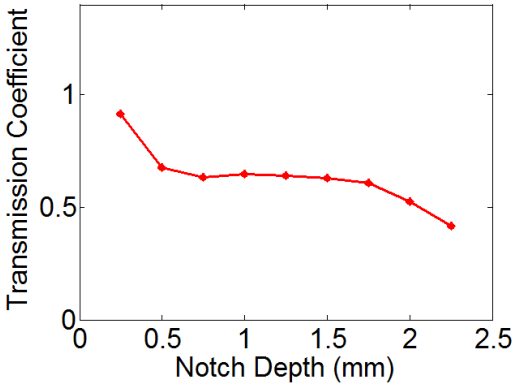

(e) S1 at 1.163 MHz

Fig. 5-9: Relationships between transmission coefficients and notch depth from FEA simulation

5.2 Experimental Study

Experiments are conducted to verify the relationships between the transmission coefficients and the varying notch depths established using the FEA study. A 1 mm wide notch is machined on a 2.5 mm thick A36 steel plate. The notch depth changes from 0.25 mm to 2.25 mm at increments of 0.5 mm, as shown in Fig. 5-10. Each depth is 40 mm long. The LEU technique will inspect from the back side of the plate to investigate how the varying notch depths will affect the transmission coefficients of different Lamb waves in the LEU signals.

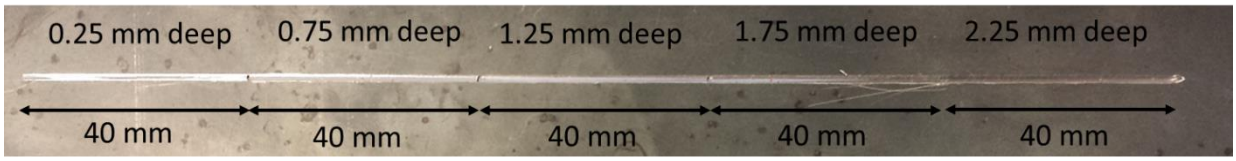

Fig. 5-10: Close look of notch with varying depths

5.2.1 Inspection Setup and Procedure

Figure 5-11 shows the setup used to inspect the sample plate. The plate is fixed vertically on the sample stage with back side facing the EMAT and the laser. The notch on the plate is

orientated horizontally. The EMAT is mounted on a stand, which has a slider to allow it to attach to the plate through its built-in magnet. The EMAT stand is fixed onto the experimental bench. The laser beam is delivered through a convex lens and focuses to a point source on the plate with a 0.5 mm radius. The pulsed laser is set to be 115 mJ/pulse, which excites ultrasounds in the ablative regime. The sampling frequency is set to be 12.5 MHz.

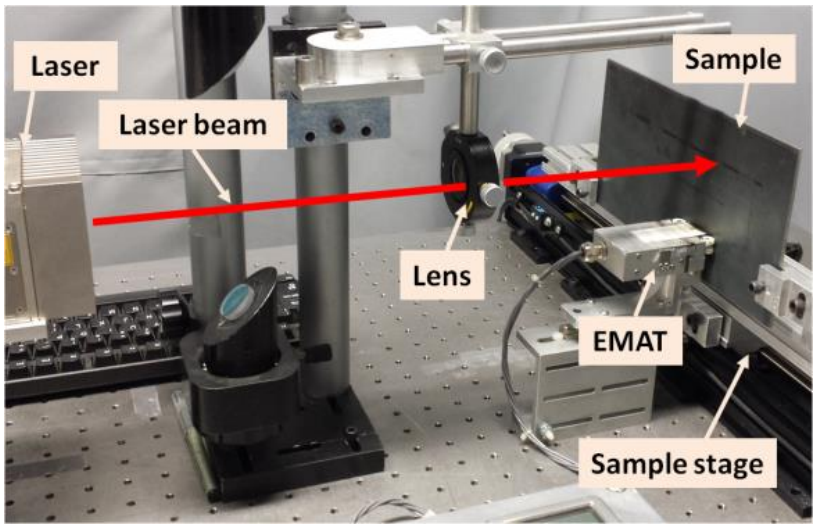

Fig. 5-11: Inspection setup for measuring different notch depths

Figure 5-12 shows the inspection procedure. The laser and the EMAT are located on the side of the plate opposite from where the notch is located. The laser source excites ultrasounds on one side of the notch, and the EMAT receiver picks up signals on the other side of the notch. During the inspection, the plate moves with the sample stage horizontally, which allows the laser and EMAT pair to inspect at different locations along the notch. The laser-to-EMAT distance is kept constant at 64 mm, and the EMAT-to-notch distance is kept constant at 47 mm. For each notch depth, 16 locations at increments of 1 mm are inspected in the center region. At each location, the laser fires 16 times, and the acquired signals are averaged to improve the SNR. A

reference signal is acquired with the same laser-to-EMAT distance from a location where there is no notch. The reference signal will be used to calculate transmission coefficients later.

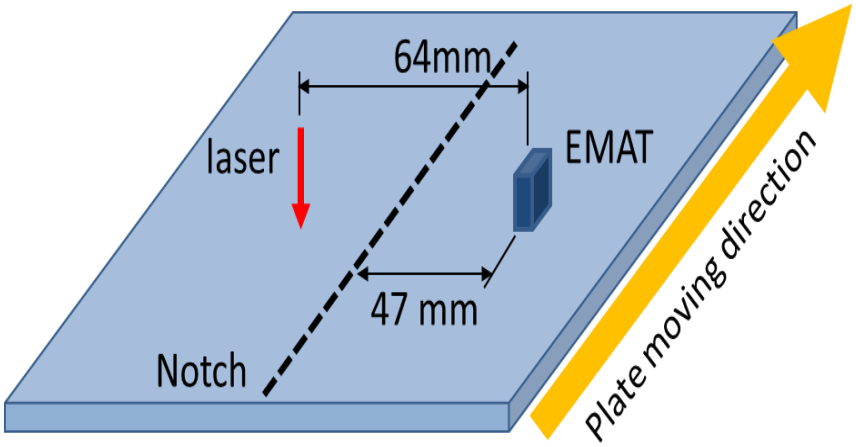

Fig. 5-12: Inspection procedure for measuring different notch depths

5.2.2 Calculation of Transmission Coefficients Using Continuous Wavelet Transform

AT each location along the notch, only one LEU signal is available. Therefore, 2-D FT cannot be used here to calculate transmission coefficients. As discussed in Chapter 3, CWT of individual LEU signals can partially separate different Lamb waves. CWT converts individual LEU signals to their time-frequency domain representations. Since the laser-to-EMAT distance is known, the theoretical arrival times of different Lamb waves can be calculated and superimposed to the CWT plots. The superimposed theoretical arrival times help to identify different Lamb waves in the time-frequency domain. For the acquired LEU signals in this work, CWT coefficients corresponding to different Lamb waves will be used to calculate their transmission coefficients.

The transmission coefficients of Lamb waves in the LEU signals are calculated using Eq. 5-4.

$$C_{tr} = CA_d / CA_0 \qquad \textbf{(Eq. 5-4)}$$

where CA_{d} is the CWT coefficient amplitude of a Lamb wave when the notch depth equals d, and CA_0 is the CWT coefficient amplitude of the same Lamb wave in the reference signal. In implementation, the root mean square of local CWT coefficient amplitudes is used to calculate the transmission coefficient of each Lamb wave of interest.

The complex-valued Morlet wavelet is used as the mother wavelet. As discussed in Chapter 3, different versions of complex-valued Morlet wavelet are good at identifying different Lamb waves in the LEU signals. Therefore, proper wavelet parameters are selected to calculate transmission coefficients for different Lamb waves. For example, the transmission coefficients of any A0 mode Lamb wave will be calculated using the wavelet in Fig. 3-6 (a) because it has a better capability to capture the A0 mode Lamb wave in the LEU signals.

Fig. 5-13 plots the relationships of the calculated transmission coefficients of selected Lamb waves versus the notch depth. Table 5-2 lists the wavelet parameters used to calculate transmission coefficients for these Lamb waves. For each Lamb wave of interest, 16 transmission coefficients corresponding to 16 locations are plotted for each depth. The transmission coefficients of these Lamb waves calculated from FEA simulation are also plotted.

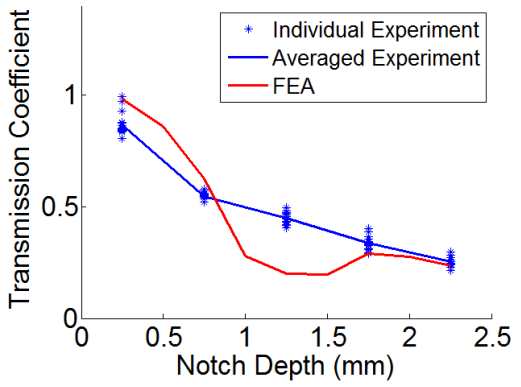

(a) A0 at 0.9771 MHz

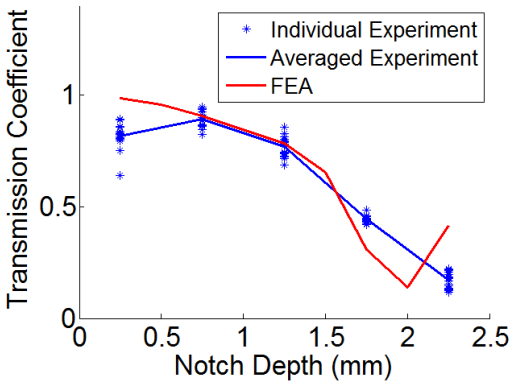

(b) S0 at 0.9771 MHz

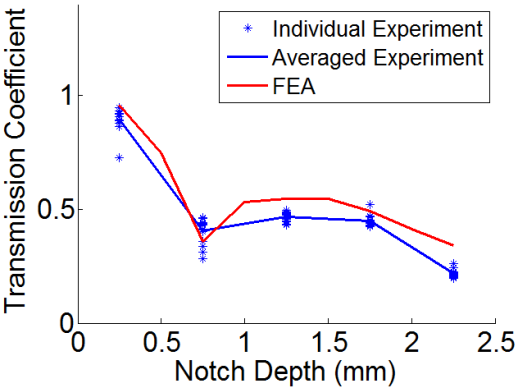

(c) A1 at 0.9771 MHz

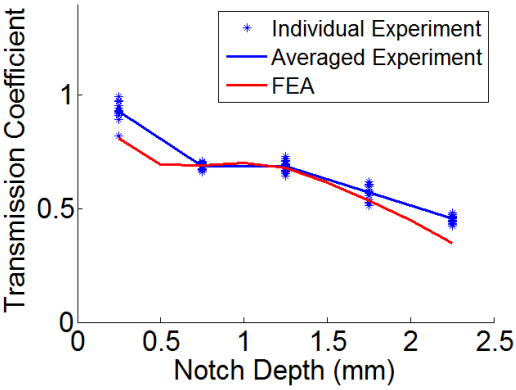

(d) S0 at 1.142 MHz

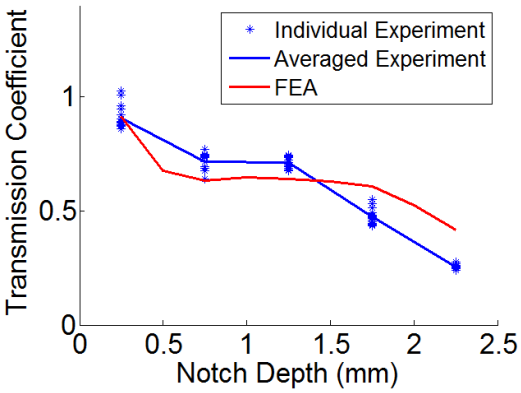

(e) S1 at 1.163 MHz

Fig. 5-13: Comparison of experimental and FEA results

The experimental and the FEA results match pretty well except a few discrepancies. The discrepancies are believed to be caused by several reasons. First, using CWT coefficients to

calculate Lamb waves' transmission coefficients is only an approximation. Secondly, the material properties used in the FEA model and used to locate the CWT coefficients may be slightly different from the real material properties of the sample plate. Thirdly, because of the low resolution in the time-frequency domain and the convolution nature of CWT, mode conversions may affect their nearby CWT coefficients in the received signals.

Table 5-2: Wavelet parameters used to calculate transmission coefficients

Lamb wave mode	Frequency (MHz)	Wavelet Parameters used
A0	0.9771	Fc = 1, Fb = 1
S0	0.9771	Fc = 1, Fb = 6
A1	0.9771	Fc = 1, Fb = 1
S0	1.142	Fc = 1, Fb = 6
S1	1.163	Fc = 1, Fb = 1

Transmission coefficients of some Lamb waves show sensitivity to the varying notch depths, which means that they can be used to predict the notch depths in thin structures.

5.3 Discussions

Mode conversions are not considered when calculating the transmission coefficients using the CWT coefficients because the converted waves propagate at different speeds from the original incident wave and therefore will arrive at different times in the received signals. The distance between the laser and the EMAT is kept constant so that the effect of the Lamb waves' attenuation on the calculated transmission coefficients can be diminished. Neither of the two selected wavelets can perfectly separate the different Lamb waves in the LEU signals. Therefore, transmission coefficients of Lamb waves located around intersections of different dispersive

curves are not calculated. The in-plane displacements of the surface nodes in the FEA model are used to calculate transmission coefficients. Using the out-of-plane displacements will yield the same results. Plus, the EMAT receiver used in this work is more sensitive to the in-plane particle motions.

5.4 Summary

Transmission coefficients of different Lamb waves in the LEU signals are calculated using both FEA simulation and experimental method. For the FEA simulation, transmission coefficients are calculated based on 2-D FT of "B-scan" signals from multiple surface nodes. For the experimental method, the transmission coefficients are calculated based on CWT of individual LEU signals. The relationships of the calculated transmission coefficients using the two different methods versus the varying notch depths match very well, which proves that CWT provides an efficient and effective way to calculate transmission coefficients of Lamb waves in LEU signals. Transmission coefficients of some Lamb waves in the LEU signals show sensitivity to the notch depth, which suggests that it is possible to use transmission coefficients of sensitive Lamb waves in the LEU signals to predict WPDs in thin structures.

CHAPTER 6

Measurement of Weld Penetration Depth in Thin Structures Using CWT-based Transmission coefficients of Laser-generated Lamb Waves

Chapter 5 shows that transmission coefficients of some Lamb waves in the LEU signals have the potential to predict WPDs in thin structures. It also shows that CWT of individual LEU signals can be used to calculate transmission coefficients of different Lamb waves, which is very attractive because it enables the LEU technique to inspect WPDs quickly. Chapter 6 will use real welds to investigate if CWT-based transmission coefficients of laser-generated Lamb waves can predict WPDs in thin structures. First, welds of varying penetration depths will be manufactured using gas metal arc welding. Secondly, the welded samples will be inspected non-destructively using the LEU technique. Thirdly, the welded samples will be cut-checked to measure their real WPDs. Fourthly, CWT-based transmission coefficients of different Lamb waves are calculated to select a set of Lamb waves whose transmission coefficients are sensitive to the varying WPDs. Finally, transmission coefficients of the selected Lamb waves will be used to train a neural network to predict WPDs in thin structures.

6.1 Sample Preparation

Gas metal arc welding (GMAW) is the most common industrial welding process for its versatility, speed and the relative ease of adapting the process to robotic automation. As shown in Fig. 6-1, the welding process forms an electric arc between a consumable wire electrode and the work piece metal, which heats the work piece metal, causing it to melt and join. Along with

the wire electrode, a shielding gas feeds through the welding torch, which shields the process from contaminants in the air. There are four primary methods of metal transfer in GMAW, called globular, short-circuiting, spray, and pulsed-spray, depending on different welding parameter settings.

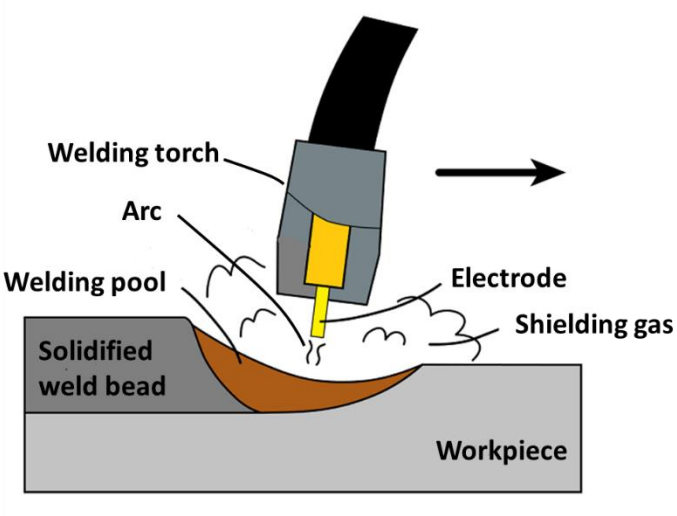

Fig. 6-1: Gas metal arc welding

Fig. 6-2 shows the welding system used in this work. Two workpieces are positioned butt to butt on a moving stage. A welding torch is held perpendicularly above the workpieces. When the stage moves beneath the welding torch, a weld can be produced along the butt joint between the two workpieces. A Miller Pulstar 450 welder is used in this system. The welder provides an interface to control two welding parameters through external analog signals during the welding process. They are the arc voltage and the wire feed rate (WFR) of the consumable electrode. The arc voltage is controlled by an analog signal ranging from 0 to 10 V, which corresponds to 0 to 50 V arc. The WFR is controlled by an analog signal ranging from 0 to 8 V, which corresponds to 0 to 800 in/min WFR. A microcontroller module developed by a previous student, Matthew Rogge, is

used to control the two welding parameters during the welding process. The microcontroller module also controls the start/stop actions of the welder. The moving stage is driven by a step motor and a ball screw. The step motor has a resolution of 0.78 degrees per step. Given the lead of the ball screw, this corresponds to a linear resolution of 6 μm per step. The microcontroller module also controls the start/stop actions of the step motor and its speed. After the welding parameters are loaded to the microcontroller, the welding process is fully automated by the microcontroller. Welds of different penetration depths can be produced by changing the welding parameters and the stage moving speed during the welding process.

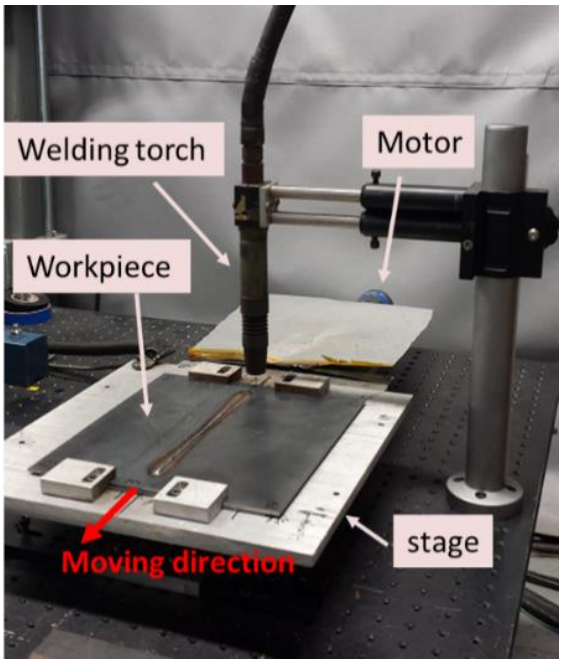

Fig. 6-2: Welding system

Totally six 8 inch long butt joint welds are manufactured using the welding system. Each weld is produced by joining two 2.9 mm thick A36 steel plates. Two set of welding parameter profiles are designed to control the welding process. The welding parameters vary during the welding

process to produce welds of different penetration depths. The two set of welding parameter settings are pretested to produce a wide range of different WPDs. Fig. 6-3 shows the first set of welding parameters. The arc voltage ramps from 22 V to 16 V for the first half run, and then ramps back to 22 V for the second half run. The wire feed rate steps from 240 in/min to 100 in/min for the first half run at increments of 20 in/min, and then steps back to 240 in/min for the second half run. Fig. 6-4 shows the second set of welding parameters. The arc voltage stays at 16 V initially, then ramps to 22 V, and finally stays at 22 V. The wire feed rate steps from 100 in/min to 240 in/min at increments of 20 in/min.

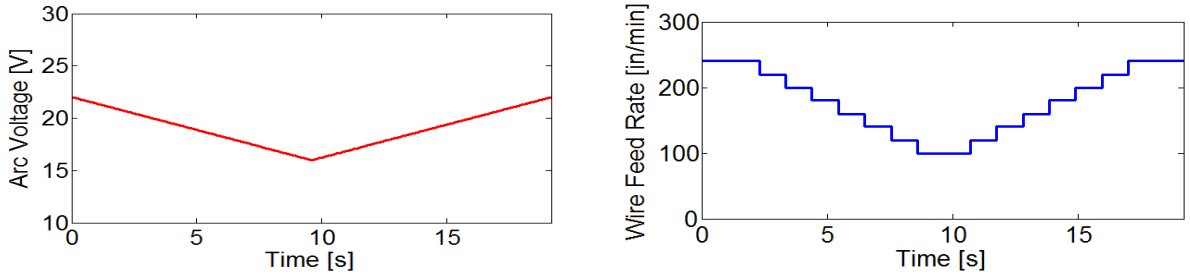

(a) Profile of arc voltage (b) Profile of wire feed rate

Fig. 6-3: First set of welding parameters

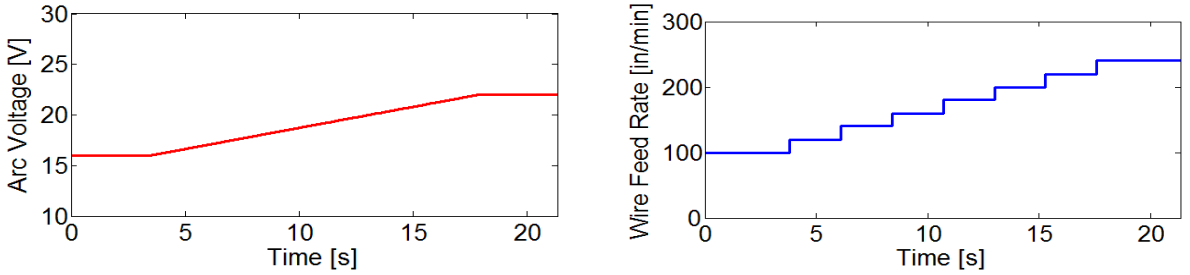

(a) Profile of arc voltage (b) Profile of wire feed rate

Fig. 6-4: Second set of welding parameters

Error! Not a valid bookmark self-reference. summarizes the parameter settings for producing each weld. In fact, the first 4 welds are manufactured first, which will be used to develop the

neural network. Weld # 5 and 6 are manufactured after the neural network is developed, which can provide additional test of the developed neural network.

Table 6-1: Parameter setting for each weld

Weld #	Length	Stage speed	Welding parameters
1	8 inch	25 in/min	1st set
2	8 inch	22.5 in/min	1st set
3	8 inch	22.5 in/min	1st set
4	8 inch	25 in/min	1st set
5	8 inch	22.5 in/min	1st set
6	8 inch	22.5 in/min	2nd set

6.2 Inspection Setup

After the welds are manufactured, they are non-destructively inspected using the LEU technique so that the transmission coefficients of Lamb waves in the LEU signals can be calculated. Fig. 6-5 shows the setup to inspect the welded samples, which is very similar to the setup used in Chapter 5. The welded sample is held vertically on the sample stage with weld bead facing the laser and EMAT. The weld seam is oriented horizontally. The laser beam is focused to a point source above the weld seam to excite ultrasounds, and the EMAT is receiving ultrasounds below the weld seam. The laser-to-EMAT distance is 64 mm, and the laser-to-weld distance is 47 mm. These distances are kept constant. During the inspection, the sample moves with the stage, and the laser/EMAT pair inspects at 91 locations with an increment of 2 mm along the weld seam. At each location, the laser fires 16 times, and the acquired signals are averaged to improve the SNR. The laser power is set to 115 mJ/pulse. The sampling frequency is set to 12.5 MHz. The received LEU signals are stored in PC for signal processing later. A reference signal is acquired on

a 2.9 mm thick defect-free steel plate with the same laser-to-EMAT distance. The reference signal will be used to calculate transmission coefficients later, in the same way as in Chapter 5.

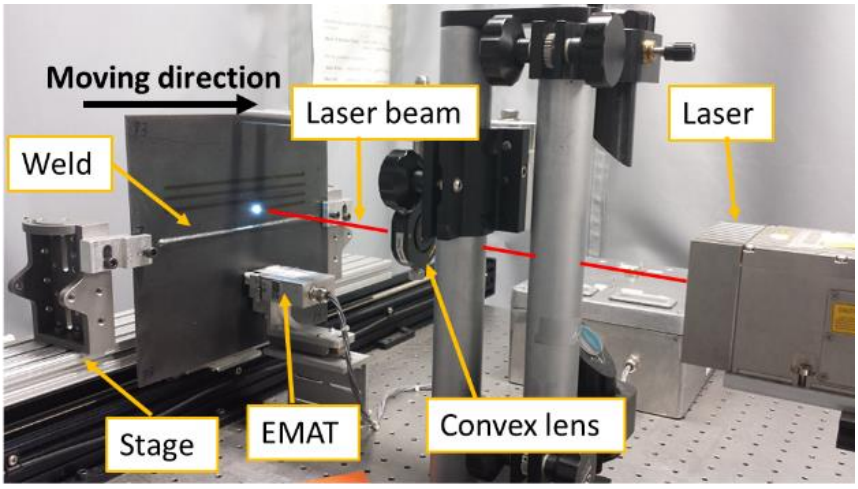

Fig. 6-5: LEU setup for inspecting welded samples

6.3 Cut Check of Weld Penetration Depth

After the welded samples are inspected using the LEU technique non-destructively, the welds are cut along the middle line of the weld seams to measure the real WPDs. Due to the width of saw blades, it is very difficult to cut accurately along the middle line of weld seams. In practice, the welds are cut along a line 2 mm off the middle line, and the rest is grinded off using grit 80 sandpapers. This way makes sure that the real WPDs can be measured accurately. After grinding, the cross-sections are etched using 5% sulfuric acid to make the boundaries between the weld material and the base material clear to see. After etching, the samples are placed in air for about 10 minutes and then scanned using an optical scanner with a 1200 dpi (dot per inch) resolution. Fig. 6-6 shows the scanned images of the six welds.

(a) Weld # 1

(b) Weld # 2

(c) Weld # 3

(d) Weld # 4

(e) Weld # 5

(f) Weld # 6

Fig. 6-6: Scanned images of welds in first set of samples

The Image Toolbox in MATLAB is used to measure WPDs at each inspected location along the welds. Fig. 6-7 plots the cut-check measured WPDs along each weld, and Fig. 6-8 shows the histogram plots of the cut-check measured WPDs from each weld. The predesigned welding parameters successfully produce varying WPDs in the six welds. Welds # 1-4 cover a wide range of WPDs from 0 mm to 2.9 mm, which are suitable to be used to develop the neural network to predict WPDs in thin structures.

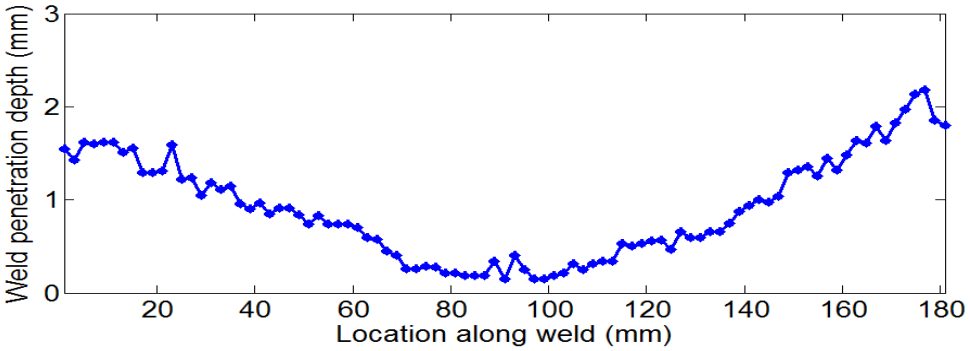

(a) Weld penetration depth along weld # 1

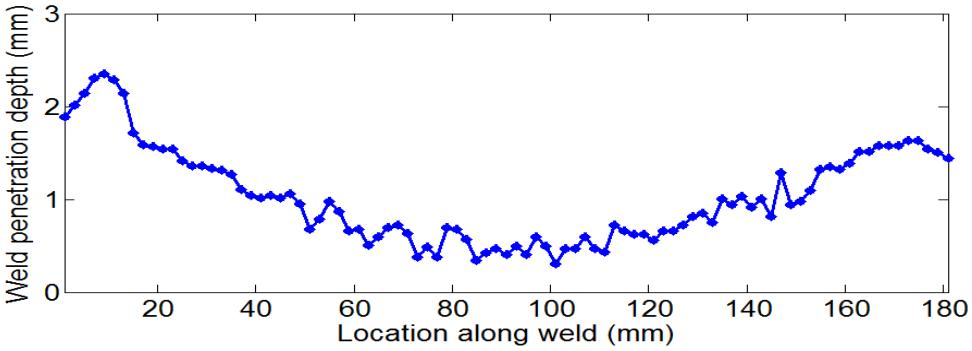

(b) Weld penetration depth along weld # 2

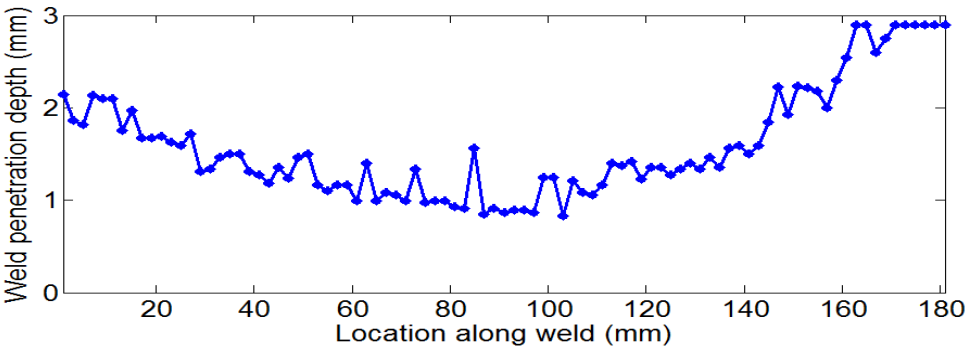

(c) Weld penetration depth along weld # 3

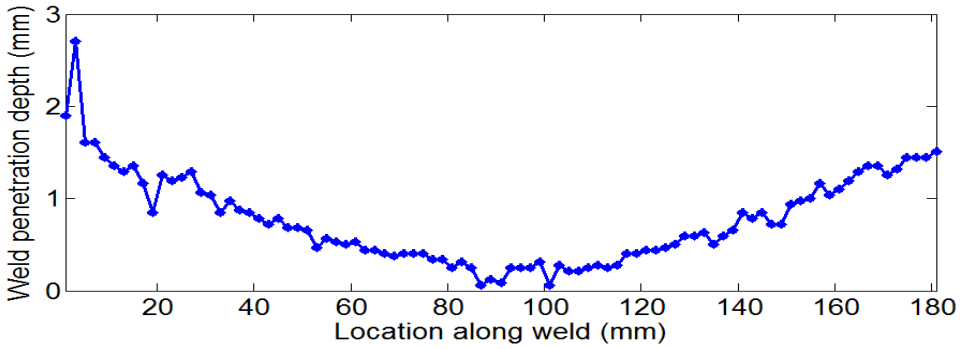

(d) Weld penetration depth along weld # 4

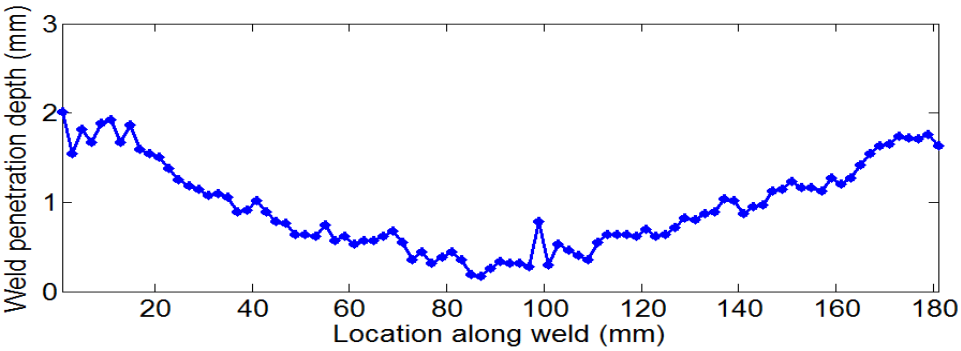

(e) Weld penetration depth along weld # 5

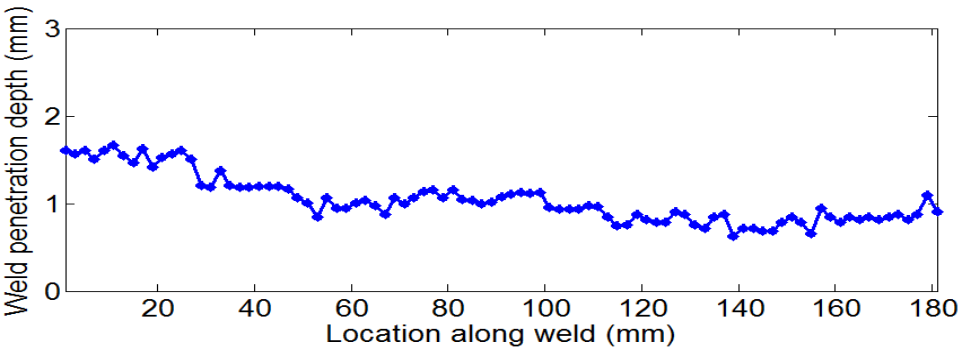

(f) Weld penetration depth along weld # 6

Fig. 6-7: Cut-check measured weld penetration depths

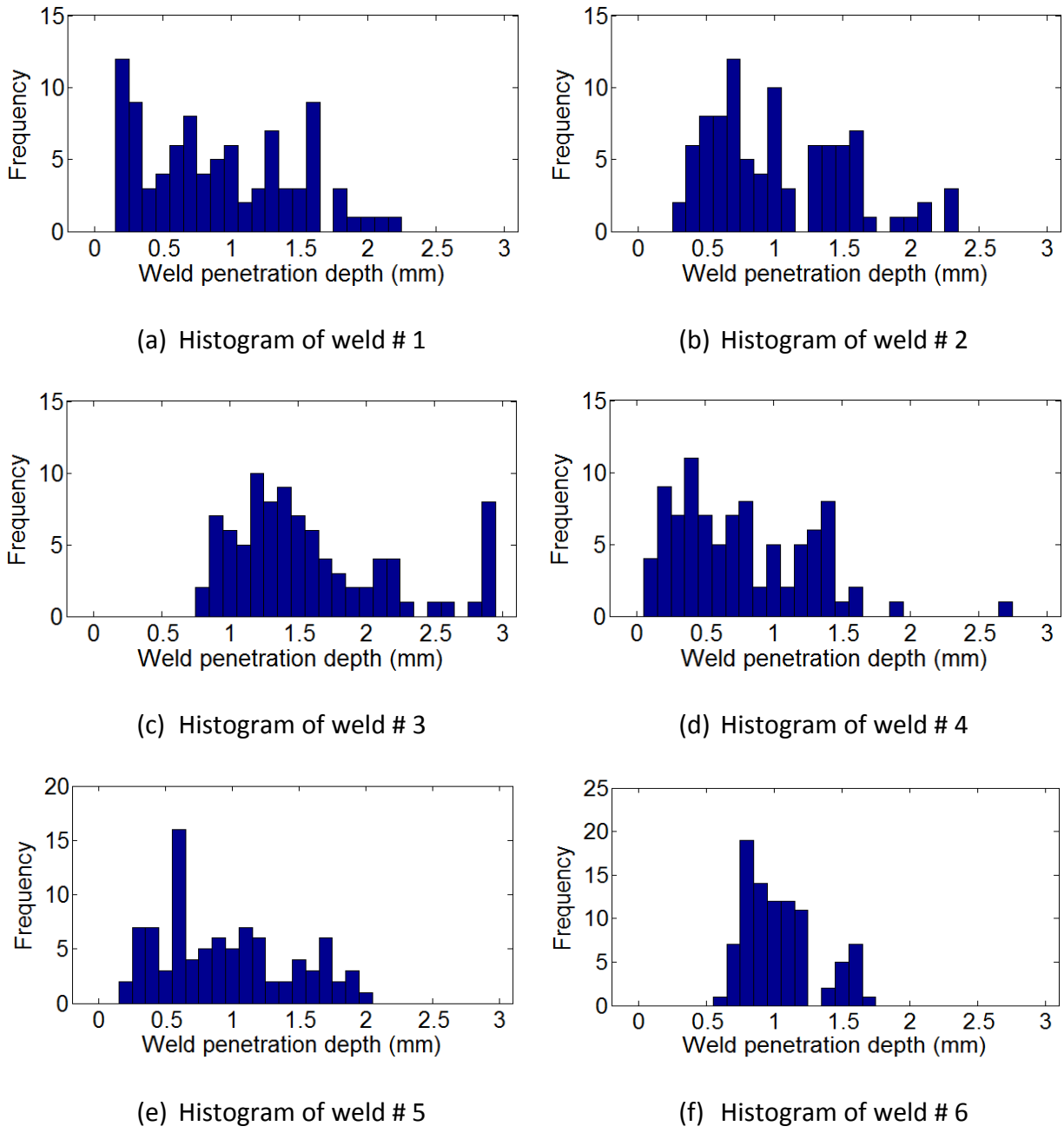

Fig. 6-8: Histogram of cut-check measured weld penetration depths

6.4 Selection of Lamb Waves

CWT converts the acquired LEU signals to the time-frequency domain. The CWT coefficients corresponding to different Lamb waves are used to calculate their transmission coefficients, as

discussed in Chapter 5. Two versions of complex-valued Morlet wavelets, cmor1-1 and cmor6-1, are used as the mother wavelets because of their capabilities to capture different Lamb waves in the LEU signals. Fig. 6-9 shows the reference signal. Fig. 6-10 shows its CWT plots using the two different mother wavelets. Theoretical dispersive curves corresponding to arrival times of different Lamb waves are superimposed to the two CWT plots.

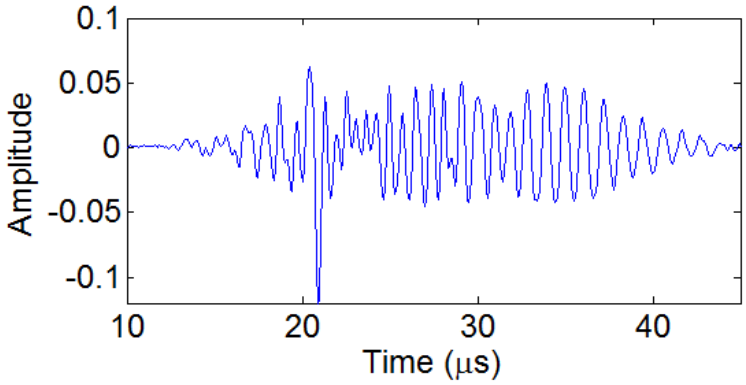

Fig. 6-9: Reference signal

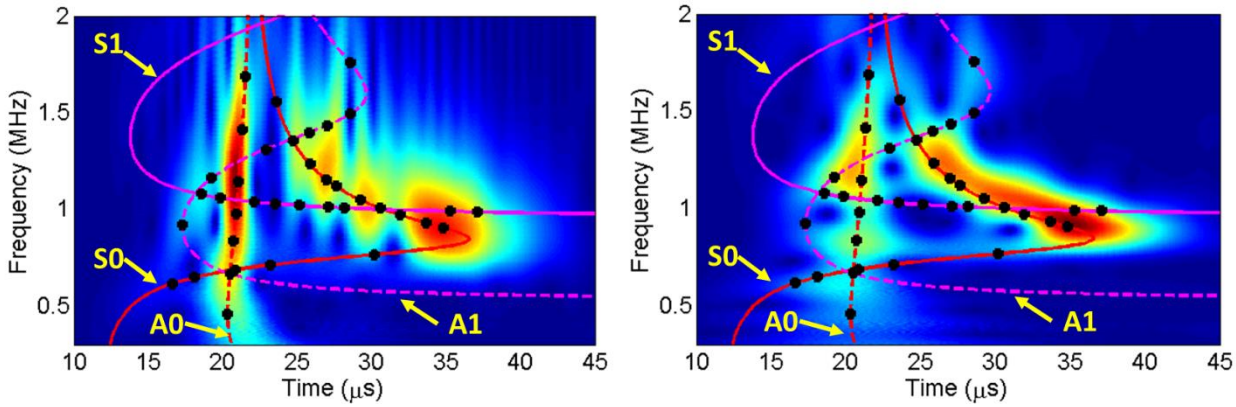

(a) CWT of reference signal using cmor1-1

(b) CWT of reference signal using cmor6-1

Fig. 6-10: CWT plots of reference signal using two different mother wavelets

The objective is to use transmission coefficients of Lamb waves to predict WPDs in thin structures. The LEU signals contain broadband and multimodal Lamb waves. It is necessary to

select Lamb waves which are sensitive to varying WPDs to calculate their transmission coefficients. Preliminary check of how CWT plots of LEU signals are affected by different WPDs helps to select an initial set of 38 Lamb waves. Table 6-2 lists the initial set of selected Lamb waves and the wavelets used to calculate their transmission coefficients. The initial set of selected Lamb waves are plotted as black dots in Fig. 6-10 (b) and (c), which show that the initial set of selected Lamb waves cover the majority of the strong Lamb waves in LEU signals identified in Chapter 3.

For the 364 LEU signals acquired from weld # 1-4, transmission coefficients of the initial set of selected Lamb waves are calculated and investigated against the cut-check measured WPDs. Fig. 6-11 shows scatter plots of the calculated transmission coefficients versus the cut-check measured WPDs. Some of the scatter plots exhibit certain patterns, such as the ones corresponding to A0 mode Lamb wave at 0.4586 MHz and A1 mode Lamb wave at 1.161 MHz, which means the transmission coefficients of corresponding Lamb waves are sensitive to the varying WPDs. However, for some Lamb waves such as S0 mode at 0.9061 MHz, no pattern is found in their scatter plots, which means the transmission coefficients of these Lamb waves are not sensitive to the WPD. After the screening process, 23 sensitive Lamb waves are finally selected, which are highlighted in Table 6-2 and plotted in Fig. 6-12 as black dots. For some Lamb waves, their transmission coefficients exceed 1, which can be interpreted by mode conversions occurring at the weld.

Table 6-2: Initial selection of Lamb waves for calculating transmission coefficients

Lamb Mode	Frequency (MHz)	Wavelet Used	Index
A0	0.4586	cmor1-1	1
	0.667	cmor1-1	2
	0.8362	cmor1-1	3
	0.9776	cmor1-1	4
	1.144	cmor1-1	5
	1.411	cmor1-1	6
	1.686	cmor1-1	7
S0	0.6157	cmor1-1	8
	0.6474	cmor1-1	9
	0.6871	cmor6-1	10
	0.7122	cmor6-1	11
	0.766	cmor6-1	12
	0.9061	cmor6-1	13
	0.9315	cmor6-1	14
	0.9713	cmor6-1	15
	1.006	cmor6-1	16
	1.05	cmor6-1	17
	1.119	cmor6-1	18
	1.154	cmor6-1	19
	1.233	cmor6-1	20
	1.353	cmor6-1	21
	1.556	cmor6-1	22
A1	0.9211	cmor1-1	23
	1.161	cmor1-1	24
	1.309	cmor6-1	25
	1.396	cmor6-1	26
	1.433	cmor6-1	27
	1.493	cmor6-1	28
	1.757	cmor6-1	29
S1	0.9891	cmor6-1	30
	0.9921	cmor6-1	31
	1.009	cmor6-1	32
	1.013	cmor1-1	33
	1.022	cmor1-1	34
	1.03	cmor6-1	35
	1.04	cmor6-1	36
	1.061	cmor6-1	37
	1.078	cmor6-1	38

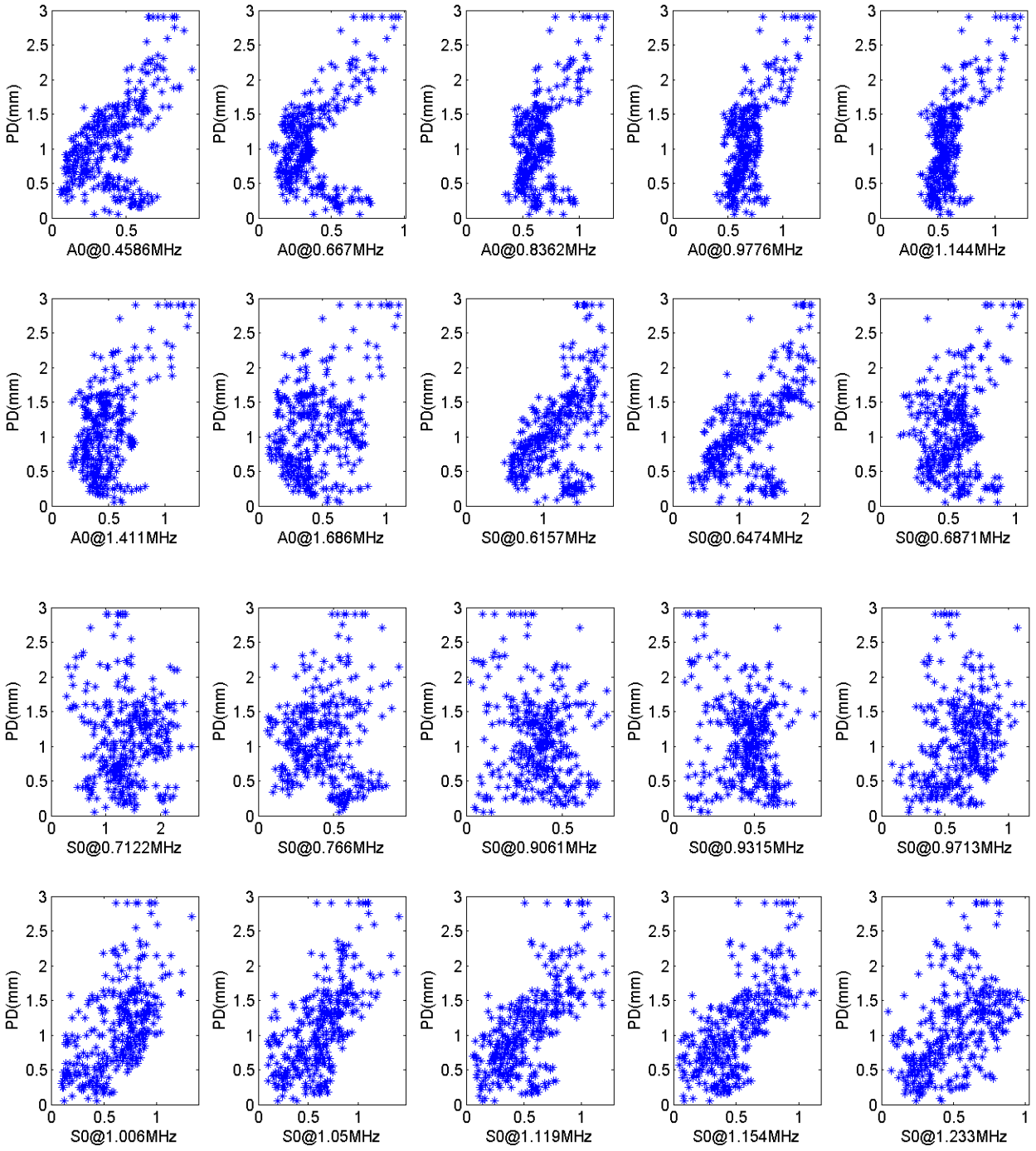
PD(mm)
A0@0.4586MHz
A0@0.667MHz
A0@0.8362MHz
A0@0.9776MHz
A0@1.144MHz
A0@1.411MHz
A0@1.686MHz
S0@0.6157MHz
S0@0.6474MHz
S0@0.6871MHz
S0@0.7122MHz
S0@0.766MHz
S0@0.9061MHz
S0@0.9315MHz
S0@0.9713MHz
S0@1.006MHz
S0@1.05MHz
S0@1.119MHz
S0@1.154MHz
S0@1.233MHz

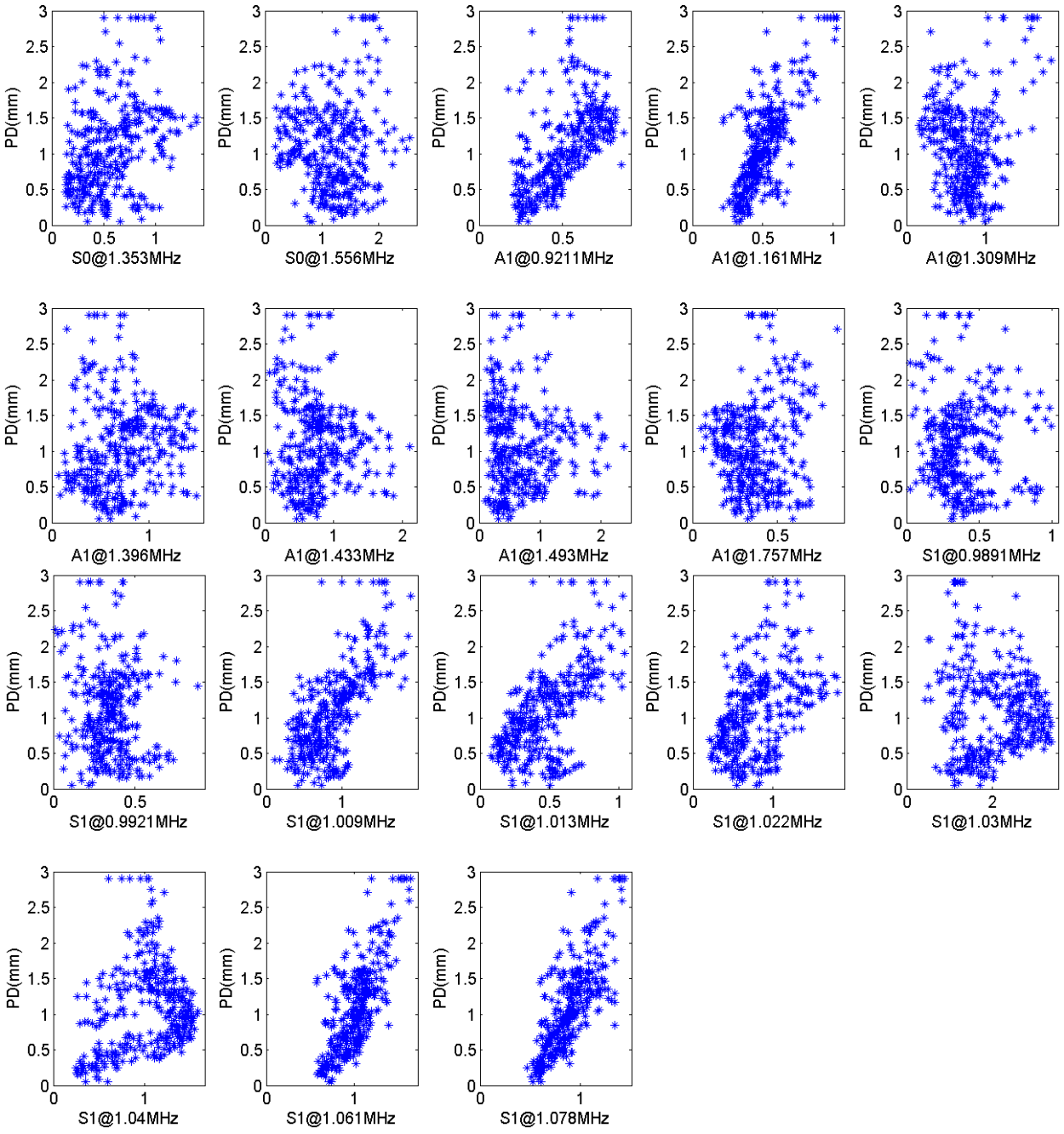

Fig. 6-11: Plots of transmission coefficients of selected Lamb waves vs. weld penetration depth

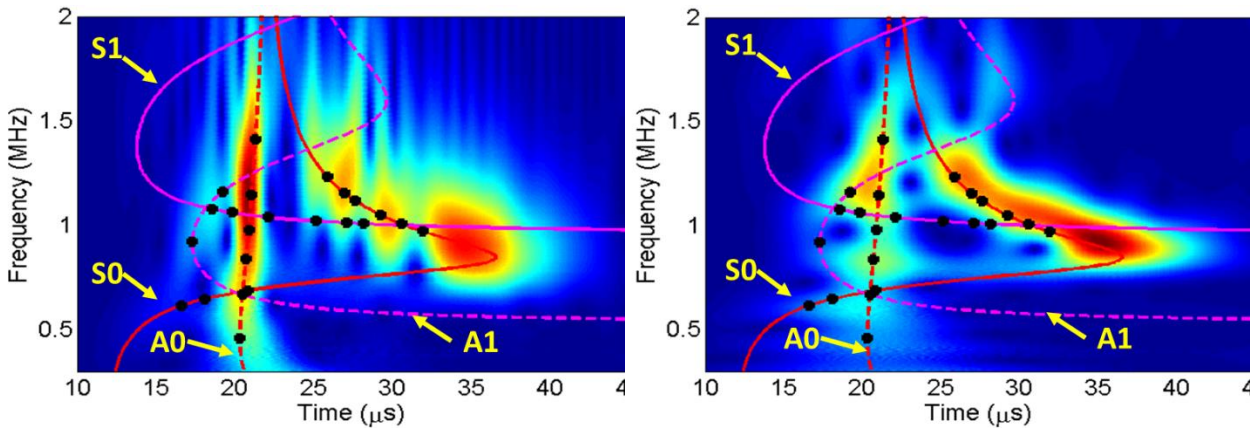

(a) CWT of reference signal using cmor1-1

(a) CWT of reference signal using cmor6-1

Fig. 6-12: Plots of selected Lamb waves in time-frequency domain

In addition to transmission coefficients of the 23 selected Lamb waves, the LEU signal energy calculated using sum of square is found to be also sensitive to varying WPDs, as shown in Fig. 6-13. The transmission coefficients of the 23 selected Lamb waves and the LEU signal energy will be used to predict the WPDs in thin structures.

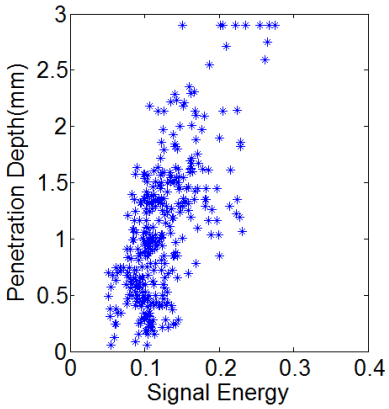

Fig. 6-13: Scatter plot of signal energy vs. weld penetration depth

The scatter plots of transmission coefficients of 23 selected Lamb waves and the signal energy versus the WPD are noisy, as shown in Fig. 6-11 and Fig. 6-13. The noises in the collected data

may be caused by many reasons. First, in addition to the varying WPDs, the other weld dimensions are also wildly varying at different inspected locations, such as weld reinforcement height, bead width, and the seam width between two plates. Secondly, the cut check measurement process may introduce errors. Thirdly, the LEU system is instable over time. Another important reason is illustrated in Fig. 6-14. Because the EMAT pickup coil is 20 mm long in the weld seam direction, the received signals are affected by WPDs of a region along the weld. However, the cut-check only measures the WPD at the center of this signal affecting region. WPDs within the signal affecting region may vary a lot.

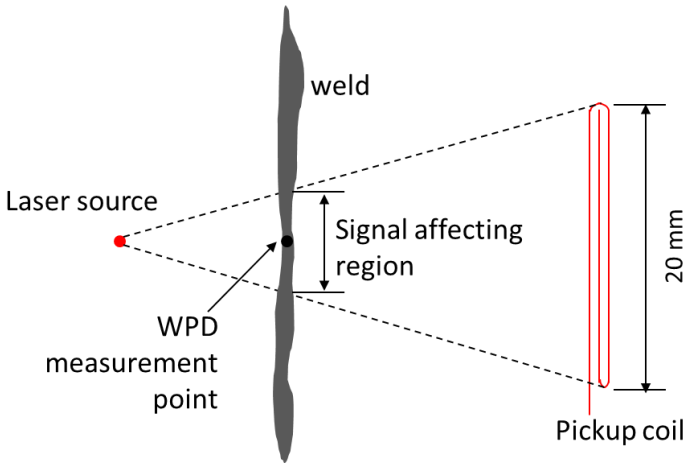

Fig. 6-14: Layout of laser and EMAT relative to weld seam

6.5 Artificial Neural Network

After Lamb waves whose transmission coefficients are sensitive to varying WPDs are selected, the prediction of WPDs becomes a data fitting problem. The inputs of the data fitting are the transmission coefficients of 23 selected Lamb waves, which are calculated based on the CWT of each acquired LEU signal, and the LEU signal energy. The output is the predicted WPD at the signal acquisition location. Fig. 6-11 shows that transmission coefficients of some selected Lamb

waves exhibit nonlinear relationships with the WPD. There are different information processing techniques available to solve nonlinear data fitting problems, such as nonlinear regression and stochastic approximation. Among these different techniques, artificial neural network (ANN) [58] proves the capability to provide equally comparable solutions with several additional appealing properties, such as fault-tolerance through the large number of connections, parallel implementations that allow fast processing, and on-line adaption which allows continuous improvements. ANN is used in this work for its fault-tolerance property.

Figure 6-15 shows the structure of the ANN used in this work, which is a two-layer feed-forward data fitting network. The input layer has 24 nodes accepting the 23 transmission coefficients and the LEU signal energy. The output layer has only one node yielding the predicted WPDs. The Universal Approximation Theorem (UAT) [59] states that a single hidden layer perceptron network with a sufficiently large number of neurons can approximate any continuous function arbitrarily close. The ANN used in this work contains 10 neurons in the hidden layer, which proves to provide a very good approximation later. The 10 hidden neurons use the sigmoid function as their activation functions, and the output neuron uses the linear function as its activation function.

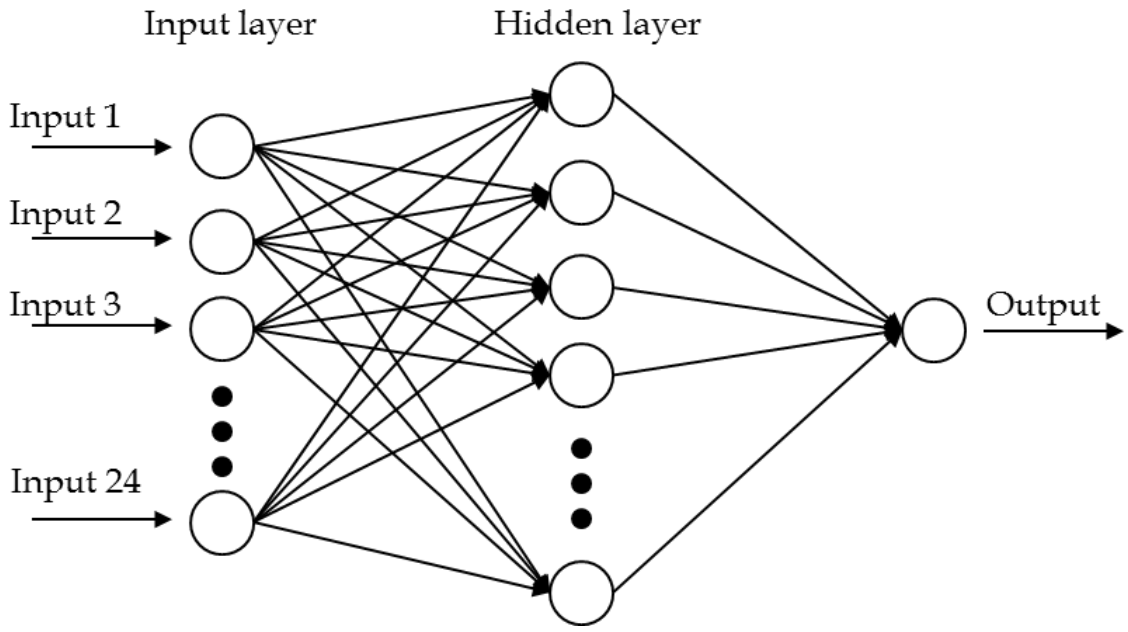

Fig. 6-15: Structure of neural network

The neural network fitting tool in MATLAB is used to perform the training. 364 sample points from weld # 1-4 are used to develop the network. These sample points are randomly divided into three groups. 70% of them are the training data, which are used for network training. 15% of them are the validation data, which are used to stop the training when the network generalization stops improving. The remaining are the test data, which are used to test the network performance during and after training independently. The mean square error (MSE) is used to calculate the network performance. The smaller the MSE is, the better the network performance is. The network is trained with Levenberg-Marquardt backpropagation algorithm until the network performance of the validation data stops improving. Fig. 6-16 keeps track of the performance of the training, validation and test data as the number of training epoch increases. The MSE of the training data keeps decreasing as the network training goes through more epochs. The MSE of the validation data decreases first and increases later. The best network

generalization occurs at Epoch 4, after which the MSE of the validation data starts increasing, that is, the network starts over-fitting. The MSE curve of the test data is very similar to the validation data, which indicates that the training result is acceptable. If the test curve increases significantly before the validation curve increases, over-fitting might have started before Epoch 4. At the best Epoch, the test data has a smaller MSE than the validation data.

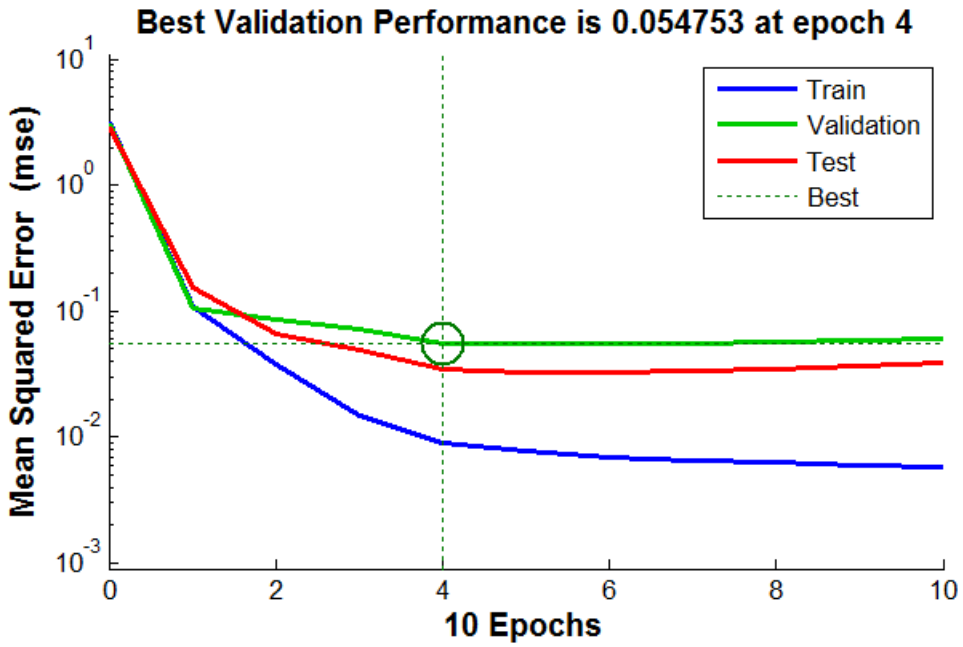

Fig. 6-16: Progress of performance during training process

Figure 6-17 shows the regression plots of network outputs (predicted WPDs) and targets (cut-checked WPDs) for the training, validation and test data at the best Epoch. If all the data points fall on the dashed line, the network provides a perfect prediction of WPDs, which is impossible. The solid line is the linear regression of the data points. The closer the solid line is to the dashed line, the better prediction the network provides. The R value measures the correlation between the outputs and targets. An R value close to 1 means a good prediction, and an R value close to 0 means a bad prediction. The test data has an R value of 0.96033, which means the trained

network has a good capability to predict WPDs in thin structures. Fig. 6-18 plots the predicted WPDs and cut-checked WPDs along welds # 1-4, which match very well. Even though the predicted WPDs are a mixture of training, validation and test data, they still show that the developed network predicts WPDs very well at different inspected locations.

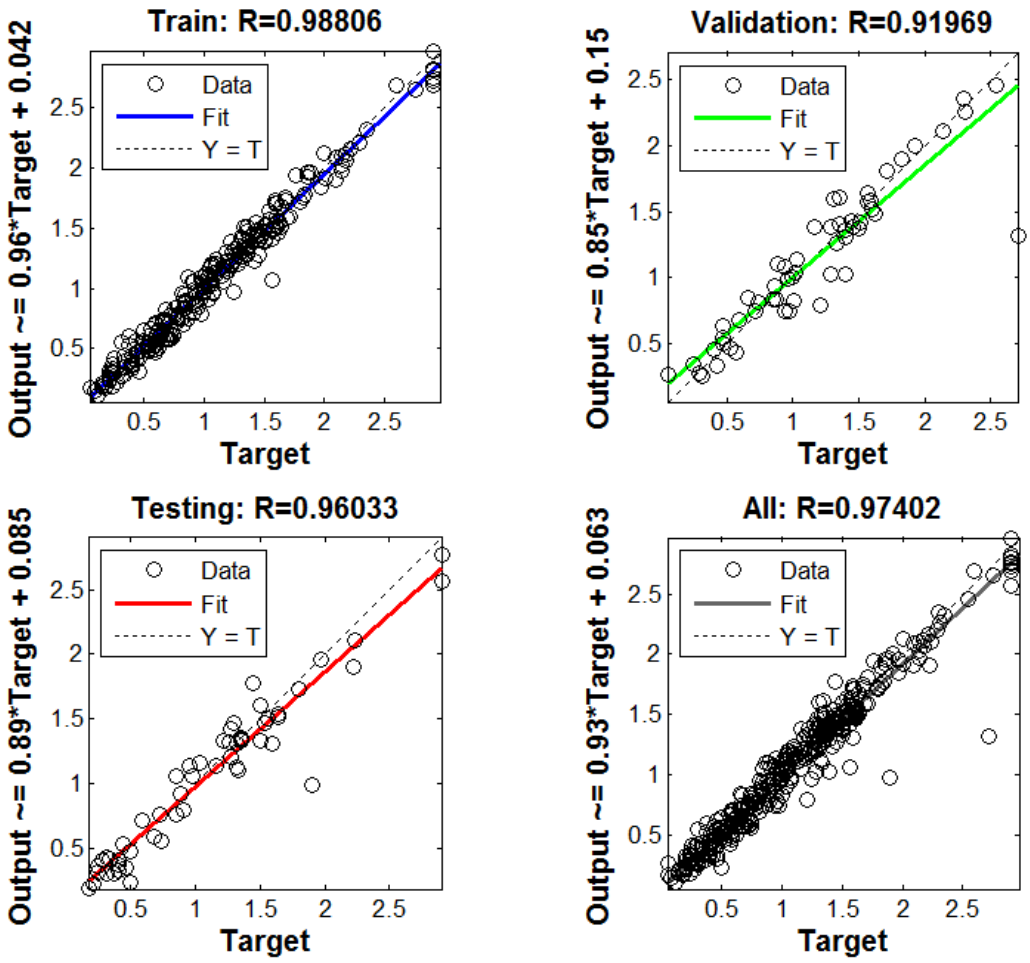

Fig. 6-17: Regression plots of network outputs and targets

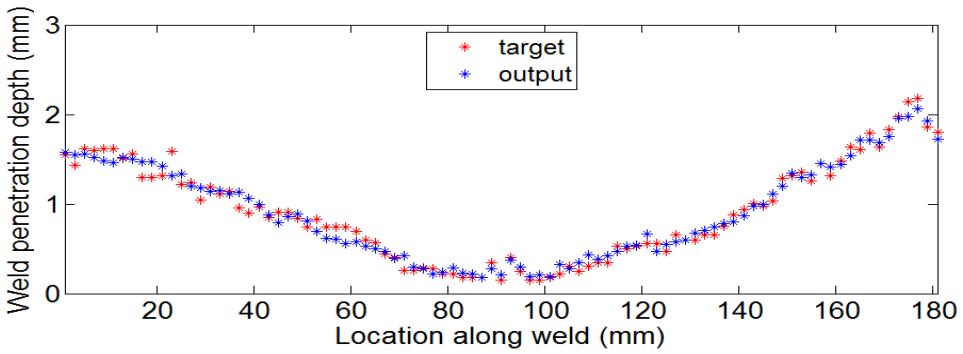

(a) Weld # 1

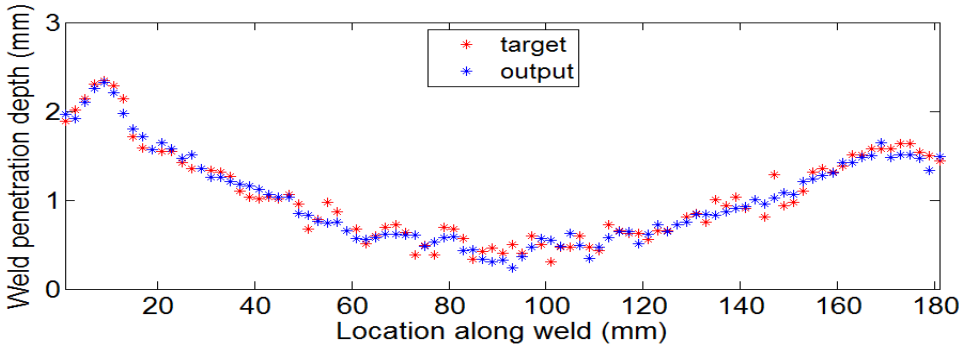

(b) Weld # 2

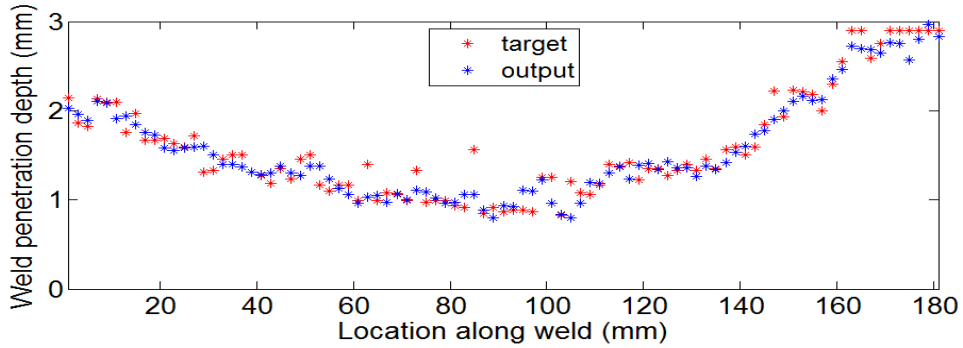

(c) Weld # 3

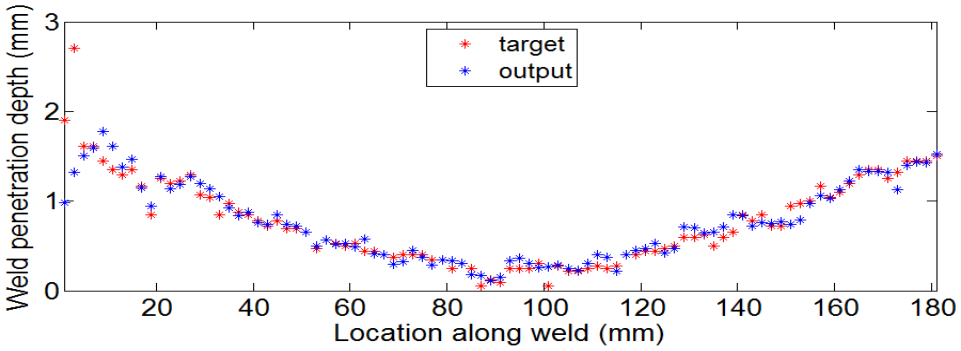

(d) Weld # 4

Fig. 6-18: Comparison of network outputs and targets along welds

Welds # 5 and 6 are not used in the development of the neural network. Therefore, they can provide additional test of the network independently. Transmission coefficients of the selected Lamb waves and the signal energy from welds # 5 and 6 are fed into the developed ANN to predict WPDs at the inspected locations. Fig. 6-19 shows the predicted WPDs and the cut-checked WPDs along welds # 5 and 6. Fig. 6-20 shows the regression plots of network outputs and targets for these two welds. The predictions match well with the cut-checked WPDs, which further confirms the performance of the developed network. Weld # 5 has an R value of 0.95811. Weld # 6 has an R value of 0.89264, which is a little lower than Weld # 5 partially because Weld # 6 has a small range of WPDs. The combined R value for the two welds is 0.90907, which is acceptable.

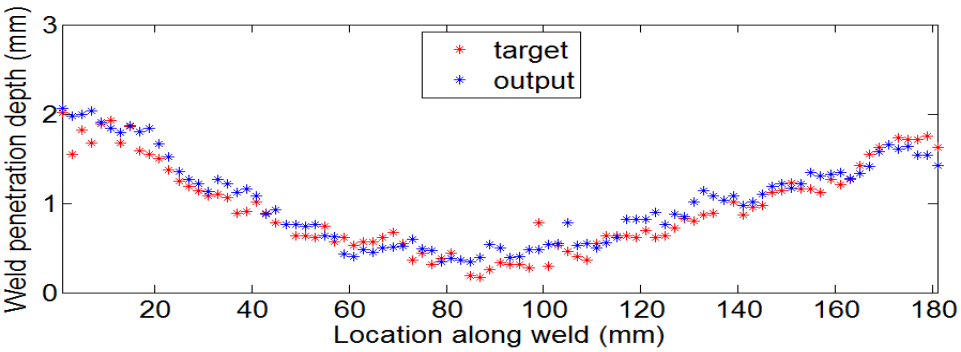

(a) Weld # 5

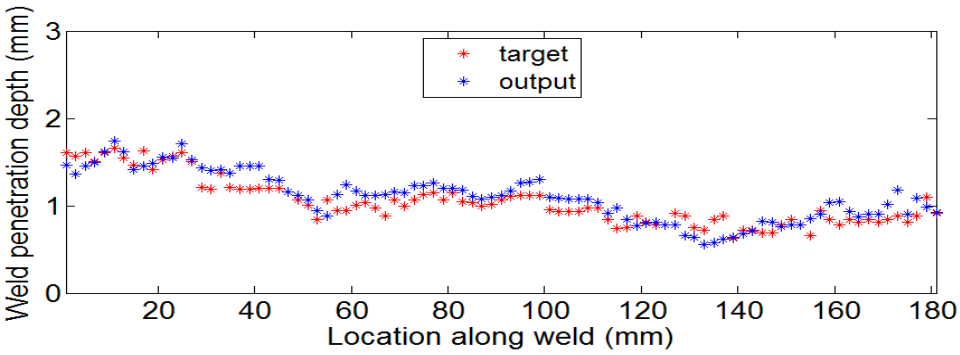

(b) Weld # 6

Fig. 6-19: Comparison of network outputs and targets for welds # 5 and 6

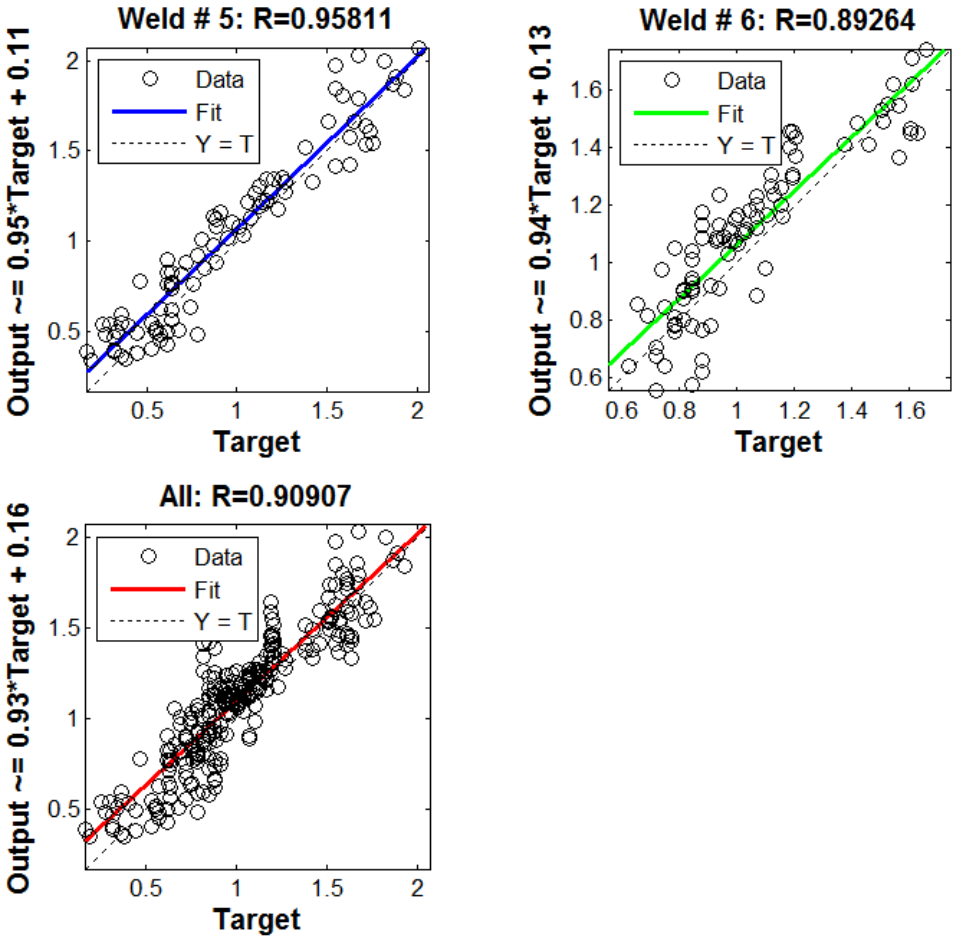

Fig. 6-20: Regression plots of network outputs and targets for additional test data

6.6 Regression Analysis

For comparison purpose, regression models are developed to predict WPDs based on transmission coefficients of selected Lamb waves and the LEU signal energy. Since there is no guideline to determine the form of the regression model, linear regressions are used in this work. As seen in Fig. 6-11, transmission coefficients of some Lamb waves exhibit nonlinear relationships with WPDs. For these Lamb waves, square root and quadratic terms of their transmission coefficients will be included in the model to account for the nonlinearity. Table 6-3 lists all the terms included in the full model.

Table 6-3: Terms included in full model

Lamb Mode	Frequency (MHz)	Linear Term	Square Root Term	Quadratic Term
A0	0.4586	✓	✓	✓
	0.667	✓	✓	✓
	0.8362	✓		
	0.9776	✓		
	1.144	✓		
	1.411	✓		
S0	0.6157	✓	✓	✓
	0.6474	✓	✓	✓
	0.6871	✓		
	0.9713	✓		
	1.006	✓		
	1.05	✓		
	1.119	✓		
	1.154	✓		
	1.233	✓		
A1	0.9211	✓		
	1.161	✓		
S1	1.009	✓		
	1.013	✓		
	1.022	✓		
	1.04	✓	✓	✓
	1.061	✓		
	1.078	✓		

Energy		✓		

Scatter plots of some sensitive Lamb waves are similar, which means that they are not independent from each other. The developed neural network used all of them because the redundancy of information helps to improve its fault-tolerance capability. However, in regression analysis, fewer predictors are preferred. The forward stepwise method is used to search for the best model based on the Akaike Information Criterion (AIC) [60]. The idea is to select a set of terms which minimize the AIC value. The selected terms using the forward stepwise method are highlighted in Table 6-3. Welds # 1-4 are used to develop the model. Fig. 6-21 shows the diagnostic plots of the selected model. There is no pattern in the residual plot, which means the model captures the underlying relationship pretty well. For the model development data, the predicted and the cut-checked WPDs have an R value of 0.9426.

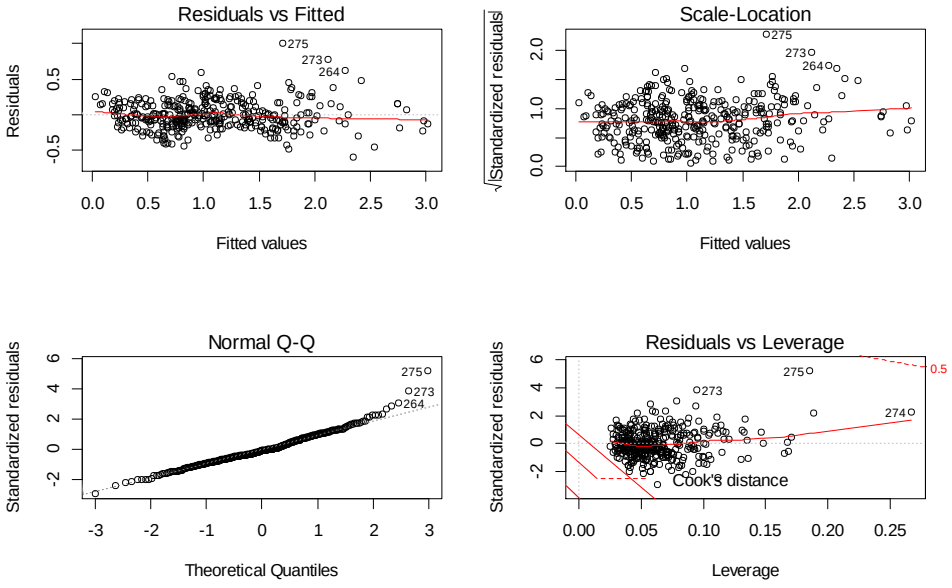

Fig. 6-21: Diagnostic plots of selected model using model development data

Welds # 5-6 are used to validate the developed model. Fig. 6-22 shows the predicted WPDs and cut-checked WPDs along Weld # 5 and 6. Fig. 6-23 shows the regression plots of regression predictions and targets for the two welds. For the validation data, the predicted and the cut-checked WPDs have a combined R value of 0.73182, which is much lower than the neural network predictions. This means that the underlying relationship is not fully captured by the selected model.

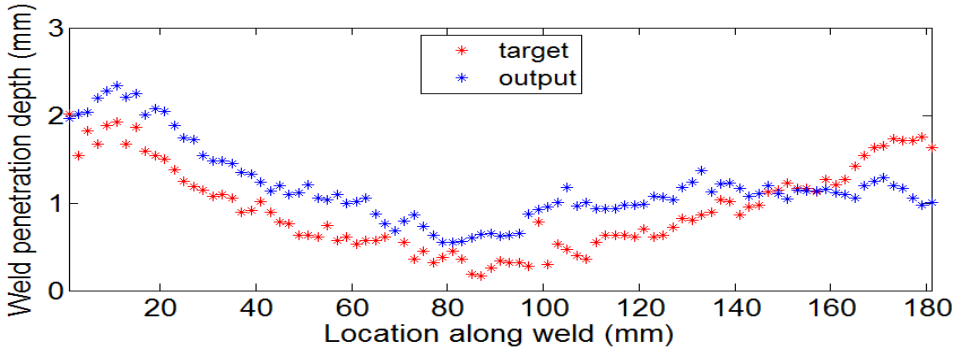

(a) Weld # 5

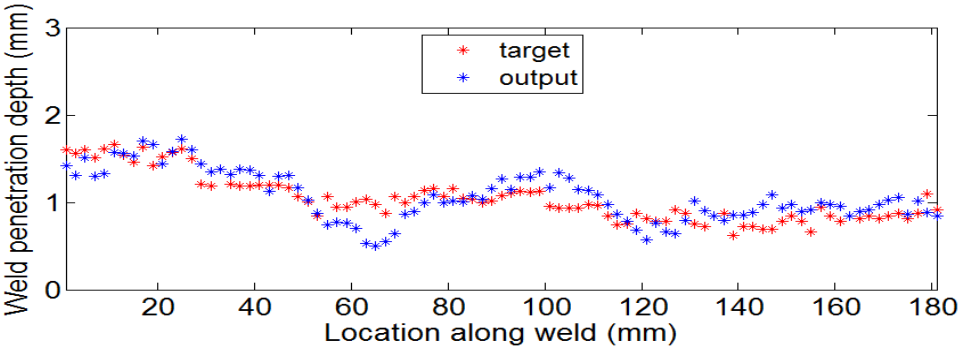

(b) Weld # 6

Fig. 6-22: Comparison of regression outputs and targets for welds # 5 and 6

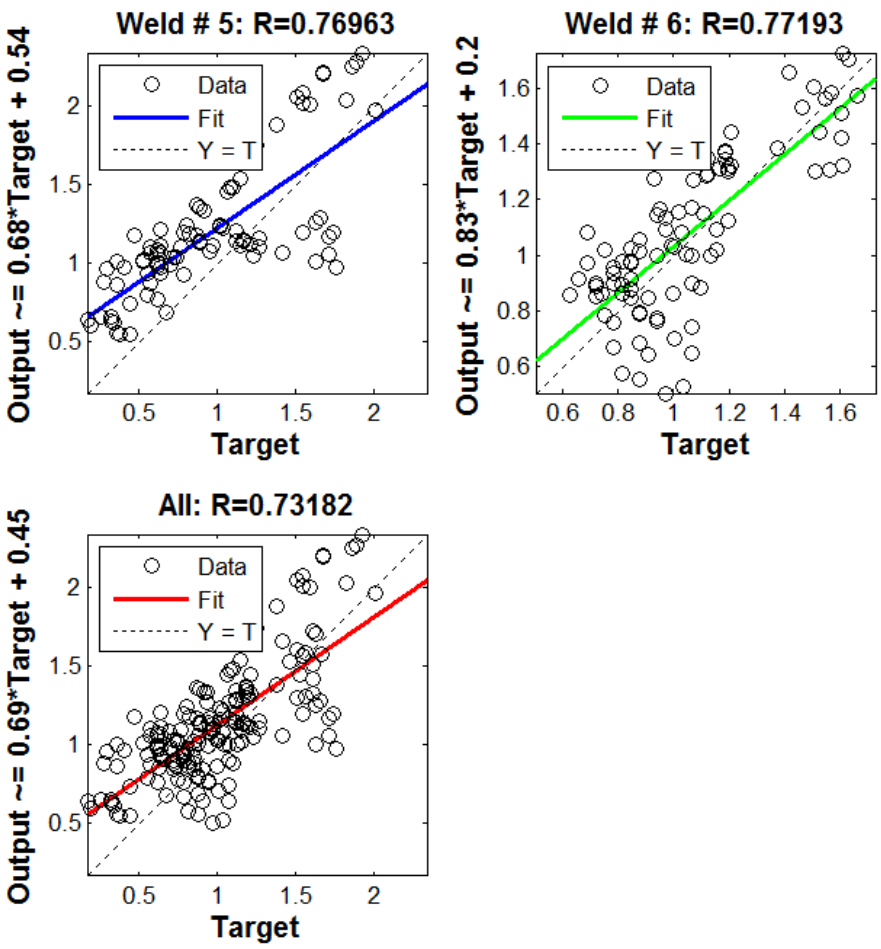

Fig. 6-23: Regression plots of regression outputs and targets for validation data

6.7 Localizations of Laser and EMAT in Inspection

The developed neural network proved the capability to predict WPDs in thin structures accurately. The laser and the EMAT need to be positioned properly in order to obtain high-quality signals. Fig. 6-24 shows four important distances during the inspection procedure. L1 is the distance from the laser source to the EMAT receiver. L2 is the distance from the laser source to the weld seam. L3 is the distance from the laser source to the laser-side edge, and L4 is the distance from the EMAT receiver to the EMAT-side edge. Considerations for determining these distances will be discussed next.

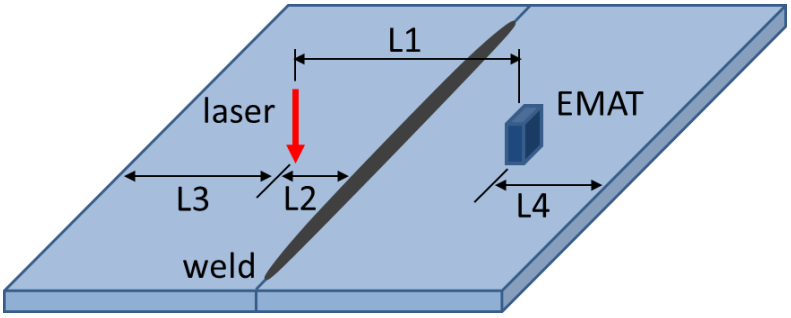

Fig. 6-24: Diagram showing important distances of LEU technique

6.7.1 Distance from Laser to EMAT

The distance from the laser source to the EMAT receiver cannot be either too large or small. If the laser-to-EMAT distance is too large, the SNR in received signals will be low due to attenuations of laser-generated Lamb waves. In Chapter 3, the LEU signal energy is estimated to attenuate at a rate of 0.4% per mm, and the LEU signal is estimated to die out after propagating for a maximum of 237 mm. Plus, a large laser-to-EMAT distance will make the received signals more vulnerable to reflections from sample edges, which will be explained in more details later. Fig. 6-25 shows CWTs of two signals acquired at different laser-to-EMAT distances. If the laser-to-EMAT distance is too small, different Lamb waves in received LEU signals are not separated enough in the time-frequency domain, which will affect the calculations of their transmission coefficients. Given the size of samples used in this work, the laser-to-EMAT distance is set to 64 mm, which proves to provide a good balance between the SNR and the capability to separate different Lamb waves.

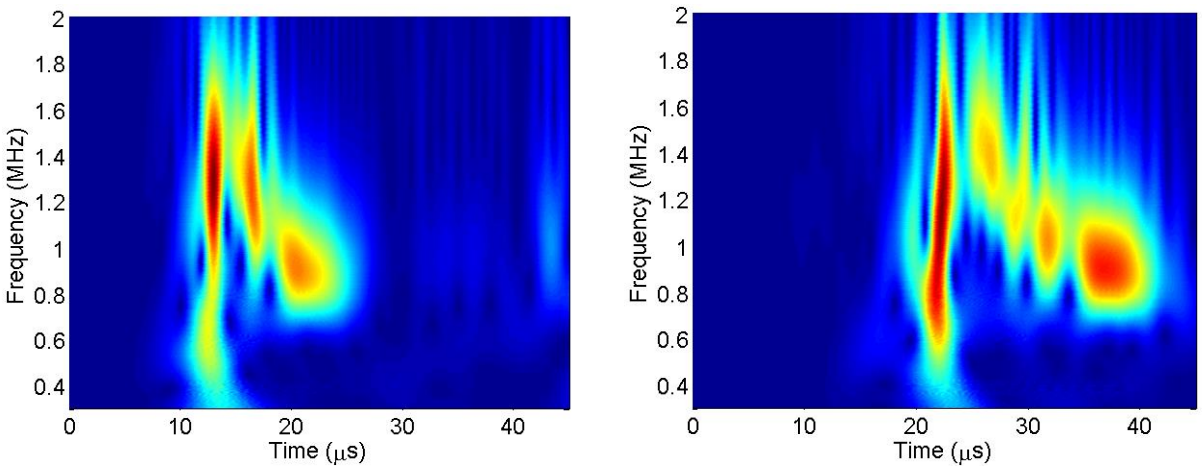

(a) Laser-to-EMAT distance = 35 mm (b) Laser-to-EMAT distance = 64 mm

Fig. 6-25: CWT plots of signals acquired at different laser-to-EMAT distances

6.7.2 Distance from Laser to Weld

When the welds were inspected non-destructively using the LEU technique, the laser-to-weld distance was changed from 7 mm to 47 mm at increments of 10 mm to evaluate its effect on the signal quality. Fig. 6-26 to Fig. 6-30 show the scatter plots of 23 selected Lamb waves when the laser-to-weld distance equals 7 mm, 17 mm, 27 mm, 37 mm, and 47 mm, respectively. Comparison shows that when the laser-to-weld distance equals 47 mm, the scatter plots of the selected Lamb waves have the clearest patterns. This means that LEU signals are more sensitive to varying WPDs when the EMAT is positioned close to weld seams. In this work, the ANN is trained with data acquired when the laser-to-weld distance was set to 47 mm. The EMAT-to-weld distance was 17 mm, accordingly.

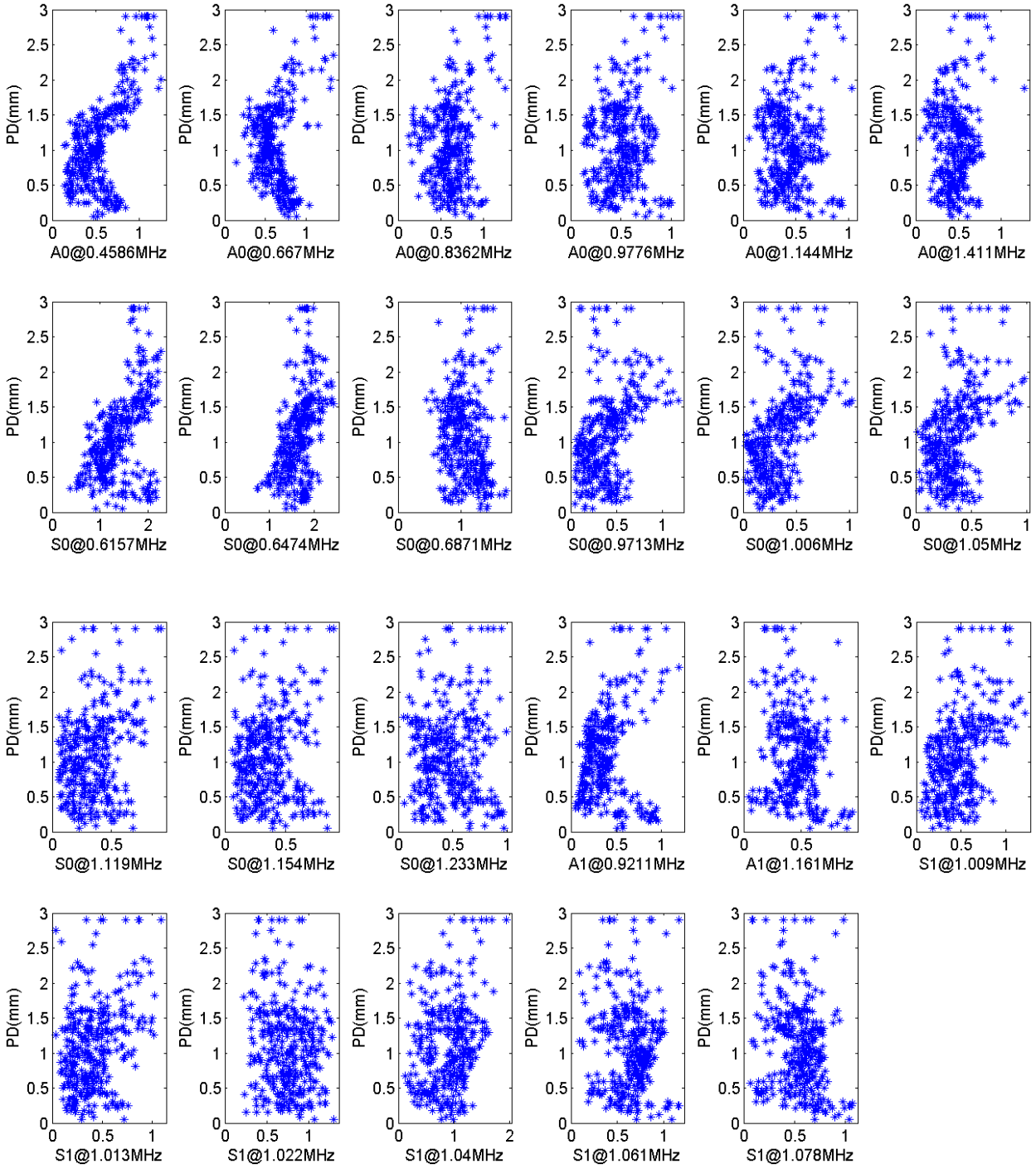

Fig. 6-26: Scatter plots when laser-to-weld distance is 7 mm

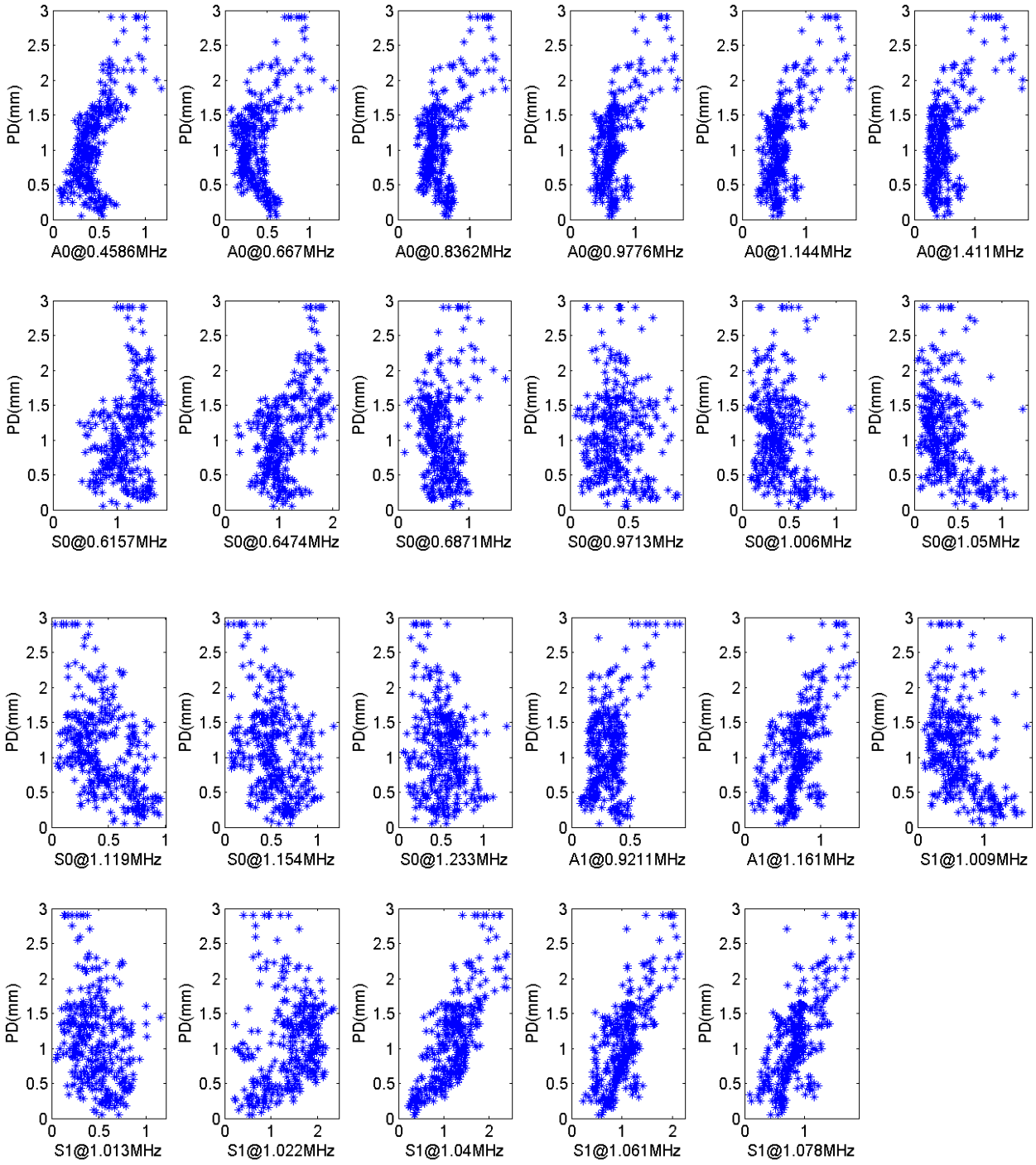

Fig. 6-27: Scatter plots when laser-to-weld distance is 17 mm

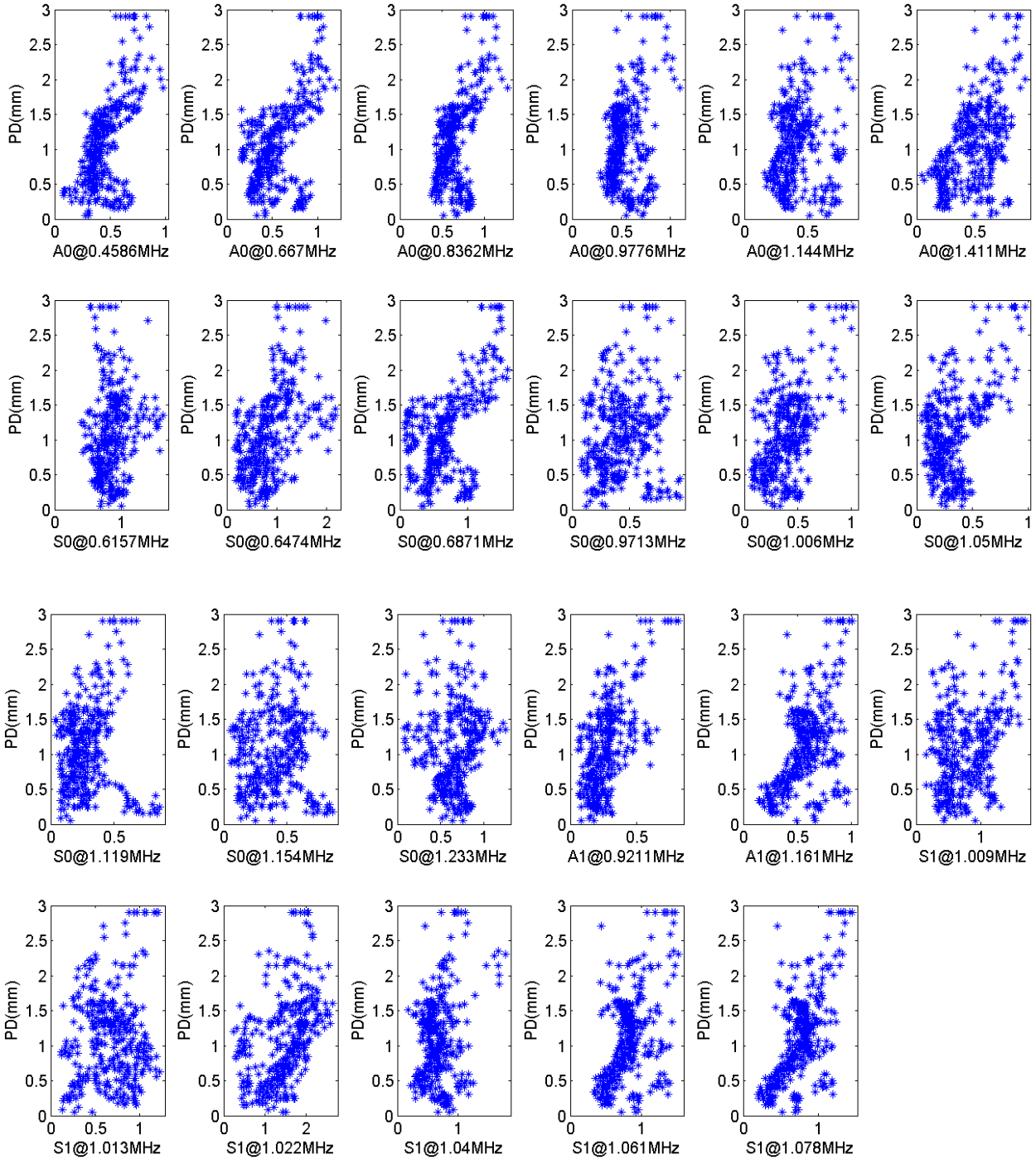

Fig. 6-28: Scatter plots when laser-to-weld distance is 27 mm

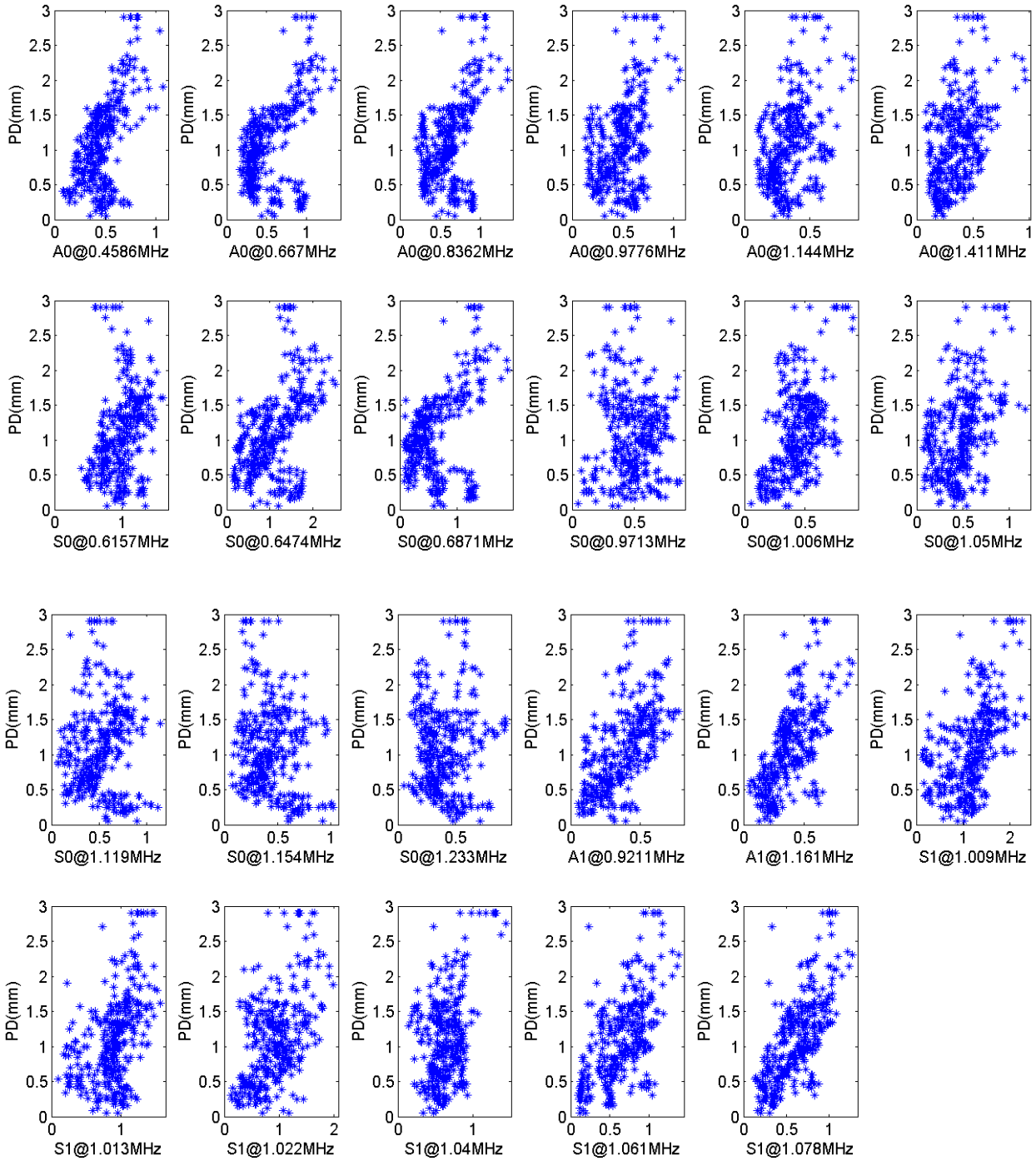

Fig. 6-29: Scatter plots when laser-to-weld distance is 37 mm

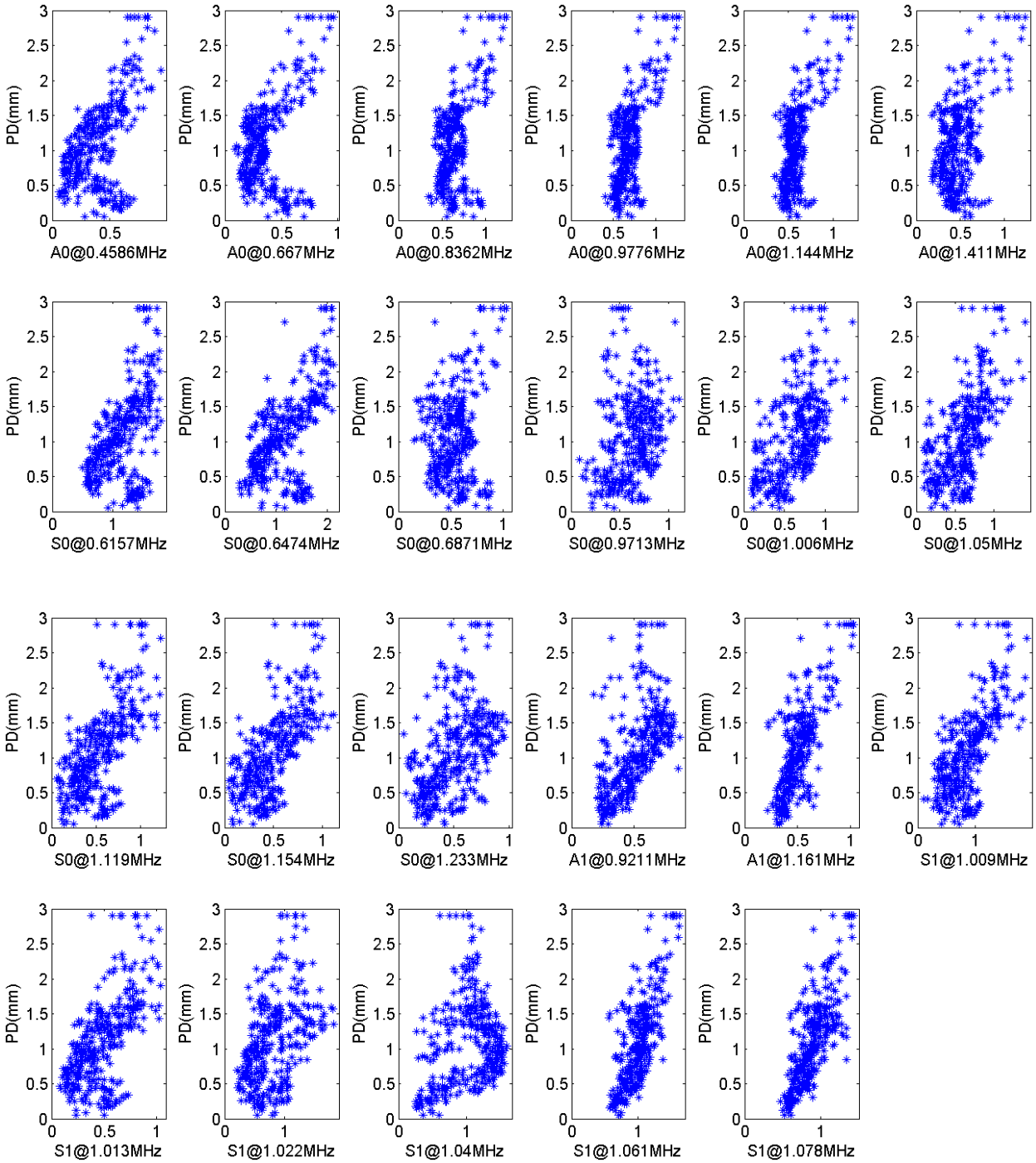

Fig. 6-30: Scatter plots when laser-to-weld distance is 47 mm

6.7.3 Distance from Laser to Laser-side Edge

The laser should be positioned far enough from the edge, otherwise the reflections from the laser-side edge can contaminate the received LEU signals, as shown in Fig. 6-31, and the calculated transmission coefficients will be affected. The fastest Lamb wave identified in the LEU signals travels at a speed of 3697 m/s. The slowest Lamb wave whose transmission coefficient is used to predict WPDs travels at a speed of 2004 m/s. The laser-to-edge distance should be large enough so that the reflection of the fasted Lamb wave cannot catch up with the slowest Lamb wave before the slowest Lamb wave reaches the EMAT receiver. The minimum value for the laser-to-edge distance can be calculated using Eq. 6-1, which is 27 mm when the laser-to-EMAT distance is 64 mm. Eq. 6-1 shows that increasing the laser-to-EMAT distance will increase the minimum acceptable value for the laser-to-edge distance.

$$D_{min} = \frac{C_{fastest} - C_{slowest}}{2C_{slowest}} D_{laser-EMAT} \qquad \textbf{(Eq. 6-1)}$$

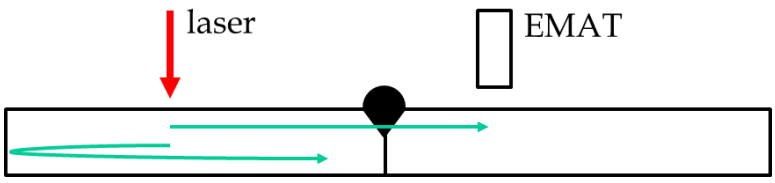

Fig. 6-31: Laser-side edge reflection

6.7.4 Distance from EMAT to EMAT-side Edge

For the same reason, the EMAT receiver should be positioned far enough from the EMAT-side edge, as shown in Fig. 6-32. The minimum value for the EMAT-to-edge distance can be calculated also using Eq. 6-1, which is 27 mm when the laser-to-EMAT distance is 64 mm. Increasing the

laser-to-EMAT distance will also increase the minimum acceptable value for the EMAT-to-edge distance.

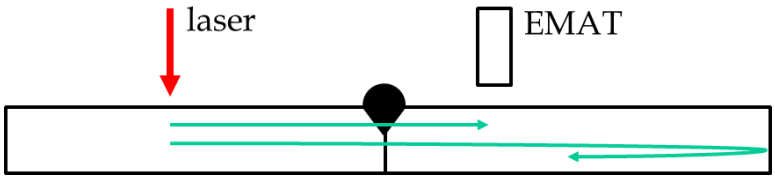

Fig. 6-32: EMAT-side edge reflection

6.8 Effect of Residual Stresses on Network Performance

Arc welding processes introduce residual stresses into welded samples due to uneven cooling speeds of molten metals. Typically heat treating is used to relieve the residual stresses after the welding process. This specific type of heat treating is called stress relief. For A36 steel, the recommended temperature is from 1100 ° - 1250 °F (593 °C – 676 °C), and the recommended soak time is one hour per inch of thickness [61]. Weld # 6 is stress relieved before cut-check and inspected again using the LEU technique to study the effect of the residual stresses on the network predictions. Weld # 6 is placed in an oven at 600 °C for half hour and then cools down slowly in the oven. Fig. 6-33 shows the predicted WPDs before and after the stress relief process. Fig. 6-34 shows the regression of predicted WPDs after stress relief and the cut-checked WPDs. The R value drops from 0.89264 to 0.78412, which indicates the presence of residual stresses will affect the calculated transmissions of selected Lamb waves and lower the prediction accuracy. It is recommended that a different network be trained to predict WPDs in thin structures which are stress relieved.

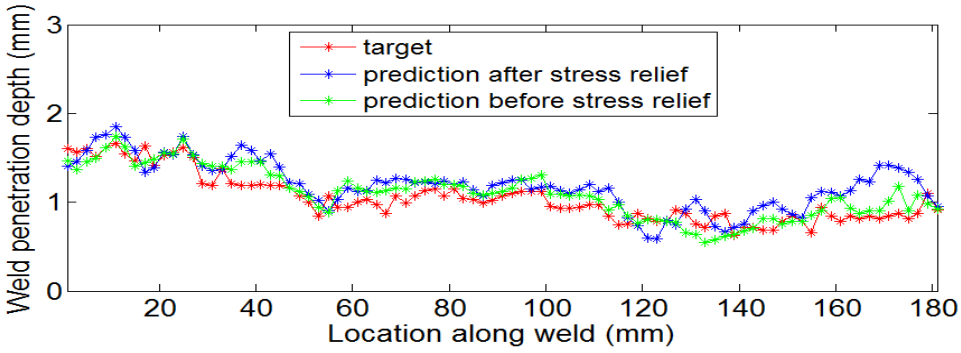

Fig. 6-33: Comparison of predictions before and after stress relief

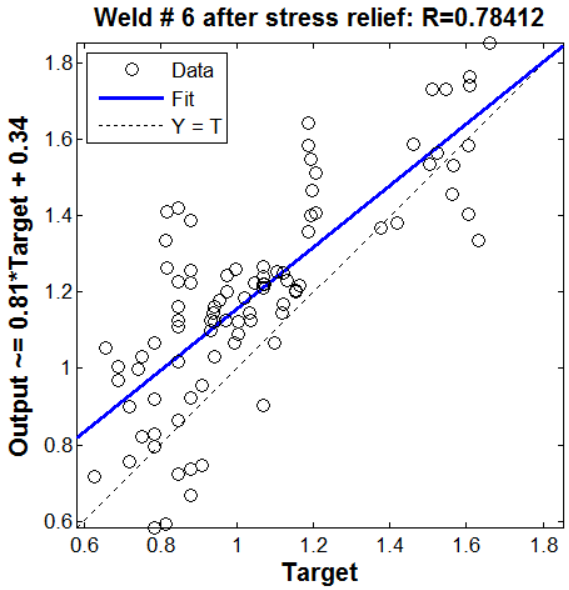

Fig. 6-34: Regression plot of predictions after stress relief and targets

6.9 Summary

Welds of different penetration depths are manufactured by varying welding parameters of GMAW. Transmission coefficients of selected Lamb waves are calculated based on CWT of individual LEU signals. A neural network is developed to accurately predict WPDs in thin structures based on transmission coefficients of selected Lamb waves and the LEU signal energy.

Proper positioning of the laser and the EMAT during the inspection process is discussed. The effect of residual stresses in welds on the prediction accuracy is also investigated.

CHAPTER 7

Conclusion, Contributions and Recommendations

7.1 Conclusion

The overall objective of this research is to extend the WPD measurement capability of the laser/EMAT ultrasonic technique to thin structures. This thesis conducted a systematic study to achieve this research objective. It started with characterization of the Lamb waves in the received LEU signals. A fundamental understanding of the LEU signals acquired in thin structures was established, which helped to narrow down the Lamb waves to be focused in the following studies. Next, the interactions of Lamb waves in LEU signals with a local lack of penetration defect was studied by measuring full wave field signals. Reflections and transmissions of some Lamb waves in LEU signals were found to be sensitive to the defect. This study proved the qualitative capability of the LEU technique to inspect WPD-related defects in thin structures. Later, transmission coefficients of some Lamb waves were proved to be able to measure notch depths in thin structures. A CWT-based method was shown effective to calculate transmission coefficients of different Lamb waves in LEU signals. Finally, welded samples were made to test the capability of using transmission coefficients of Lamb waves to predict WPDs in thin structures. Sensitive Lamb waves were selected, and a neural network was developed to use their transmission coefficients and the LEU signal energy to provide accurate predictions of WPDs. Some considerations regarding the implementation of the developed method were discussed.

The research objective was successfully accomplished. The deliverable of this research is an accurate, high-speed, non-contact, and non-destructive method to inspect WPDs in thin structures using the LEU technique. The most attractive feature of this method is that it requires only one signal to make the predictions, which makes it suitable for real-time WPD inspections. Proper positioning of the laser and the EMAT is discussed, which makes the method ready to use.

7.2 Contributions

Contributions of this research can be summarized as followings.

1. Experimentally characterized properties of Lamb waves present in received LEU signals and obtain a deep understanding of LEU signals acquired from thin structures.
2. Experimentally calculated the attenuation rate of LEU signals in thin plates.
3. Developed an efficient FEA model to study interactions of Lamb waves with surface notches
4. Developed a method to calculate transmission coefficients of Lamb waves in LEU signals based on CWT of individual signals, and proved its effectiveness by comparing with FEA results.
5. Established relationships of transmission coefficients of Lamb waves and WPDs, and selected Lamb waves which are sensitive to varying WPDs.
6. Developed an accurate neural network to predict WPDs in thin structures based on transmission coefficients of selected Lamb waves in LEU signals and the LEU signal energy.
7. Determined proper locations of the laser and the EMAT to guarantee signal qualities.

8. Investigated the effect of weld residual stresses on the network prediction performance.

7.3 Recommendations

The research objective is successfully accomplished. An accurate and efficient method is developed to predict WPDs in thin structures. However, there are still many areas in this research which can be further explored. Some recommendations for the future work are listed below.

1. More welded samples can be made to further test the network performance. The training data don't have many large WPD values.
2. Samples with different thicknesses can be made to adapt the developed neural network. If possible, it would be very attractive to make the network capable of predicting WPDs in structures of different thicknesses through continuous training.
3. The neural network is trained to measure WPDs in butt joint welds. There are other types of welds, such as lap joint weld, fillet weld, etc. Researches can be conducted to study if transmission coefficients of Lamb waves in LEU signals can predict WPDs in other types of welds.
4. Researches can be conducted to study if transmission coefficients of Lamb waves in LEU signals can predict other important weld dimensions or other weld defects.
5. Weld residual stresses are shown to lower the prediction accuracy. Researches can be done to compensate this error or develop a different neural network to predict WPDs of stress relieved welds.

6. The developed method is not ready for on-line WPD measurement because it doesn't consider the heat effect during the welding process. It would be helpful to study the heat effect and compensate the heat-related errors to make the method more attractive.
7. The LEU system used in this work can be improved from different aspects. The speed and automation level of the inspection procedure can be improved by upgrading the sample stage. The signal quality can be improved by using a better EMAT preamp.

References

[1] S. Kou and Y. Le, "Welding parameters and the grain structure of weld metal — A thermodynamic consideration," *Metallurgical Transactions A,* vol. 19, pp. 1075-1082, 1988/04/01 1988.

[2] R. Halmshaw, *Introduction to the Non-destructive Testing of Welded Joints*: Abington Publishing, 1996.

[3] A. C. o. M. o. Inspection and A. W. Society, *The Everyday Pocket Handbook for Visual Inspection and Weld Discontinuities -- Causes and Remedies*: American Welding Society, 2004.

[4] T. W. Liao and J. Ni, "An automated radiographic NDT system for weld inspection: Part I — Weld extraction," *NDT & E International,* vol. 29, pp. 157-162, 1996.

[5] T. W. Liao and Y. Li, "An automated radiographic NDT system for weld inspection: Part II— Flaw detection," *NDT & E International,* vol. 31, pp. 183-192, 6// 1998.

[6] K. Aoki and Y. Suga, "Application of Artificial Neural Network to Discrimination of Defect Type in Automatic Radiographic Testing of Welds," *ISIJ International,* vol. 39, pp. 1081-1087, 1999.

[7] J. Y. Lee, S. J. Lee, D. C. Jiles, M. Garton, R. Lopez, and L. Brasche, "Sensitivity analysis of simulations for magnetic particle inspection using the finite-element method," *Magnetics, IEEE Transactions on,* vol. 39, pp. 3604-3606, 2003.

[8] C. E. Betz, *Principles of Magnetic Particle Testing*. Chicago, IL: Magnaflux Corp., 1985.

[9] http://en.wikipedia.org/wiki/Dye_penetrant_inspection.

[10] P. E. E. E. Paul E. Mix, *Introduction to Nondestructive Testing: A Training Guide*: Wiley, 2005.

[11] D. J. Hagemaier, *Fundamentals of Eddy Current Testing*: American Society for Nondestructive Testing, 1990.

[12] A. Runnemalm, J. Ahlberg, A. Appelgren, and S. Sjökvist, "Automatic Inspection of Spot Welds by Thermography," *Journal of Nondestructive Evaluation,* vol. 33, pp. 398-406, 2014/09/01 2014.

[13] H. C. Wikle Iii, S. Kottilingam, R. H. Zee, and B. A. Chin, "Infrared sensing techniques for penetration depth control of the submerged arc welding process," *Journal of Materials Processing Technology,* vol. 113, pp. 228-233, 2001.

[14] M. Vasudevan, N. Chandrasekhar, V. Maduraimuthu, A. K. Bhaduri, and B. Raj, "Real-time monitoring of weld pool during GTAW using infra-red thermography and analysis of infra-red thermal images," *Welding in the World,* vol. 55, pp. 83-89, 2011.

[15] X. P. Gu, J. Liu, G. C. Xu, and X. Y. Gu, "Ultrasonic Testing and Evaluation of Laser Welds in Stainless Steel," *Lasers in Engineering (Old City Publishing),* vol. 26, pp. 103-113, 2013.

[16] S. Dixon, C. Edwards, and S. B. Palmer, "A laser–EMAT system for ultrasonic weld inspection," *Ultrasonics,* vol. 37, pp. 273-281, 1999.

[17] S. Dixon, S. E. Burrows, B. Dutton, and Y. Fan, "Detection of cracks in metal sheets using pulsed laser generated ultrasound and EMAT detection," *Ultrasonics,* vol. 51, pp. 7-16, 1// 2011.

[18] S. J. Davies, C. Edwards, G. S. Taylor, and S. B. Palmer, "Laser-generated ultrasound: its properties, mechanisms and multifarious applications," *Journal of Physics D: Applied Physics,* vol. 26, p. 329, 1993.

[19] B. Mi and I. C. Ume, "Parametric Studies of Laser Generated Ultrasonic Signals in Ablative Regime: Time and Frequency Domains," *Journal of Nondestructive Evaluation,* vol. 21, pp. 23-33, 2002/03/01 2002.

[20] C. B. Scruby and L. E. Drain, *Laser Ultrasonics: Techniques and Applications*: A. Hilger, 1990.

[21] M. D. Rogge, *In-process Sensing of Weld Penetration Depth Using Non-contact Laser Ultrasound System*. PhD Thesis, Georgia Institute of Technology.: ProQuest Information and Learning Company, 2009.

[22] B. Mi and C. Ume, "Real-Time Weld Penetration Depth Monitoring With Laser Ultrasonic Sensing System," *Journal of Manufacturing Science and Engineering,* vol. 128, pp. 280-286, 2006.

[23] K. A, "Measurement of Weld Penetration Depth Using Non-contact Ultrasound Methods," *PhD Thesis, Georgia Institute of Technology,* 2005.

[24] A. Kita and C. Ume, "Measuring on-line and off-line noncontact ultrasound time of flight weld penetration depth," *American Welding Society,* vol. 86, 2007.

[25] M. Bao, "Implementation of Fiber Phased Array Ultrasound Generation System and Signal Analysis for Weld Penetration Control," PhD Dissertation, Georgia Institute of Technology, 2003.

[26] J. Sadler and R. G. Maev, "Experimental and theoretical basis of Lamb waves and their applications in material sciences," *Canadian Journal of Physics,* vol. 85, pp. 707-731, 2007.

[27] S. Yashiro, J. Takatsubo, and N. Toyama, "An NDT technique for composite structures using visualized Lamb-wave propagation," *Composites Science and Technology,* vol. 67, pp. 3202-3208, 12// 2007.

[28] Y. Zheng, C. F. He, J. J. Zhou, and Y. C. Zhang, "2D scattering characteristics of Lamb wave at defects," *Gongcheng Lixue/Engineering Mechanics,* vol. 30, pp. 236-243, 2013.

[29] J. D. Achenbach, *Wave propagation in elastic solids*. Amsterdam, New York: North-Holland Pub. Co.; American Elsevier Pub. Co, 1973.

[30] T.-Y. Wu and I. C. Ume, "Fundamental study of laser generation of narrowband Lamb waves using superimposed line sources technique," *NDT & E International,* vol. 44, pp. 315-323, 5// 2011.

[31] T.-Y. Wu and I. C. Ume, "Measurement of Weld Dimensions of Butt Joint Welding in Thin Plates Using Superimposed Laser Sources," in *ASME 2010 International Mechanical Engineering Congress and Exposition*, 2010, pp. 549-561.

[32] D. A. Hutchins, R. J. Dewhurst, and S. B. Palmer, "Directivity patterns of laser‐generated ultrasound in aluminum," *The Journal of the Acoustical Society of America,* vol. 70, pp. 1362-1369, 1981.

[33] L. R. F. Rose, "Point‐source representation for laser‐generated ultrasound," *The Journal of the Acoustical Society of America,* vol. 75, pp. 723-732, 1984.

[34] Z. Guo, J. D. Achenbach, and S. Krishnaswamy, "EMAT generation and laser detection of single lamb wave modes," *Ultrasonics,* vol. 35, pp. 423-429, 9// 1997.

[35] M. Farge, "Wavelet Transforms and their Applications to Turbulence," *Annual Review of Fluid Mechanics,* vol. 24, pp. 395-458, 1992.

[36] C. Torrence and G. P. Compo, "A Practical Guide to Wavelet Analysis," *Bulletin of the American Meteorological Society,* vol. 79, pp. 61-78, 1998.

[37] T. E. Michaels, J. E. Michaels, and M. Ruzzene, "Frequency-wavenumber domain analysis of guided wavefields," *Ultrasonics,* vol. 51, pp. 452-66, May 2011.

[38] D. Alleyne and P. Cawley, "A two-dimensional Fourier transform method for the measurement of propagating multimode signals," *The Journal of the Acoustical Society of America,* vol. 89, pp. 1159-1168, 1991.

[39] M. Ruzzene, "Frequency-wavenumber domain filtering for improved damage visualization," *Smart Materials and Structures,* vol. 16, pp. 2116-2129, 2007.

[40] M. D. Rogge and C. A. C. Leckey, "Characterization of impact damage in composite laminates using guided wavefield imaging and local wavenumber domain analysis," *Ultrasonics,* vol. 53, pp. 1217-1226, 2013.

[41] T. E. Michaels and J. E. Michaels, "Application of acoustic wavefield imaging to non-contact ultrasonic inspection of bonded components," in *AIP Conference Proceedings*, 2006, p. 1484.

[42] D. N. Alleyne and P. Cawley, "A 2-dimensional Fourier transform method for the quantitative measurement of Lamb modes," in *Ultrasonics Symposium, 1990. Proceedings., IEEE 1990*, 1990, pp. 1143-1146 vol.2.

[43] A. H. Meitzler, "Backward‐Wave Transmission of Stress Pulses in Elastic Cylinders and Plates," *The Journal of the Acoustical Society of America,* vol. 38, pp. 835-842, 1965.

[44] D. Cerniglia and B. Djordjevic, "Analysis of laser-generated lamb waves with wavelet transform," *NONDESTRUCTIVE CHARACTERIZATION OF MATERIALS,* pp. 63-68, 2003.

[45] S. W. Kercel, M. B. Klein, and B. F. Pouet, "Wavelet and wavelet-packet analysis of Lamb wave signatures in laser ultrasonics," 2000, pp. 308-317.

[46] A. Yun-Kyu, P. Byeongjin, and S. Hoon, "Complete noncontact laser ultrasonic imaging for automated crack visualization in a plate," *Smart Materials and Structures,* vol. 22, p. 025022, 2013.

[47] H. Sohn, D. Dutta, J. Yang, M. Desimio, S. Olson, and E. Swenson, "A wavefield imaging technique for delamination detection in composite structures," DTIC Document2010.

[48] A. Yun-Kyu, S. Homin, and S. Hoon, "Wireless ultrasonic wavefield imaging via laser for hidden damage detection inside a steel box girder bridge," *Smart Materials and Structures,* vol. 23, p. 095019, 2014.

[49] L. Jung-Ryul, T. Junji, T. Nobuyuki, and K. Dong-Hoon, "Health monitoring of complex curved structures using an ultrasonic wavefield propagation imaging system," *Measurement Science and Technology,* vol. 18, p. 3816, 2007.

[50] J.-R. Lee, C. Ciang Chia, H. Jin Shin, C.-Y. Park, and D. Jin Yoon, "Laser ultrasonic propagation imaging method in the frequency domain based on wavelet transformation," *Optics and Lasers in Engineering,* vol. 49, pp. 167-175, 2011.

[51] E. B. Flynn, S. Y. Chong, G. J. Jarmer, and J.-R. Lee, "Structural imaging through local wavenumber estimation of guided waves," *NDT & E International,* vol. 59, pp. 1-10, 10// 2013.

[52] Z. M. Master, T. E. Michaels, and J. E. Michaels, "Incident wave removal for defect enhancement in acoustic wavefield imaging," in *AIP conference Proceedings*, 2007, p. 665.

[53] J. Jin, S. Tong Quek, and Q. Wang, "Wave boundary element to study Lamb wave propagation in plates," *Journal of Sound and Vibration,* vol. 288, pp. 195-213, 11/22/ 2005.

[54] D. N. Alleyne and P. Cawley, "The interaction of Lamb waves with defects," *Ultrasonics, Ferroelectrics, and Frequency Control, IEEE Transactions on,* vol. 39, pp. 381-397, 1992.

[55] M. J. S. Lowe, P. Cawley, J.-Y. Kao, and O. Diligent, "Prediction and measurement of the reflection of the fundamental anti-symmetric Lamb wave from cracks and notches," *AIP Conference Proceedings,* vol. 509, pp. 193-200, 2000.

[56] M. J. S. Lowe, P. Cawley, J.-Y. Kao, and O. Diligent, "The low frequency reflection characteristics of the fundamental antisymmetric Lamb wave a0 from a rectangular notch in a plate," *The Journal of the Acoustical Society of America,* vol. 112, pp. 2612-2622, 2002.

[57] M. J. S. Lowe and O. Diligent, "Low-frequency reflection characteristics of the s0 Lamb wave from a rectangular notch in a plate," *The Journal of the Acoustical Society of America,* vol. 111, pp. 64-74, 2002.

[58] P. K. Simpson, *Artificial neural systems: foundations, paradigms, applications, and implementations*: Windcrest/McGraw-Hill, 1990.

[59] B. C. Csáji, "Approximation with artificial neural networks," *Faculty of Sciences, Etvs Lornd University, Hungary,* vol. 24, 2001.

[60] P. Gagné and C. M. Dayton, "Best regression model using information criteria," *Journal of Modern Applied Statistical Methods,* vol. 1, p. 57, 2002.

[61] S. Funderburk, "Key concepts in welding engineering," *Welding Innovation,* vol. 16, 1999.